UNIVERSITY OF POTSDAM
DEPARTMENT OF PHYSICS AND ASTRONOMY

MAX-PLANCK INSTITUTE FOR ASTRONOMY HEIDELBERG

MASTER THESIS

Determining the physical parameters of eclipsing binaries from the B-Type Binaries Characterization programme (BBC) with PHOEBE

Henry Willems
Matricle number: 801610

supervised by
Prof. Hans-Walter Rix
Jaime Villaseñor

February 21, 2025

Contents

1 Introduction **4**
1.1 Binary stars . . . 4
1.1.1 Importance of studying binaries . . . 4
1.1.2 Physical parameters . . . 5
1.1.3 Orbital parameters . . . 6
1.1.4 Orbital configurations . . . 9
1.2 Massive binaries . . . 12
1.3 B-type binaries . . . 14
1.4 Large Magellanic Cloud and 30 Doradus . . . 15
1.5 Spectroscopic observations of B-type binaries in the LMC . . . 16
1.5.1 VLT-FLAMES Tarantula survey . . . 16
1.5.2 B-type characterization programme . . . 17
1.5.3 Other spectroscopic studies of massive eclipsing binaries . . . 18
1.6 Photometric observations . . . 18
1.6.1 Limitations of spectroscopic-only observations and need for photometric data . . . 18
1.6.2 Optical Gravitational Lensing Experiement . . . 19
1.6.3 Other photometric studies . . . 20
1.7 Eclipsing binaries . . . 20
1.8 Open issues in stellar evolution of massive B-type binaries . . . 21
1.9 Scientific aim of the work . . . 23

2 Methodology **24**
2.1 Period determination . . . 24
2.1.1 Lomb-Scargle . . . 24
2.1.2 Box-Least-Squares . . . 25
2.1.3 Special cases with inconsistent periods . . . 27
2.2 Classification of light curves . . . 32
2.3 Initial models and optimization . . . 32
2.3.1 Setting initial model parameters . . . 34
2.3.2 Model optimization . . . 36
2.4 Estimations of parameter uncertainties (EMCEE) . . . 37

3 Results **39**
3.1 Stellar parameters of the system's components . . . 39
3.2 Plotting on HRD with isochrones . . . 46
3.3 Systems having both components on the same isochrone . . . 48
3.4 Systems with no common isochrone (mass-transferring candidates) . . . 50
3.5 Systems where the relationship to the isochrones is uncertain . . . 51
3.6 Comparison with evolutionary tracks . . . 51

4 Discussion **51**
4.1 Comparison of parameters 54
4.1.1 Mass ratios 54
4.1.2 Effective temperatures, radii and spectroscopic type 55
4.2 Interesting finding 57
4.2.1 Mass transfer candidates 57
4.2.2 Findings based on the parameters 58

5 Conclusions **60**

6 Summary **62**

7 Kurzzusammenfassung (Deutsch) **62**

A Model solutions **69**

B EMCEE corner plots **72**

Abstract

Context. Massive stars are mostly found in binary systems. Their evolution can be altered if the components interact with each other by transferring mass. Therefore, it is important to assess how many of these systems show evidence of ongoing or past mass transfers. The B-Type Binaries characterisation (BBC) programme is a spectroscopic survey carried out on 88 massive binaries in the 30 Doradus region, located in the Large Magellanic Cloud (LMC). 82 out of these stars were also photometrically observed by OGLE and some of them are already known eclipsing binary systems.

Aims. With the combination of processed spectroscopic data of 88 massive B-type binaries from the BBC and photometric data from OGLE, this work aims to get tight constraints for the parameters that determine the binary system. Photometric data of eclipsing binaries can yield the effective temperatures T_{eff}, the equivalent radii r_{eq} and the orbital inclination i with high precision, allowing us to find out in which physical configuration and in which evolutionary state the components are and to find out whether systems have undergone or are undergoing a phase of mass transfer.

Methods. The data of the massive binary systems have spectroscopically been processed by the BBC. To get the stellar and orbital parameters at a high precision, this work complements the existing orbital solutions from the spectroscopy with photometric data coming from OGLE. With the use of the Lomb-Scargle and the Box-Least-Squares analysis, the period of a system is first determined. After the period is given, the data is phase-folded to produce the light curve that contains the eclipses. This light curve is then passed into `PHOEBE`, a modelling software, where one can set initial model parameters, approaching the shape of the observed data. When reaching a sufficiently close agreement, the model is then optimized via `Nelder-Mead` to determine the precise values for the important parameters. Finally, `EMCEE` returns their uncertainties to see how reliable the returned values are. These values are then used to put the components on a Hertzsprung-Russell diagram with isochrones to determine whether both components are located on a common isochrone. Mass transferring candidates are identified as those that do not fit on a common isochrone.

Results. Out of the sample of 82 objects having both OGLE and BBC data, 9 showed clear eclipsing signatures in the light curves. Their periods were mostly in the range of 1.4 to 4.4 days, including close binary systems, possibly being a contact system and/or undergoing a phase of mass transfer. Furthermore, 4 stars showed ellipsoidal variations and even a heartbeat star was discovered. Of these 14 studied systems, three showed evidence of ongoing or past mass transfers and three more systems have a high likelihood of being a (post-)mass-transfer system.

Conclusions. It turned out that close massive binary systems can undergo a phase of mass transfer at a significant probability, however, most systems fit on one common isochrone, meaning that they are not mass-transfer candidates. It also becomes clear that looking for mass-transferring systems is a challenging task, requiring a good set of both photometric and spectroscopic data.

1 Introduction

1.1 Binary stars

The observable universe contains an immense number of stars, a substantial proportion of which exist within a binary or multiple-star system, where the components orbit each other.

1.1.1 Importance of studying binaries

Due to the large number of binaries, they are a crucial part of the understanding of star formation and evolution. Within a distance of 1 kpc from the sun, more than 1 million binaries were resolved using the Gaia eDR3 catalogue (El-Badry, Rix, and Heintz 2021).
The multiplicity fraction of stars depending on the mass was studied by Offner et al. (2023) and Figure 1 illustrates it. The multiplicity fraction is the ratio of stars being a

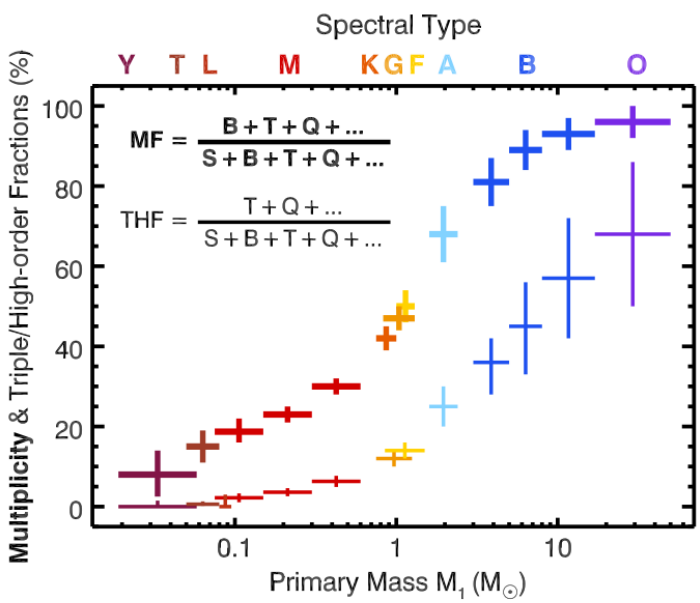

Figure 1: Binary multiplicity fraction (upper crosses), fraction of at least triples (lower crosses). This figure illustrates that most of the most massive stars are in binaries. Taken from Offner et al. 2023.

member of a system of at least two stars compared to the total number of stars.
It was observed that almost all massive stars are part of a binary system. As a result, examining the physical parameters of the components of binary and multiple systems is essential in advancing our understanding of stellar evolution in these systems. During the stellar evolution, many systems will experience interactions between the members of the system. Such studies also contribute to a broader per-

spective of star formation processes and history, especially in active star-forming regions.
Despite declining towards lower masses, the multiplicity fraction of solar-type stars is still fairly high at about 50 % (Offner et al. 2023). This trend continues towards lower mass stars and the coolest stars (M-type dwarfs) have a binary fraction of about 20-30 %.

1.1.2 Physical parameters

In binary systems, a hierarchy among the members has to be defined to know which star is called the primary and secondary. Mostly the disambiguation is done by the mass, such that the primary is the star with the higher mass. For stars in a binary, physical parameters can be defined. They describe how massive, how large and hot a star is. From these parameters, the total integrated energy output per unit time of a star, which is called the luminosity, can be derived. It can be calculated with the effective temperature T_{eff} and the equivalent radius R_{eq} with the Stefan-Boltzmann law (eq. 1)

$$L = 4\pi R_{\mathrm{eq}}^2 \sigma T_{\mathrm{eff}}^4 \tag{1}$$

The emission spectrum of a star can be approximated by a black body. A black body is an object that emits a continuum spectrum in the wavelength regime, assuming all incoming radiation is absorbed and all radiation gets re-emitted. The effective temperature is the temperature of a black body that shows the same total flux emission as the star does. Figure 2 shows the spectral irradiance as a function of wavelength, plotted for different effective temperatures ranging from 4000 (red) to 28000 K (blue) with a spacing of 2000 K. This can be calculated using eq. (2).

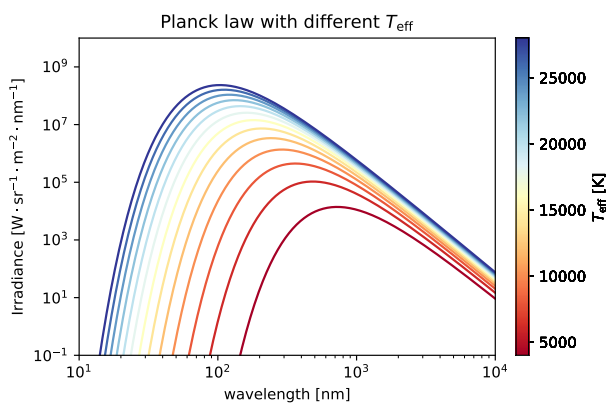

Figure 2: Planck law in wavelength for different effective temperatures it provides fluxes per wavelength bins and sky area and the maximum for hot stars lies in the blue or UV regime

$$B_\lambda(\lambda, T) = \frac{hc^2}{\lambda^5} \cdot \frac{1}{e^{\frac{hc}{k_B \lambda T}} - 1} \tag{2}$$

where B_λ is the spectral irradiance at a wavelength λ, h the Planck constant, c the speed of light, T the effective temperature and k_B is the Boltzmann constant.
As it can be seen in Fig. 2, the maximum flux shifts to shorter wavelengths when the black body increases its temperature and the flux itself at this point also increases. This principle is known as Wien's displacement law (eq. 3)

$$\lambda_{\max} = \frac{2.898 \cdot 10^{-3} \mathrm{m} \cdot \mathrm{K}}{T_{\mathrm{eff}}}. \tag{3}$$

Wien's displacement law states an inverse proportionality between the effective temperature T_{eff} and the wavelength of maximum irradiance $\lambda_{\max}$ (equation 3).
While luminosity is a feature that can be assigned to both stars individually, the same applies to the star's mass. An important parameter describing the relationship of both components is the **mass ratio** (q). It describes the ratio of the mass that both components have. It is usually defined as

$$q := \frac{M_{\mathrm{secondary}}}{M_{\mathrm{primary}}}. \tag{4}$$

A mass ratio of 1 means that both components have the same mass while a value much smaller than 1 represents a binary where most of the mass of the binary is concentrated in the primary star.
While physical parameters describe the nature of the stars themselves, other parameters describe the orbital dynamics of the system.

1.1.3 Orbital parameters

Orbital parameters can be defined in binary systems and they are linking both of the components. A visualization of the parameters that are discussed in this section can be seen in Fig. 3. The Keplerian laws describe the orbital dynamics of objects orbiting each other. The first law describes that one object orbits around the more massive orbital parent in an ellipse and the more massive object sits at one of the foci. Fig. 4 visualises an ellipse with the foci. The blue line is the actual ellipse, the green and the red lines represent the semi-major (a) and semi-minor axis (b) respectively and the yellow dots are the focal points of the ellipse located at $(\pm\sqrt{a^2 - b^2}, 0)$. In Fig. 4, the semi-major axis was set to 1 unit and the semi-minor axis to 0.5 units.
The second law describes that the connecting vector between the orbiting object and its parent passes through an equal area at a constant time interval. This law implies the conservation of angular momentum, resulting in a faster motion when closer to the orbital parent and a slower motion when further apart.
The third law states that the square of the orbital period is proportional to the cube of the semi-major axis ($P^2 \propto a^3$). It can be derived by equating Newton's gravitational law with the centripetal force, eventually yielding

$$\frac{a^3}{P^2} = \frac{G(M_1 + M_2)}{4\pi^2} \tag{5}$$

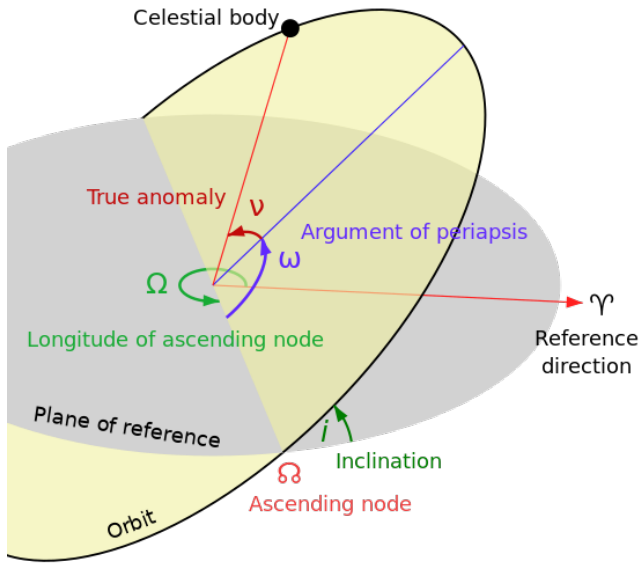

Figure 3: Orbital parameters visualized. Made by Lasunncty at the English Wikipedia, CC BY-SA 3.0 http://creativecommons.org/licenses/by-sa/3.0/, via Wikimedia Commons

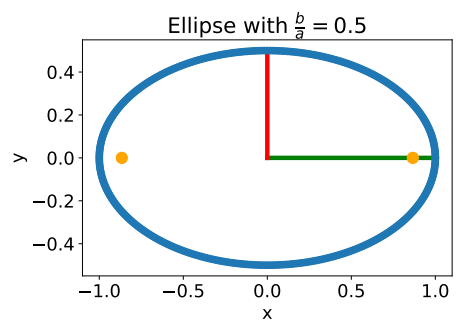

Figure 4: Visualization of an ellipse

with M_1 and M_2 being the masses of the stars, a the semi-major axis and G is the gravitational constant. Since in a binary star, both components orbit each other, one can define the orbital **period** P. A period has passed when both stars have reached the same point in their orbits again. Figure 5 shows a radial velocity (RV) curve of

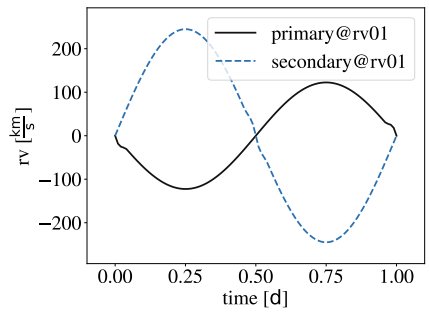

Figure 5: Radial velocity curve to illustrate an orbital period, created with `PHOEBE`

a binary system with a mass ratio of $q = 0.5$. The RV is defined as the component of the velocity vector that points radially, either towards the observer or away from it. An orbital period in this case passed as soon as both stars reached the same RVs *and* change of RVs again. It is really important to consider the latter to fully get the orbital period correctly.

With Kepler's third law (equation 5), the orbital period can be connected to the **semi-major axis** a. The semi-major axis is a line passing through both foci and the periastron (see Fig, 4) of the ellipse and it describes the distance between the objects orbiting each other. For example, the Earth has a semi-major axis of 1 AU ($\approx 1.5 \cdot 10^{11}$m). The semi-major axis has a relationship to the periastron r_{min} and apoastron r_{max}, given in equation 6. The periastron and the apoastron are the closest and furthest distances from the stars respectively.

$$a = \frac{r_{\text{min}} + r_{\text{max}}}{2}. \tag{6}$$

The values of r_{min} and r_{max} are also related with the semi-major axis through the geometry of the ellipse, which is called the orbital **eccentricity** e.

It describes the orbit's geometry from $e = 0$ (circular) to values just below 1 (highly eccentric orbits). Then the periastron and apoastron are found at the following distances:

$$r_{\text{min}} = a(1 - e) \tag{7}$$

$$r_{\text{max}} = a(1 + e) \tag{8}$$

The eccentricity e is defined with the ratio of the two axes of the ellipses, the semi-major axis a and the semi-minor axis b as follows:

$$e = \sqrt{1 - \frac{b^2}{a^2}} \tag{9}$$

The eccentricity and the semi-major axis describe the shape and the size of the ellipse. Then two more parameters set the orientation of the ellipse in a plane.
The **inclination** is an angle that states the difference of the orbital plane relative to a reference frame. In the solar system, the reference frame is defined by Earth's orbit and it is shown as the apparent path of the sun in the sky during the year (known as the ecliptic). For binaries outside the solar system, the reference frame is defined in such a way that an edge-on view has an inclination of 90 degrees (see Fig. 14a).
The **longitude of ascending node** (☊) sets the position angle where the orbit passes through the reference frame from south to north (upwards when considering a counterclockwise orbit).
Two more parameters are used to describe the orientation of the semi-major axis and the current location of the object within the orbit. The **argument of periastron** ω states the orientation of the axis connecting the periastron (the closest point between both stars) with the apoastron (farthest point of both stars). Note that ω is called the argument of peri*apsis* in Fig. 3 (apsis relates to the centre of gravity, barycenter). However, in this work, this is called the argument of peri*astron* because here two stars (Greek *astron* star) orbit each other. The angle is counted from the ascending node where the orbit passes through a reference plane.
Related to the argument of periastron is the **true anomaly**, saying where in the orbit the celestial body is located at a specific time. Denoted as ν in Fig. 3, it is the difference of the angle starting from the ascending node ☊to the object's current location φ_{current} and the argument of periastron

$$\nu = \varphi_{\text{current}} - \omega \tag{10}$$

1.1.4 Orbital configurations

Binary stars can be in three different configurations that are based on the Roche lobe filling factor. The **Roche geometry** describes the gravitational potential of the stars and mass transfer occurs if any of those stars fills or overflows its Roche lobe (see glossary in Heber (2024)). This mass transfer happens because material outside the Roche lobe of a star gets more attracted by the companion at the first Lagrangian point (L_1), located at the intersection of both Roche lobes.
Mass transfer can be either stable or unstable. A stable mass transfer is given if the rate $\dot{M}$ does not make sudden jumps over a long period. Unstable mass transfer occurs if a star expands faster than the Roche lobe or the star shrinks slower than the Roche lobe. It is known for a changing rate of $\dot{M}$ over time. The panels in Figure 6 show the two components as dark spheres and the boundary of the Roche lobes, which is dependent on the mass ratio q, is shown with the thin black line. A formula giving an approximate radius (better than 1% accuracy) of the Roche lobe R_L was given by Eggleton (1983):

$$R_L = \frac{0.49q^{2/3}}{0.6q^{2/3} + \ln(1 + q^{1/3})}, \text{for } 0 < q < \infty \tag{11}$$

The stars can be in three different configurations. They can be either detached (Fig. 7), semi-detached (Fig. 8) or in a contact system (Fig. 9).

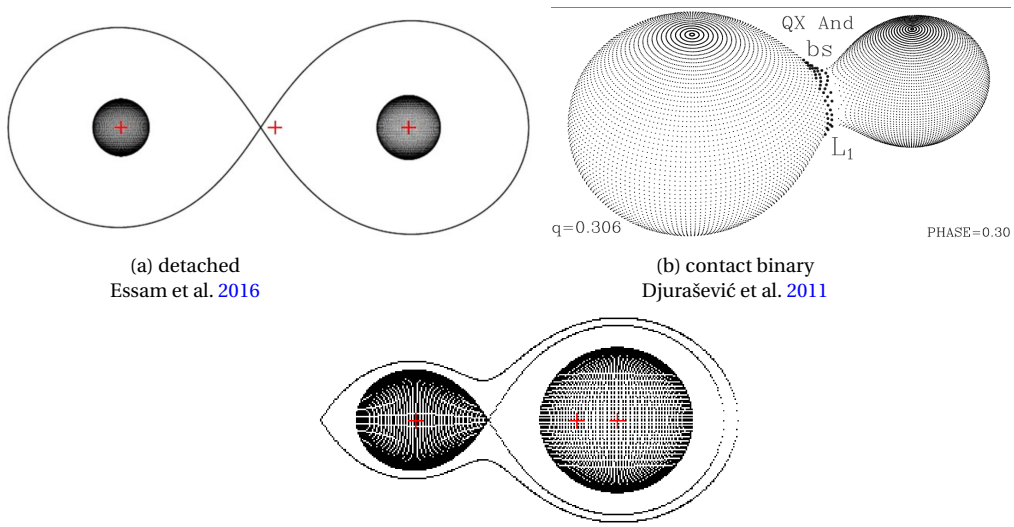

(a) detached
Essam et al. 2016

(b) contact binary
Djurašević et al. 2011

(c) Semi-detached
Öztürk and Erdem 2023

Figure 6: Roche lobe geometries of binaries

In **detached binaries**, neither of the components fills its Roche lobe. This means that there is no mass transfer between the two components and they do not significantly interact with each other.

In **semi-detached binaries**, one component fills its Roche lobe. As soon as this happens, a Roche lobe overflow (RLOF) starts, meaning that the RLOF star starts transferring mass to the companion. This transfer of mass can be either stable or unstable, which can make the evolution of both components more complex. Stability of mass transfer can be inferred by the adiabatic response $\zeta_{\rm ad} \equiv {\rm d}\log R_{\rm d}/{\rm d}\log M_{\rm d}$ of the donor star's radius $R_{\rm d}$ losing mass $M_{\rm d}$ compared to the response of its Roche lobe $\zeta_{\rm R} \equiv {\rm d}\log R_{\rm L}/{\rm d}\log M_{\rm d}$ and it is stable if $\zeta_{\rm ad} > \zeta_{\rm L}$ or the inequality only flips temporarily and changes back to the stable state with $\zeta_{\rm ad}$ becoming bigger again (Temmink et al. 2023). In Fig. 8, the primary star fills its Roche lobe, making the star start to transfer mass to the companion.

The components of **contact binaries** are so close together that both stars have an RLOF. They may even share their gaseous envelopes, resulting in a common envelope (CE). Contact binaries transfer mass to each other (Lucy and Wilson 1979), making their orbital period subject to change due to loss of angular momentum or transfer of mass (e.g. Liu et al. 2024).

In total, the components in detached binaries mostly evolve independently like single stars, while in semi-detached and in contact systems the evolution of the system's components can be completely altered. In contact and semi-detached systems, the components can then be located on different isochrones.

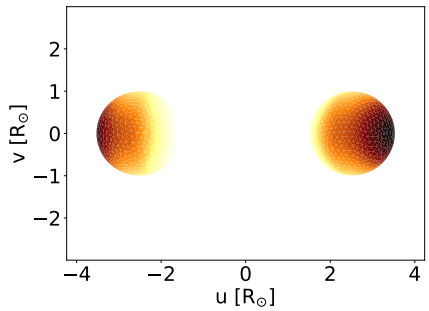

Figure 7: Mesh plot of the default detached binary, created with PHOEBE. The colours depict the temperature with yellow being hotter than the brown parts An effect of illumination can be seen on the sides of the stars facing each other. The u and v coordinates are relative to the barycentre and the orbit is in the v plane

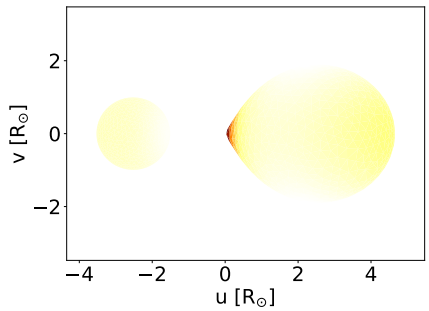

Figure 8: Mesh plot of the default semi-detached binary, created with PHOEBE. The colour coding and coordinate system are the same as in Fig. 7. A temperature decrease at the centre (Lagrange point L_1) happens because the matter becomes unbound from the Roche-lobe filling star

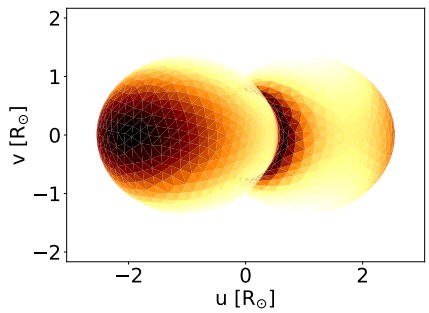

Figure 9: Mesh plot of the default contact binary system, created with PHOEBE. The same colour coding and coordinate system is used as in figure 7. This figure shows that both stars have a RLOF and their envelopes overlap, thus being in contact and making it a contact binary

1.2 Massive binaries

It is common to classify stars as massive when they exceed the value of $8M_\odot$. This mass is the boundary of different evolutionary ends of stellar lives. Stars above this mass will eventually collapse in a core-collapse supernova (also known as type II supernova), resulting in either a neutron star or a black hole. Stars below this limit will expel their outer layers and their remnant is a white dwarf, a star that does not produce energy itself through nuclear fusion and cools down over time. The evolutionary tracks of massive stars from $5M_\odot$ are shown in Fig. 10.

Stars in the range 10 to 30 $M_\odot$ evolve to blue (BSG) and yellow supergiants (YSG) after they leave the main sequence (see Fig. 10) and the most massive stars with masses higher than $20M_\odot$ can become a Wolf-Rayet (WR) star. WR stars are among the hottest and most massive stars known.

The mass of a star has a huge impact on the main sequence lifetime and massive ones stay in the main sequence for only a few to some hundreds of millions of years. However, the majority of their lifetime is passed in the main sequence and phases related to supergiants or WR phases only last for a brief moment.

In massive binaries, an RLOF starts occurring as soon as the primary star expands past its Roche lobe, increasing significantly its radius and changing the physical configuration from a detached to a semi-detached system. This mass transfer happens to be unstable above a critical mass ratio (Pellouin, Dvorkin, and Lehoucq 2024) and is otherwise stable.

Another important orbital parameter of massive binaries is the orbital period and the semi-major axis which determine how far away the components are from each other. They are related to Kepler's laws of motion, which is described in section 1.1.3. When both values are high (i.e. the stars have a high separation), the stars will not interact with each other and their evolution behaves like two single stars. However, if the stars are close by, meaning the semi-major axis and the orbital period are low, this means that interactions among the components are likely happening and can be a transfer of mass, circularization of the orbit and even a merger of both stars to

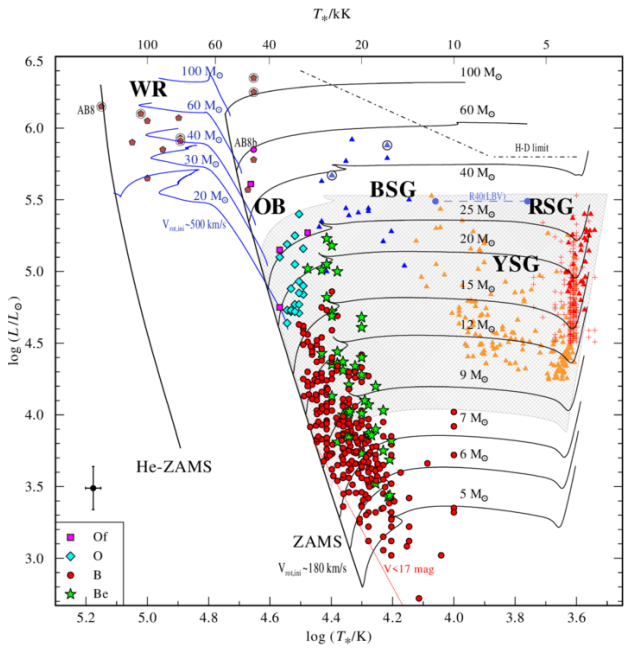

Figure 10: Evolutionary tracks for massive stars. This HRD shows massive stars in the Small Magellanic Cloud (SMC). The red dots represent B-type stars, the green stars are Be-stars (B-type stars showing emission lines), the blue diamonds are O-type stars, the blue triangles show the blue supergiants (BSG), the yellow symbols show yellow supergiants (YSG), the red crosses and the red triangles are the red supergiants (RSG), the purple squares are Of stars (O-type stars with nitrogen emission lines) and the brown pentagons show Wolf-Rayet (WR) stars and are encircled if in a binary. The Zero-age main sequence (ZAMS) and the Helium-ZAMS as well as the Humphreys-Davidson (HD) limit are also indicated in this figure. Taken from Ramachandran et al. 2019.

a single star can be the result.
A correlation between the primary mass and the binary fraction was found (e.g. Duchêne and Kraus 2013, Offner et al. 2023). It states that the more mass the primary has, the more likely it is a member of a binary system, which can be seen in Fig. 1. The massive stars are among those whose likelihood of being in a binary system is the highest.

This means that most massive stars (spectral types O and B) are members of binary systems. However, the observed binary fraction is mostly lower than the intrinsic (true) one because there is always a probability of missing binaries with observational campaigns (Marchant and Bodensteiner 2023). These limitations arise from measuring the radial velocities and selection effects favouring binaries of similar brightness. Massive binaries tend to be in close orbits, making most of them interact with each other during their lifetime (Marchant and Bodensteiner 2023), especially after the primary leaves the main sequence. Sana et al. (2012) observed O-type stars, the most massive stars, in Galactic open clusters. They found out that interaction processes have a high impact on how the binary system evolved over time and only a small fraction of them (about 29%) remain undisturbed until they undergo a supernova explosion. About a quarter of the stars eventually merge. The envelope of them is getting stripped at a third of the systems and 14% of the binaries will get into an accretion or common envelope phase (Sana et al. 2012). They mention that the orbital period and the mass ratio at the beginning are the main factors that impact how such systems will interact later.

1.3 B-type binaries

B-type stars are relatively massive, but not the most massive ones. They have effective temperatures ranging from 10,000 to 30,000 K and masses ranging from 2 to 16 $M_{\odot}$ (Daszyńska-Daszkiewicz and Miszuda 2019). B-type stars feature strong neutral helium absorption lines and hydrogen lines (e.g. the Balmer lines) are dominating the star's spectrum.
B-type stars are more numerous than the more massive O-type stars as it is suggested by the initial mass functions (IMFs) from Salpeter (1955) and Pavel Kroupa (2001). The relative abundances of stars depending on the mass is illustrated in Fig. 11. And the majority of the core-collapse supernovae progenitors are early B-type stars, making them a subject of interest to study, especially their evolution and interactions among the companions in a binary.
The rotational synchronization of B-type stars in 30 Doradus was observed by Lennon et al. (2024). When stars are in close binaries, tidal effects become significant which can cause the stars to synchronize the spin period to the orbital period. Binary stars with periods under 3 days are almost always synchronized whereas systems with periods of more than 10 days must be asynchronous (Lennon et al. 2024). This synchronization is relative to the mean angular velocity in the orbit rather than the angular velocity at periastron.
Since many massive stars are located in close binaries (Marchant and Bodensteiner 2023), it can also happen that the stars occult each other regularly. These systems are called eclipsing binaries. This type of binaries will be explained in more detail in

section 1.7.
Moe and Di Stefano (2015) investigated 221 eclipsing binaries with B-type main sequence stars with masses of $\approx 4-14 M_\odot$ and mass ratios $q = m_2/m_1 > 0.2$ in the Large Magellanic Cloud. Their orbital periods are in the intermediate range between 20 and 50 days. They found a correlation between the age and the crowdedness of the eclipsing binaries, describing that the younger systems tend to be in more crowded regions. They found a significantly higher fraction of low mass ratios $\approx 0.2-0.3$ as compared to shorter orbital periods, meaning the accretion was less competitive during the formation process.

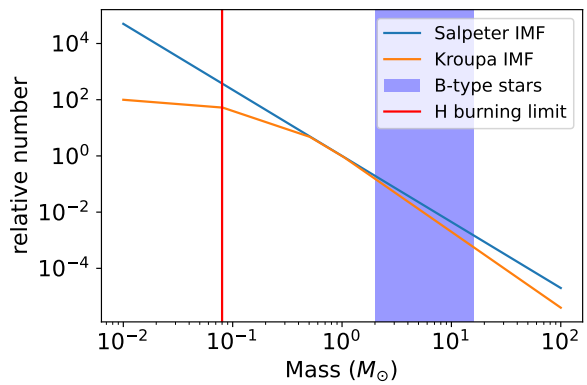

Figure 11: Salpeter and Kroupa IMFs. They show that B-type stars are less numerous than stars of solar mass or less massive stars but more abundant than the most massive O-type stars

1.4 Large Magellanic Cloud and 30 Doradus

The Large Magellanic Cloud (LMC) is one of the Milky Way's satellite galaxies, being around 160,000 light-years (~ 50 kpc) away from the Milky Way (Pietrzyński et al. 2013). It has an estimated total mass of $1.38^{+0.27}_{-0.24} \cdot 10^{11}\ M_\odot$ (Erkal et al. 2019), which is about a third of Milky Way's mass within 50 kpc. The LMC has a bar in the centre that can be seen for stars with metallicities greater than [M/H]=-1.5. It shows that the radial profile of the LMC can be described as exponentials, however, the scale height depends on the metallicity and ranges from 2.3 kpc at [M/H]=-2.3 to 0.75 kpc at [M/H]=-0.25 (Frankel et al. 2024). The mean metallicity of the LMC was determined to be [M/H]=-0.42 (Li et al. 2024).
Like many other irregular-shaped galaxies, the LMC contains lots of dust and gas in its interstellar medium. This gas is involved in star-forming regions such as 30 Doradus. The 30 Doradus region is an H II region (region of ionized hydrogen) inside the LMC. It is the most energetic star-forming region, not only in the LMC, but also in the galactic neighbourhood (Fahrion and De Marchi 2024), causing it to have many young, massive stars, and they have been observed by both spectroscopic and

photometric surveys.
In its core, it contains the open cluster R136, an exceptionally young cluster (1-2 Myr) and contains the most massive stars known (Townsley, Broos, and Povich 2024). It is a region of high scientific interest because it is an association of the most massive stars that are currently known. According to Schneider et al. (2018), there are no stars younger than 1 Myr, meaning that either the star formation ceased one Myr ago or the very young stars are still hidden in the formation cloud. Because of this young age, these stars have not evolved off the main sequence so there are no red supergiants or luminous blue variables or supernova explosions.

1.5 Spectroscopic observations of B-type binaries in the LMC

There have already been some observations on B-type binaries in the LMC and, most importantly for this work, in the 30 Doradus region. There have been spectroscopic surveys from the VLT Flames Tarantula Survey (VFTS, Evans et al. 2011) and a follow-up study from the B-type binaries characterization programme (BBC, Villaseñor et al. 2021).

1.5.1 VLT-FLAMES Tarantula survey

The VLT-FLAMES Tarantula Survey (hereafter VFTS) is an ESO Large programme that obtained multi-epoch spectroscopic data from more than 800 massive stars in the 30 Doradus region (Evans et al. 2011). One of the main objectives of the VFTS is to examine the multiplicity of massive stars. 342 of those have been classified as O-type stars by Walborn et al. (2014) and 438 as B-type stars by Evans et al. (2015). Schneider et al. (2018) states that the inferred IMF has a smaller slope than the Salpeter IMF (Salpeter 1955) with stars up to $200 M_{\odot}$. The mass distribution transitions from a plateau to a negative power law at about $15 M_{\odot}$ (Schneider et al. 2018).
They also found that the visual extinction in the 30 Doradus region is relatively low but distributed inhomogeneously.

Dunstall et al. (2015) focused on the multiplicity properties and the binary fraction in 30 Doradus. With an observed binary fraction of $f_{\rm obs} = 0.25 \pm 0.02$ and synthetic populations models together with correction of observational biases, they inferred a true binary fraction of $f_{\rm true} = 0.58 \pm 0.11$ for B-type stars.
The spectroscopic classification and radial velocity analysis was carried out by Evans et al. (2015). Most of the stars were not digitally classified before and the ones that were had lower-resolution spectroscopy. For Giants (luminosity class III) and for main-sequence stars (luminosity class V), a series of lines and their intensities were used to classify stars. Due to the high temperature ranges, different spectral lines were taken to determine the radial velocities. However, the Balmer series was left out because of high nebular contamination.
The physical parameters of B-type main sequence binaries were subject for Garland et al. (2017). The effective temperatures were estimated using the Si III ionization balance or the line profiles of He II $\lambda 4542$ and $\lambda 4686$. The surface gravity $\log g$ was estimated by comparing the observations at the Hγ and Hδ line with theoret-

ical models. The broader the spectral lines become, the higher the surface gravity becomes. However, 13 targets showed significant $T_{\rm eff}$ uncertainties because these aforementioned features were not present. These targets mostly have a range of $T_{\rm eff}$ of 20000 to 26000 K. which is typical for early B stars.
Sana et al. (2013) studied the multiplicity fraction of 360 O-type stars in 30 Doradus. For identification of binaries, they used the RV variability method and set a threshold of 20 kms^{-1}, which 36% of the systems passed and are likely spectroscopic binaries. 46% of the sample showed significant RV variations. Almeida et al. (2017) analyzed spectra of 93 O-type and 9 B-type binaries in 30 Doradus. Being a follow-up study from Sana et al. (2013), they focused on the radial velocities (RV) to get orbital solutions. After they are obtained, statistical distributions for different orbital parameters such as the mass ratio q, the orbital period P and the eccentricity e were visualized by Almeida et al. (2017).
The atmospheric parameters of B-type supergiants with the combination of nitrogen abundances were analysed to get the width of the main sequence (McEvoy et al. 2015).

1.5.2 B-type characterization programme

The B-type binaries characterization programme (hereafter BBC) is a spectroscopic study of 88 early B-type stars in the 30 Doradus region, spanning over 29 observational epochs (Villaseñor et al. 2021). These objects were identified to show RV variability by Dunstall et al. (2015) and the BBC is a follow-up study of these systems. The data was acquired through the FLAMES/GIRAFFE spectrograph and it is publicly available through the ESO data portal [1] under the program ID 096.D-0825(A) with the PI Taylor. Binarity was confirmed for 64 of these systems and 20 more show periodicity, but the periods were more tentative (classified as SB1*). This sample is the biggest homogeneous one that has orbital solutions for this type of star.
Out of the sample, 50 are single-lined spectroscopic binaries (SB1), meaning that the spectral lines of only one component can be resolved. The other 14 systems are double-lined spectroscopic binaries (SB2) where the spectral lines of both components can be seen. This makes a total of 84 systems where orbital solutions, containing the orbital period P, the eccentricity e, the argument of periastron ω, time of periastron passage T_p, the semi-major axis $a\sin(i)$, the systemic velocity γ as well as the half-amplitude of the primary K_1, were presented. These solutions were obtained via fitting Keplerian orbits to the RV data with the `RVFIT` code (Iglesias-Marzoa, López-Morales, and Morales 2015). The statistics of the orbital periods are not significantly different to B-type stars in the Galactic OB association Cygnus OB2 (Kobulnicky et al. 2014), which is illustrated in Fig. 12. The Tarantula Massive Binary Monitoring (TMBM, Almeida et al. 2017) aimed at characterizing massive OB starts that have been identified. With multi-epoch radial velocity measurements of 102 stars in 30 Doradus, orbital parameters were obtained to fill gaps in the parameter space because no direct measurements outside of the Milky Way were available before this study.

[1] https://archive.eso.org/eso/eso_archive_main.html

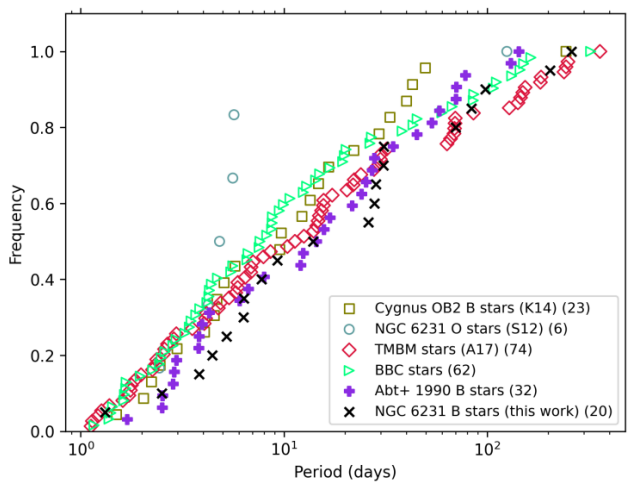

Figure 12: Comparison between B-type binaries in the Galactic association Cygnus OB2 (olive-green squares) and in 30 Doradus (light green triangles). NGC 6231 is a Galactic open cluster in the constellation of Scorpius and their O stars have been studied by Sana et al. 2012. The Tarantula Massive Binary Monitoring (TMBM, Almeida et al. 2017) was carried out on O stars in 30 Doradus. Abt, Gomez, and Levy (1990) studied 72 stars of spectral type B2-B5 with a luminosity class of IV and V. Taken from Banyard et al. 2022.

1.5.3 Other spectroscopic studies of massive eclipsing binaries

Only a few stars with masses of more than $30M_{\odot}$ were known to be eclipsing before the analysis of Koumpia and Bonanos (2012), allowing to get constraints on the masses, radii to compute evolutionary models. Koumpia and Bonanos (2012) reduced MIKE (Bernstein et al. 2003) spectroscopic data from four eclipsing binaries in the young Galactic stellar cluster Westerlund-1. With these eclipsing binaries, an independent way is found to determine the distance to the cluster.
The individual star HMI 8, a massive eclipsing binary, was observed with spectroscopic data from MIKE, FEROS and an echelle spectrograph and the data was analyzed by Rodríguez et al. (2021). With the high-resolution spectrgraph, it can be seen that HMI 8 is a double-lined spectroscopic binary (SB2), allowing to get constraints on the mass ratio and modelling the radial velocity of both components, helping in the spectral disentangling.

1.6 Photometric observations

1.6.1 Limitations of spectroscopic-only observations and need for photometric data

With spectroscopy, one can determine some parameters such as the orbital eccentricity, the period, the semi-amplitude and the mass ratio for SB2 systems. However, the masses, the radii and the rotational velocities have high uncertainties, especially

if the signal-to-noise ratio (SNR) and the spectral resolution $R = \lambda/\Delta\lambda$ are low. The inclination can be tightly constrained with the help of photometric data to precisely get values for the masses and the rotational velocities with no unknowns.
Zasche and Wolf (2019) also mentioned that photometry only does not get the full set of orbital and stellar parameters of the binary. This in total emphasizes that there is a need for *both* spectroscopic and photometric data to precisely determine the physical parameters and therefore their evolutionary state.

1.6.2 Optical Gravitational Lensing Experiement

The Optical Gravitational Lensing Experiment (OGLE) is a multi-decade photometric survey to monitor the variability of over a billion sources, particularly targeting the Milky Way bulge and in the Magellanic systems with its fourth data release (OGLE-IV, Udalski, M. K. Szymański, and G. Szymański 2015). The project started in the early 1990s and obtained photometry since then. Over 2000 gravitational lensing events are captured per year and exoplanets were discovered by the transit method. Photometric variability can come in different shapes. But it always means that a star changes its photometric brightness over time. Some stars, the so-called Cepheids, have pulsating envelopes and their brightness increases when they expand and when they contract again the brightness drops. Eclipsing binaries have characteristic dips when one star occults the other in a binary system (see section 1.7 for more details).
The first phase of the OGLE (OGLE I) survey lasted from 1992 to 1995 and was conducted using a one-meter telescope in Las Campanas Observatory in Chile. Due to time constraints when accessing the telescope, only the Galactic bulge could be regularly monitored (Udalski et al. 1992). The first microlensing events were discovered in the direction of the Galactic centre with this survey.
In 1996, a new 1.3-metre telescope (called the “Warsaw Telescope“) dedicated to OGLE became operational at Las Campanas observatory. The second phase (OGLE II), therefore, had more time available to monitor more objects. Its main goal was to increase the number of detections of microlensing events in both the Milky Way and the Magellanic systems. An automated procedure was implemented to significantly increase the number of detections(Paczynski et al. 1997).
The third phase (OGLE III) started in 2001 with an instrumental upgrade and it remained one of the biggest optical sky surveys in the first decade of the 21st century (Udalski 2003). With the help of new astronomical software (Difference Image Analysis technique, Alard 2000) and the favourable weather conditions at Las Campanas observatory, a photometric accuracy of the order mmag can be achieved. Transits and microlensing events were used in this survey to discover exoplanets. The photometric data for the analysis of this thesis comes from both OGLE III and OGLE IV.
OGLE IV started its regular observations in 2010. With its experience in measuring photometric data in crowded fields like 30 Doradus, it is valuable in conducting variability studies in these fields. Between 100 and 700 epochs per system were collected in I and V bands in this phase (Pawlak et al. 2016). They also focused on the OGLE sample in the Magellanic clouds. Out of 48605 systems, 40204 belong to the LMC and 8401 to the SMC. This is made possible by a mosaic of 32 CCD cameras covering a field of view of 1.4 deg^2 (Pawlak et al. 2016).

1.6.3 Other photometric studies

A sample of more than 4600 eclipsing binaries of bright, early-type (mostly B and A) stars in the SMC and the LMC has been observed by Faccioli et al. (2007). They made a detailed analysis of the period distribution and they found a strong peak between 0.8 and 4 days, while having a tail from 10 to 100 days. They already conducted light curve analysis with PHOEBE, though with an older version of the software package (A. Prša and Zwitter 2005).
Eclipsing binaries can also be observed by surveys that are primarily dedicated to detecting exoplanet transits. One example is the work of IJspeert et al. (2024). They made a catalogue for more than 14000 eclipsing binaries from spectral type O to F, using data from the Transiting Exoplanet Survey Satellite (TESS). TESS features much shorter cadences ranging from 2 to 30 minutes (Andrej Prša et al. 2022) than OGLE with 1 to 3 days in the Magellanic systems (Udalski, M. K. Szymański, and G. Szymański 2015). Their focus was on orbital circularization. This means that an orbit's eccentricity is decreasing due to tidal forces until the orbit gets circular. This orbit circularization is also undergoing in contact binary systems.
A more recent work from Mahy et al. (2020) focused on 13 SB2 binaries with O-type primaries in 30 Doradus and the data was analysed with PHOEBE. They classified the systems into their configurations (detached, semi-detached, (over-)contact or uncertain) with the ratios of the radii to the Roche lobe filling factor.

1.7 Eclipsing binaries

Binary systems can have different orientations as viewed from Earth. In some cases, this leads to periodic occultations of the stars, causing the received flux from the system to decline periodically. An example plot of a light curve of an eclipsing binary is shown in Fig. 13. This is the variability in brightness of eclipsing binary systems.

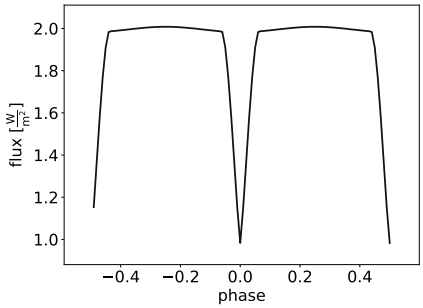

Figure 13: Example light curve plot of an eclipsing binary model, created with PHOEBE

Eclipsing binaries show the characteristic drops in the light curve where the flux reduces significantly compared to the continuum flux when no star is eclipsed and

the full flux reaches the observer. The panels in Fig. 14 show a configuration of eclipsing binaries at three different inclination angles.
A valuable property of eclipsing binaries is that the inclination of the system can be tightly constrained. On the one hand, an inclination of 90 degrees represents an edge-on view, meaning that the observer is located in the orbital plane of the stars. On the other hand, when the system's inclination is 0 degrees, there is a face-on view. It is obvious that the higher the inclination, the more likely the stars eclipse each other. Figure 14 shows the configuration of a binary system at three different inclination angles. Fig. 14a represents an edge-on view. Fig. 14c shows a face-on configuration and Fig. 14b illustrates an in-between situation.

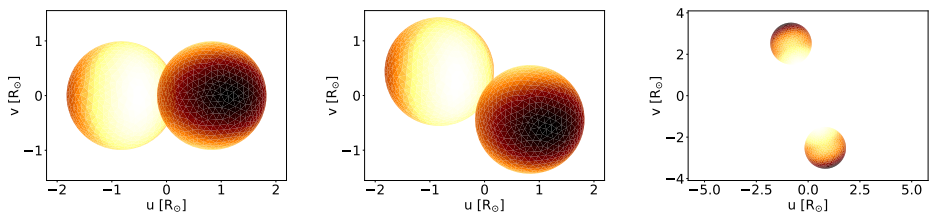

(a) $i = 90°$ (b) $i = 80°$ (c) $i = 0°$

Figure 14: Mesh plots at different inclination angles, created with `PHOEBE`
When viewing edge-on, the stars can completely eclipse each other, making the dips in the light curve the biggest. If the inclination is still high but lower than 90 degrees, the depth of the eclipse decreases since only a part of the star gets eclipsed. A face-on view does not allow the observer to see eclipses at all.

Figure 15 shows the impact of five different parameters on the light curve. Fig. 15a shows that the higher the primary radius, the deeper the eclipses become relative to the continuum flux. In Fig. 15b, it becomes clear that the higher the secondary temperature relative to the primary temperature (6000 K) becomes, the more equal the eclipse depths become. Eclipsing binaries are therefore valuable objects to constrain the effective temperatures because the ratio of the depths of the eclipses heavily depends on the ratio of effective temperatures. Fig. 15c shows the impact of the eccentricity, making the eclipse timing more asymmetric as the eccentricity increases. The higher the inclination, the deeper the eclipses become, keeping the other parameters fixed (15d). The mass ratio affects how far the stars are relatively located at a fixed orbital period, thus also showing (minor) effects on illumination and eclipse depths (15e).

1.8 Open issues in stellar evolution of massive B-type binaries

As was seen from the initial mass functions, the amount of B-type stars is significantly lower than the solar-type stars. Because of that, there are still some open questions that are not yet satisfactorily answered.
An aspect is the mass loss rate during the lifetime of a B-type star. It is known that B-type stars expel a significant amount of their mass from stellar winds (see Vink

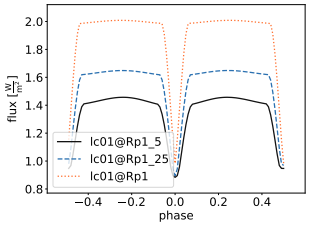

(a) primary radius

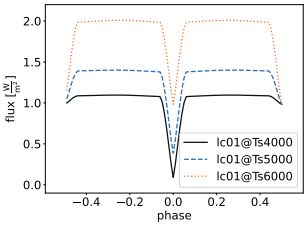

(b) secondary temperature

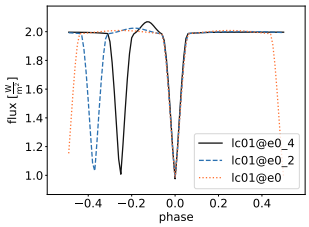

(c) eccentricity

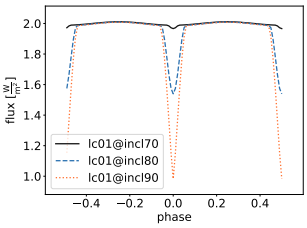

(d) inclination

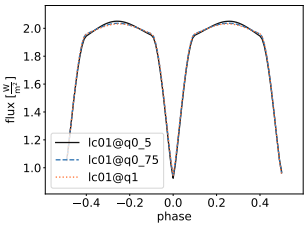

(e) mass ratio

Figure 15: Impact of different parameters on the light curve. All plots created with PHOEBE.

2022).
Another point is how the stellar rotation affects the evolution, especially how it is related to the stellar winds and the mass loss.
Finally, it is not fully understood which remnants are left behind after a B-type star dies. Moe and Di Stefano (2017) discussed period and mass ratios in binaries and mentioned as well that B-type stars are progenitors of compact remnants, not specifying it but it could be either white dwarfs, neutron stars or even black holes since B-type stars cover a large range of masses.
And in binaries, especially the massive binaries, it remains not well known how the mass transfer rates behave, causing high uncertainties in modelling a mass transferring system with evolutionary models. Scowen et al. 2019 discussed *PolStar*, a mission targeting massive stars and their environments with the help of spectropolarimetry in the ultraviolet (far-UV). It measured with a resolution of 30000 and simultaneously the four Stokes parameters. This is done using magnetic and wind environments to constrain the effect of mass loss on stellar evolution.
The appearance of the products of a massive binary that underwent a phase of mass transfer is still poorly studied. Gosnell et al. (2019) focused on white dwarfs and blue straggler stars after a phase of mass transfer but it did not deeply focus on stars that are both still in the main sequence.
The question of whether a phase of mass transfer extends the stellar lifetime is also a subject of current research. A concept of rejuvenation is that a star can appear to be younger than its actual age due to mass transfer.

1.9 Scientific aim of the work

At it was mentioned in the section of eclipsing binaries (sect. 1.7), they allow astronomers to precisely determine the effective temperatures and stellar radii of two stars. Since they are located in a binary, this shows that both stars have formed at the same time, thus having the same age.
The temperatures and the radii allow placement in a $L - T_{\mathrm{eff}}$ diagram. The placement of the two components is compared with isochrones to check whether both components fit on the same isochrone or not; Therefore, two possible cases can occur.
If there is a common isochrone found that matches the position of both components, it means that there is no evidence of mass transfer in that binary system.
If the components do not fit on the same isochrone, it can either be the case that the models used to produce the isochrone are inaccurate because of the uncertainties of the models or that this is evidence of both stars having undergone a phase of mass transfer, the former case being less likely.
This thesis opts to perform these tests under the use of a sample of eclipsing binary stars in the LMC that have existing orbital solutions obtained by spectroscopy.
To get the effective temperatures and the radii of the eclipsing binaries, three fundamental steps are followed. Firstly, the photometric data is analysed with period-search methods to obtain a period and to phase-fold the data accordingly. Then, `PHOEBE` will be used to model the light curves by finding the optimal fit of a model to the observational light curve. The uncertainties of these parameters are then es-

timated by sampling around the solution. When this process is done, values for the temperatures and radii are obtained. The temperatures and the luminosity, which relate both the radius and the temperature, are returned and the position in the $L - T_{\text{eff}}$ diagram is compared with LMC-like isochrones.
The primary goal is to see how often the isochrones fit into the systems and how often not to see how frequent mass transfers happen across B-type stars.
In section 2, the methods used to perform the analysis are explained, containing the period determination in section 2.1 as well as the modelling in section 2.3 with approaching a solution and the sampling around it to estimate uncertainties. Section 3 provides the results for the stellar parameters as well as their plots on a HRD. Section 4 will discuss and interpret the results, that will be concluded in section 5. The work will eventually be summarized in section 6.

2 Methodology

To identify the eclipsing binaries and determine their physical parameters, I used the combination of the spectroscopic data coming from BBC (Villaseñor et al. 2021) and the OGLE photometric data (Pawlak et al. 2016). In this case, the spectroscopic data has already been processed so that spectroscopic periods, eccentricities and the half-amplitudes values are already available. The goal is to obtain constraints for the effective temperatures, radii and inclination of the systems with the OGLE data, validate the spectroscopic results and fully determine the parameter space of the systems. The first step I did is a search for the orbital period by periodogram analysis and then the data will be phase-folded accordingly. After that, `PHOEBE` will be used to set some initial model parameters, setting them closer to the light curve data. When a sufficient agreement between the model and the observational data is visible, `Nelder-Mead`, an optimizer is run to refine the parameters until the solution converges. Finally, `EMCEE` is applied to get estimates of parameter uncertainties and correlations between them.

2.1 Period determination

The first step of the analysis is to find the photometric period of the system. For that, periodograms are used. A periodogram analyses the data and returns a power spectrum with several peaks that can be the true period of a system. There are different periodograms available, of which two (Lomb-Scargle and Box-Least-Squares) were used for the period search in this work.

2.1.1 Lomb-Scargle

A Lomb-Scargle periodogram (Lomb 1976, Scargle 1982) returns the power of a searched period by fitting sine curves to the data. The better the sine waves match the data, the higher the Lomb-Scargle power for this period will be, resulting in a periodogram showing this power depending on the periods. The periodogram for the system VFTS 189 is shown in Fig. 16 as an example. The crosses there are to mark which

peaks have been marked as significant and the light curve was phase-folded accordingly. The lines at the bottom represent the false-alarm probabilities (FAPs) of 10%

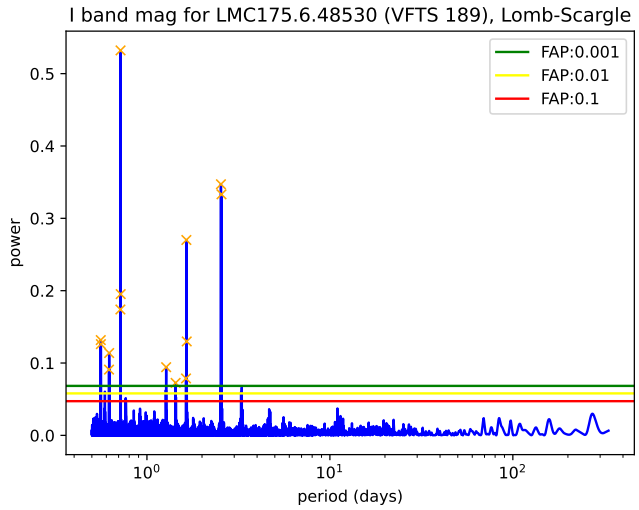

Figure 16: Lomb-Scargle periodogram for LMC175.6.49530 (VFTS 189)

(red), 1% (yellow) and 0.1 % (green). An FAP of 0.1% means that the peak at this period has a probability of 0.1 % of being arisen from random signals. The lower the FAP is, the more likely it is that a detected period is a true periodic signal.
For VFTS 189, the system shown in Fig. 16, several peaks are likely showing periodic signals when phase-folded. Therefore, one has to look at the phase-folded data for some peaks because the highest peak is not necessarily the true orbital period of the system. This system, for example, yielded the highest Lomb-Scargle power at a period of just over 0.7 days, but the data does not reveal the eclipses correctly, as shown in Figure 17. In this case, both the primary and the secondary eclipse are located around the same phase of about 0.3. This means that the period is probably wrong by a factor of 2. Figure 18 shows the phased data for VFTS 189 multiplied by this factor. In this case, the eclipses are disentangled and can be seen separately. Therefore, the multiplication by 2 yielded the correct period of this system, which could be confirmed for most eclipsing binaries by the spectroscopic periods.

2.1.2 Box-Least-Squares

The Box-Least-Squares (BLS) mechanism (Collier Cameron et al. 2006) is another method to perform a search for orbital periods. Unlike Lomb-Scargle, the BLS fits rectangles to the phase-folded light curve but it also returns a power spectrum related to the searched frequency. This method is used in exoplanetary transit searches because the light curve shows an approximately rectangular shape since the planets are small compared to the star in diameter. Table 1 shows the periods for the eclips-

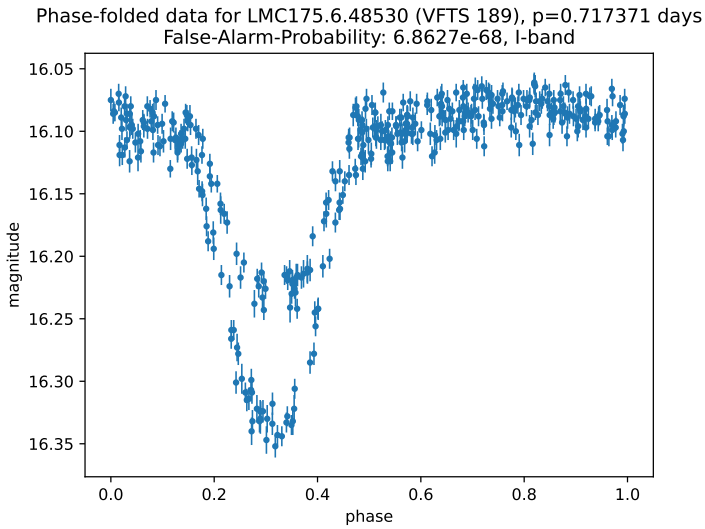

Figure 17: Phase-folded data with highest Lomb-Scargle power
Both the primary and secondary eclipse are located at around the phase 0.3

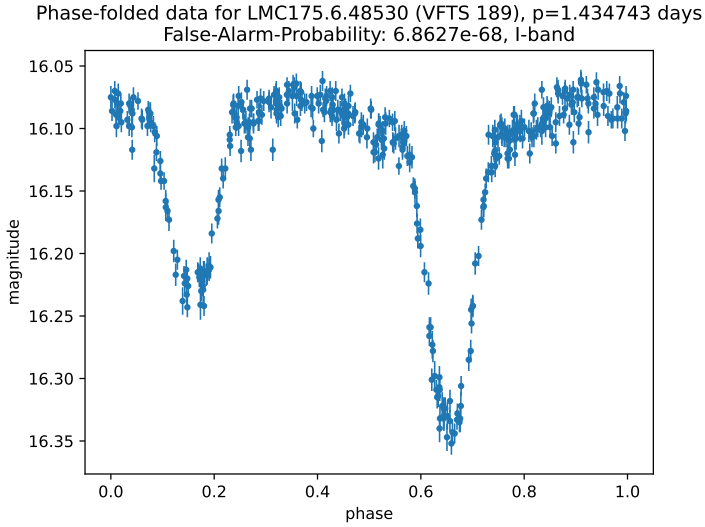

Figure 18: VFTS 189 data phase-folded to double the period of the highest peak
The primary and secondary eclipses are disentangled

ing, the ellipsoidal and the heartbeat star systems with different methods and it also compares them with the literature values in BBC and OGLE.

VFTS	SB	Var	$P_{\mathrm{BLS}}(d)$	$P_{\mathrm{LS}}(d)$	$P_{\mathrm{BBC}}(d)$	$P_{\mathrm{OGLE}}(d)$
27	SB1	ECL	6.58217582	6.582745	6.582728	6.5827068
112	SB2	ECL	1.67406948	1.674056	1.674083	1.6741191
157	SB1	ECL	12.94466945	12.945317	12.940303	12.9444695
189	SB1	ECL	1.4347787	1.434743	1.434800	1.4347451
206	SB2	DPV	215.98275983	218.235844	7.556457	7.5547969
215	SB1	ECL	4.30341003	4.304030	4.303465	4.3035700
240	SB2	ECL	1.37768355	1.377662	1.377795	1.3776837
248	SB2	ECL	2.49414788	2.494355	2.494240	2.4943809
255	SB2	ECL	2.8449009	2.844995	2.844891	2.8449050
364	SB2	ECL	4.399868	4.400090	4.399906	4.3997768
388	SB1*	HB	1.02450252	14.774035	14.792479	14.773080
430	SB1	ELL	2.59273459	2.582437	8.760079	
687	SB1	ELL	2.17114354	12.470365	12.468230	
698	SB2†	W Ser†	1.0395204	25.418534		
883	SB2	ECL	3.49536495	2.330191	3.495192	6.9908902

Table 1: Orbital period for the eclipsing binaries and the ellipsoidal variables determined by different tools
Meaning of the columns: 1) VFTS identifier; 2) SB: spectroscopic binary; SB1:single-lined, SB2:double-lined spectroscopic binary (Villaseñor et al. 2021); 3) Variability classes: ECL-eclipsing binary, ELL - ellipsoidal variable, DPV - double-periodic variable, HB - heartbeat star, W Serpentis 4) Period determined by Box-Least-Squares; 5) Period determined by Lomb-Scargle; 6) Spectroscopic period from the BBC programme (Villaseñor et al. 2021); 7) photometric period from the OGLE catalogue (Pawlak et al. 2016); † Dunstall et al. 2012. No entry in the table means that the object was not found in the catalogue.

2.1.3 Special cases with inconsistent periods

Here we comment on six objects from table 1 that present disagreements of the orbital periods from the different methods and/or sources.

VFTS 206: Both the spectroscopic and the photometric period from the catalogues showed periods of about 7.55 days. However, when looking at the phased diagram (Fig. 19, it did not show clear eclipsing signs: The highest peak in the Lomb-Scargle periodogram appeared at about 215 to 218 days which is way off the catalogue periods. But on the other side, a clear periodicity is visible. This object is already classified as a double periodic variable (DPV) in the OGLE catalogue. In this case, there is a short period of about 7.55 days and a long period of roughly 218 days, which makes this system unique among the BBC sample. Fig. 19 shows the comparison of the short OGLE period to the long Lomb-Scargle period. However, the signal does not show features of eclipsing

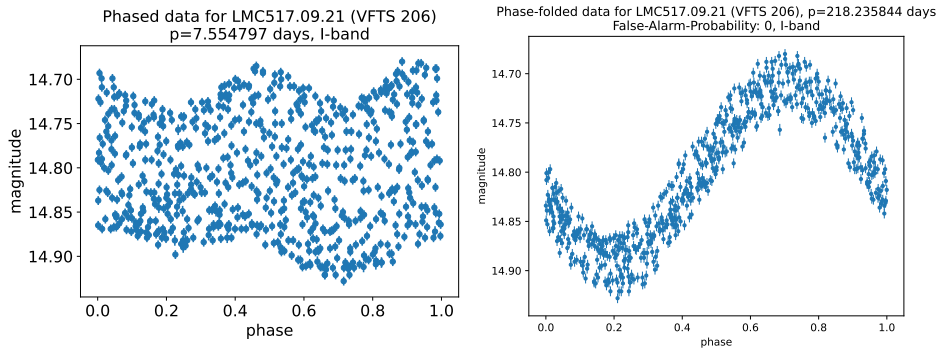

(a) VFTS 206 phase-folded data with the OGLE period

(b) VFTS 206 phase-folded with respect to the highest Lomb-Scargle periodogram peak

Figure 19: Comparison of the OGLE and the LS periods for VFTS 206

binaries that would be there if there were clear visible dips in the magnitude. Instead, the signal for the long period is clearly sinusoidal.

VFTS 388: This system is classified as a heartbeat star, meaning that this system does not show periodic flux decreases as is the case for eclipsing binaries. Section 2.2 provides a more detailed description of a heartbeat star. Instead, the flux *increases* periodically, which turned out to be problematic to detect with the BLS mechanism. The Lomb-Scargle search for periods correctly identified the period, agreeing with the OGLE and BBC periods.

VFTS 430: Both the Box-Least-Square and the Lomb-Scargle periodograms suggest around 2.59 days, in contrast to the BBC period of about 8.76 days. In this case, both the plots look really similar but the Lomb-Scargle period is about a third of the BBC period. Since this object is not classified as an eclipsing binary by OGLE, it has no period available.

VFTS 687: The Lomb-Scargle period and the BBC period are relatively close to each other but not completely agree with each other, being at around 2.38 and 2.46 days respectively. The BLS period with 1.18 days is about half the Lomb-Scargle period but it did not show a full sinusoidal curve. The plots are summarized in Figure 22.

VFTS 698: This object also has periodic features but does neither have a spectroscopic (BBC) nor a photometric period (OGLE). Dunstall et al. (2012) have classified this star as a peculiar B[e] type star with emission lines. Due to its complexity, neither the BBC programme nor the OGLE provide an orbital solution. In this case, likely periods from Lomb-Scargle and Box-Least-Square were compared but both yielded completely different results. They can be seen in Figure 23. This system has proved to have the most complicated analysis of all systems; therefore, careful individual analysis is needed, Both plots clearly show some

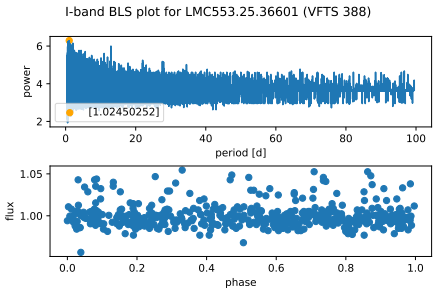

(a) BLS periodogram and phased light curve

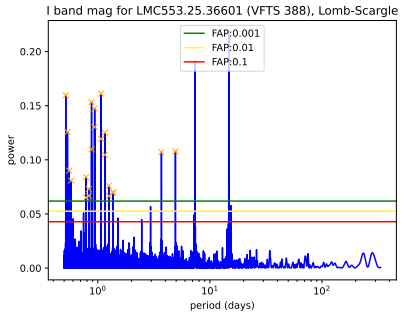

(b) LS periodogram

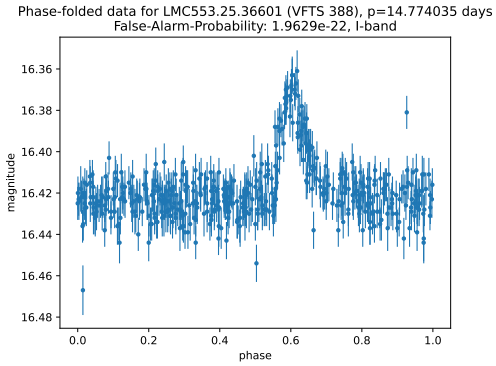

(c) LS phased light curve

Figure 20: Comparison of Box-Least-Squares with Lomb-Scargle periods for VFTS 388

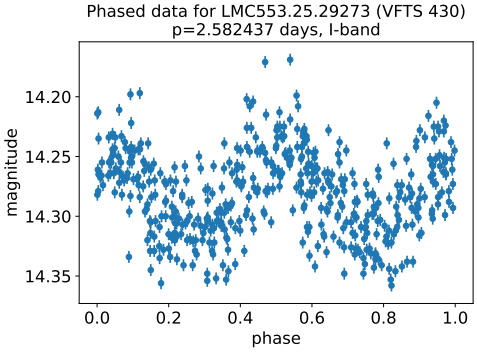

(a) LS

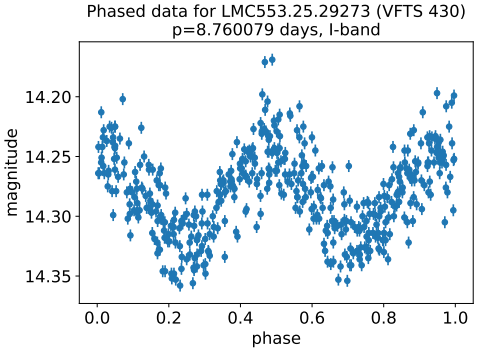

(b) BBC

Figure 21: Comparison of Lomb-Scargle with the BBC period for VFTS 430

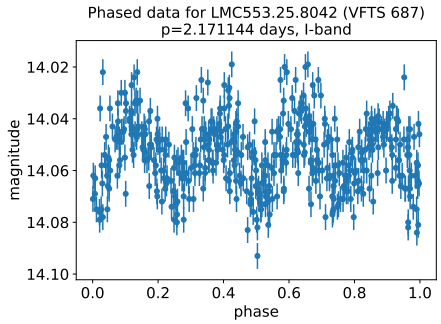

(a) BLS

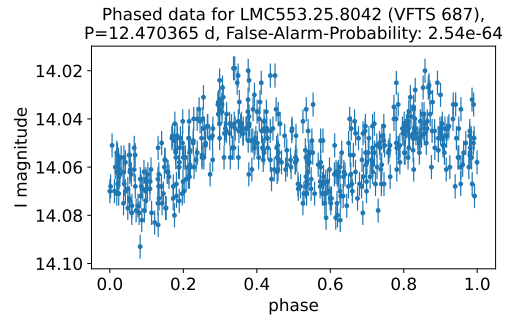

(b) LS

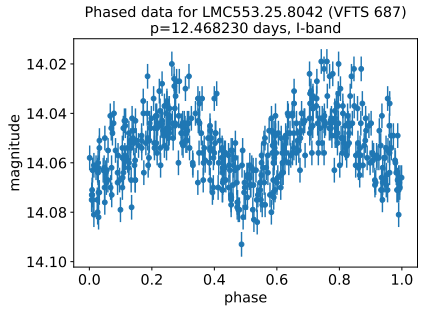

(c) BBC

Figure 22: VFTS 687 phase-folded data with respect to different methods and literature values

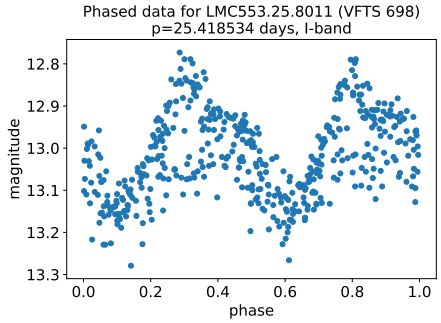

(a) LS

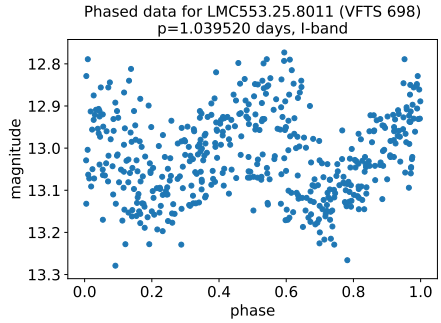

(b) BLS

Figure 23: Comparison of the phased data with respect to the LS and BLS period for VFTS 698.

periodicity, however, no eclipses are visible. The periodic behaviour is either caused by ellipsoidal variations or by pulsations.

VFTS 883: For this system, the disagreement between the different periods from the different methods is even higher. The Lomb-Scargle (LS) period is about 2.33 days, whereas Box-Least-Square (BLS) and the BBC period are about 3.495 days and OGLE even states a period of 6.991 days, making the determination of the correct period even more challenging. The comparison between the periods is shown in Figure 24. It should be noted that the OGLE period is about twice the BBC (more precisely $P_{\mathrm{OGLE}} = 2.000046 \cdot P_{\mathrm{BBC}}$) and BLS period and three times the LS period (more precisely $P_{\mathrm{OGLE}} = 3.000136 \cdot P_{\mathrm{LS}}$). In this case, all the possible periods have to be compared all to find out which one is most likely the correct one.

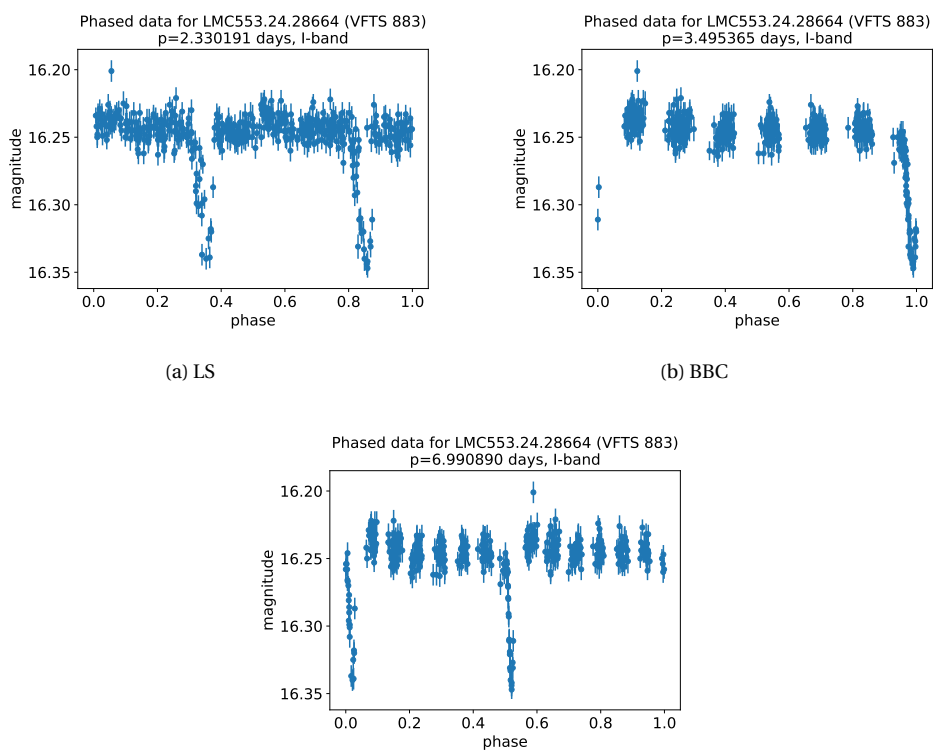

(a) LS

(b) BBC

(c) OGLE

Figure 24: Comparison of phased data with different periods from literature and methods for VFTS 883

When comparing all these periods, it becomes clear that both the Lomb-Scargle and the OGLE periods show two eclipses, unlike the BBC period where only one eclipse can be seen. The bin-like structure in the OGLE plot is likely

caused by the fact that the period is very close to a multiple of one day. Observations are only carried out at night and this becomes visible when the period is very close to an integer day value. A similar effect causes the bins at the BBC period too, but the period here is close to half of a day, making the binning still clearly visible.
Since both eclipses are still visible at the lowest of all periods (2.33 days, Lomb-Scargle), this period has the highest probability of being the true one. This would mean that the BBC and OGLE periods are 1.5 and 3 times as long as the actual period respectively. Knowing the correct period is crucial because this has an impact on the masses of both stars. From Kepler's laws, it is clear that the shorter the period is, the higher the masses of both stars have to be.

2.2 Classification of light curves

When observing binary stars through photometry, one can also discover light curves that look neither constant nor eclipsing. Two examples of this are heartbeat systems where the photometric brightness periodically increases (Fig. 25a) and ellipsoidal variables where the light curve shows sinusoidal variations (Fig. 25b). These particular systems can be even less frequent than the eclipsing ones and these are also included in the analysis of the thesis to get the physical parameters and the configuration of the system. Both a heartbeat and an ellipsoidal variability can be modelled

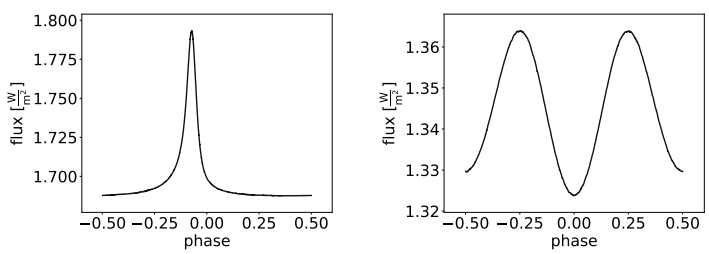

(a) Heartbeat star

(b) ellipsoidal variable

Figure 25: Heartbeat star and ellipsoidal variable light curve plots, created with `PHOEBE`

if the system's inclination is set to a low value, resulting in no eclipses occurring. While an ellipsoidal system needs a low eccentricity and both stars to be close to each other, a heartbeat system can be modelled with a comparably high eccentricity.

2.3 Initial models and optimization

The panels in Fig. 26 show the impact of various parameters on the light curve. The photometric data of the eclipsing binary VFTS 248 is shown as an example for comparison to the models. The radius of the secondary is varied in Fig. 26a, its effective temperature in Fig. 26b, , the mass ratio in Fig. 26c, the inclination in Fig. 26d and the eccentricity in Fig. 26e.

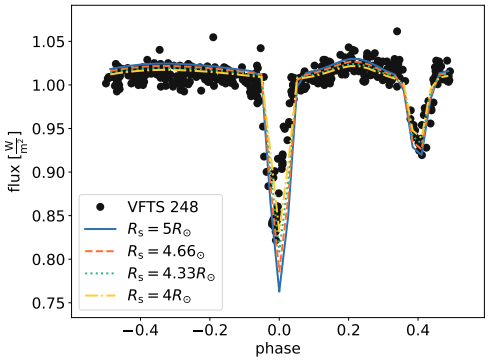

(a) $R_{\text{eqiv}}^{\text{secondary}}$

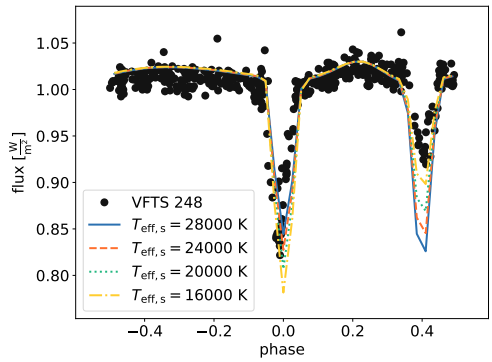

(b) $T_{\text{eff}}^{\text{secondary}}$

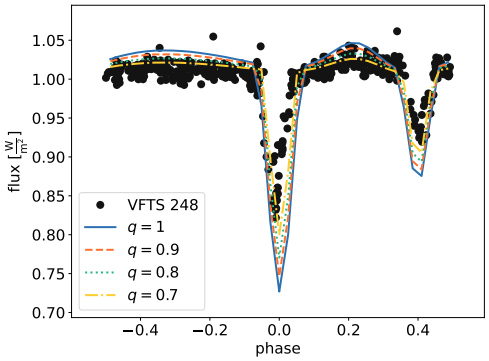

(c) q

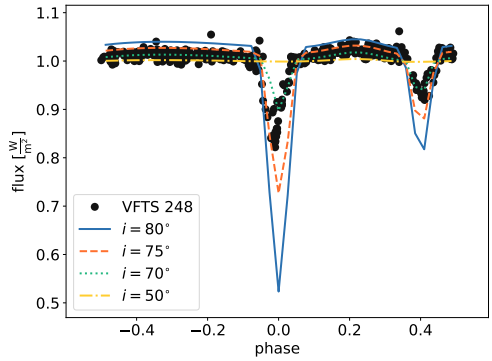

(d) i

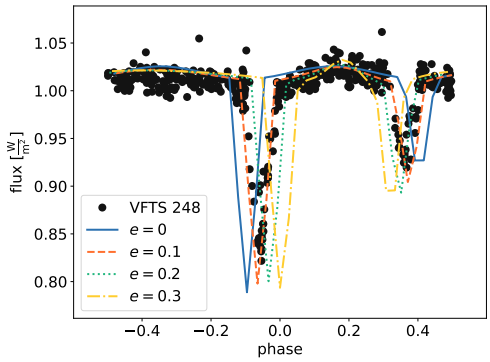

(e) e

Figure 26: Overview of the impact of different parameters on the light curve. The observational data was taken from VFTS 248

It can be seen that most parameters only impact the depths of the eclipses: A smaller secondary star means more light can reach the observer because less light is blocked during the eclipses. The effective temperature has an impact on the depth ratio and the mass ratio, in combination with the given fixed period, puts the components at the needed distance, thus also impacting the eclipses' depths. The eclipses are really sensitive to the inclination and if it is too low, the sign of eclipses vanishes. Only the eccentricity shifts the location in phase-space, depending on where the periapsis is, the time between the two eclipses is lower than the time between the eclipses when the stars pass through their apoapsis. At a circular orbit, both eclipses are separated by a phase shift of 0.5. A more detailed description of the effects that the parameters have on the light curve is described in section 2.3.1.
When a good period is found, it is time to move on to get an idea of the physical and orbital parameters, which is done by PHOEBE. A good period is defined such as that the eclipses or the ellipsoidal variability can be clearly seen. For eclipsing binaries, two distinct eclipses are expected to be seen (e.g compare Fig. 18 and Fig. 17). For the ellipsoidals, the variability must remain visible with two maxima and minima since the stars face one side twice during an orbit. This consists of two steps: Firstly a set of parameters is set until there is a good match between the phase-folded observational data and the model computed by PHOEBE. This step consists of setting values typical for early B stars such as effective temperatures of around 20000 K, and radii from 4-20 solar radii for the components based on the pattern of the light curve. Sometimes the ratio of the effective temperatures can be adjusted as well (see Fig. 26b). Adjusting the inclination (mostly around 60-80 degrees) and the mass ratio (mainly between 0.3 and 1) until the computed light curve has a similar shape to the observed one. After that, these values are taken into a model optimization with PHOEBE's Nelder-Mead optimizer. When this is finished, a possible set of model parameters according to the light curve is given. This will be explained in more detail in the sections 2.3.1 and 2.3.2.

2.3.1 Setting initial model parameters

This part of the analysis is allowing to understand the different effects of the stellar and orbital parameters on the light curve. The study of how the radii of the stars (Fig. 26a), the effective temperatures (Fig. 26b), the mass ratio (Fig. 26c), the inclination (Fig. 26d) and the eccentricity (Fig. 26e) impact the shapes and location of the eclipses in phase-space is examined here.

stellar radius: Figure 26a shows the influence of the secondary radius to the light curve, keeping all the other parameters constant.
In this case, the other parameters, namely the effective temperatures of the stars (28000 K for the primary and 13500 K for the secondary), the radius of the primary ($5R_\odot$), the inclination (78°) and the mass ratio ($q = 0.76$), were held constant.
It can be seen that both eclipses become shallower when the secondary's radius is decreased. Since the luminosity is proportional to R_{eq}^2 (eq. 1), the contribution from the secondary is significantly decreasing, thus reducing the dip

when an eclipse occurs. It can also be observed that the ratio of the eclipse depths stays constant. When a star contributes less to the total luminosity, the relative contribution to the total flux decreases during the secondary eclipse. When the primary star is eclipsed, a smaller secondary star will still let more flux from the primary reach the observer.

effective temperature: To see the impact of the effective temperature on the light curve, the effective temperature of the secondary was changed here. The other fixed parameters are the primary temperature (28000 K), the radii of the components ($5R_\odot$ for both), inclination 78° and mass ratio $q = 0.76$. This is illustrated in Figure 26b. It can be seen that the change in the effective temperature of the secondary star primarily has an impact on the depths of the eclipses. For the blue line, both effective temperatures and the radii of the stars are the same. Then both eclipses have about the same depth, and only the non-zero eccentricity makes them not exactly equal. As soon as the secondary temperature decreases and therefore also the ratio of the effective temperatures, the secondary eclipse becomes significantly shallower. However, the flux outside of the eclipses does not change at all.
The different depths of the eclipses can be explained by Stefan-Boltzmann's law, stating that the luminosity is proportional to T^4 (eq. 1). When both stars have about the same temperature, their surface brightness is also about equal (surface brightness $F = \frac{L}{4\pi r^2} = \sigma T_{\text{eff}}^4$) which means about the same flux is occulted during the eclipses. However, when the secondary star is significantly cooler than the primary, this causes the secondary to have a much lower surface brightness. This means that the dip in the secondary eclipse is relatively shallow since only a small proportion of the total flux is blocked by the primary star. During the primary eclipse, a much higher contribution, coming from the hotter primary star, is blocked by the secondary, causing the primary eclipse to be much deeper.

mass ratio: In this example, shown in Fig. 26c, the mass ratio $q := \frac{m_{\text{secondary}}}{m_{\text{primary}}}$ was varied, ranging from $q = 1$, meaning that both stars have the same mass, down to $q = 0.7$. The fixed parameters here are the primary temperature (28000 K) the secondary temperature (16000 K), the radii of the components ($5R_\odot$ for both) and the inclination (78°).
It can be seen that the mass ratio mainly has an impact on the depth of both eclipses. The higher the mass ratio, the lower the depth of both eclipses become.
The lower the mass ratio becomes, the further away the secondary star has to be from the primary to keep the same orbital period. In principle, the depth of the eclipses here is influenced by the distance between both stars. When their separation is increased, a lower amount of their surface is occulted while an eclipse happens, causing them to become shallower when the mass ratio decreases.

inclination: This example illustrates the impact of the inclination to the light curve, while the effective temperatures (28000 K for the primary and 16000 K for the sec-

ondary), the mass ratio ($q = 0.7$) and the radii ($R = 5R_\odot$) were kept constant. The illustration of these light curves is in Fig. 26d.
It is directly obvious that the inclination has a huge impact on the light curve of eclipsing binaries. An inclination of 0 degrees means a face-on view, while an edge-on view is given when the inclination is 90 degrees.
The effect of the inclination to the eclipses is mainly seen in their depth. The higher the inclination becomes, the deeper both eclipses become. This makes sense since a higher inclination makes a larger part of the surface become eclipsed. The higher the inclination, the bigger the contribution of the total star's surface to an eclipse becomes, reaching a maximum at 90 degrees (edge-on).
However, if the inclination of a binary system is too low, the eclipse is not visible from Earth because both stars are missing each other when they come close (apparently as seen from Earth). If that is the case, the binary is no longer an eclipsing one and the photometric data would not allow for precise determination of physical parameters.
However, the huge impact on the eclipse's depth is an opportunity to tightly constrain the inclination of the system and, as a result, also to other parameters of the system.

eccentricity: For all the previous examples, the eccentricity was set to 0.166, which is the value for VFTS 248 taken from Villaseñor et al. (2021). But here, I am demonstrating the impact of the eccentricity as well, which is visualized in Figure 26e.
The eccentricity, unlike the previously discussed parameters, also has an impact on the location of the eclipses in the phase diagram.
When the eccentricity is set to 0 (circular orbit), both eclipses are 0.5 in phase-space apart, meaning that they are equidistant with half the period. An increase in the orbital eccentricity results in the eclipses getting shifted in their location. When the stars reach their periapsis, they are moving faster according to Kepler's laws. For example, if the primary eclipse happens just before the periapsis and the secondary just after the periapsis, the time difference between the primary to the subsequent secondary becomes lower than the time that passes between a secondary eclipse and the next primary eclipse because the stars then pass their apoapsis, resulting in slower movement in their orbits. This is then reflected in the phase-folded curve in the following: The periapsis is placed somewhere in-between both eclipses of shorter separation in time (yellow curve at phases 0.0 and 0.3 in Fig. 26e).
The depth of the eclipses is also changing. However, this is a secondary effect here because the changes in eccentricity also affect the orbit's shape and how far the stars are from each other when eclipses occur.

2.3.2 Model optimization

As soon as some appropriate model parameters are found, an optimizer can be run. `PHOEBE` has a built-in optimizer called `Nelder-Mead` whose task is to find the best model fit to the observational data. This is done by χ^2 minimization. `Nelder-Mead`

allows the user to set initial values and then the optimizer fits some chosen parameters to the curve until the fit converges. In Fig. 27, it can be seen how the parameters converge with an increasing amount of iterations. The upper panel in Fig. 27 shows

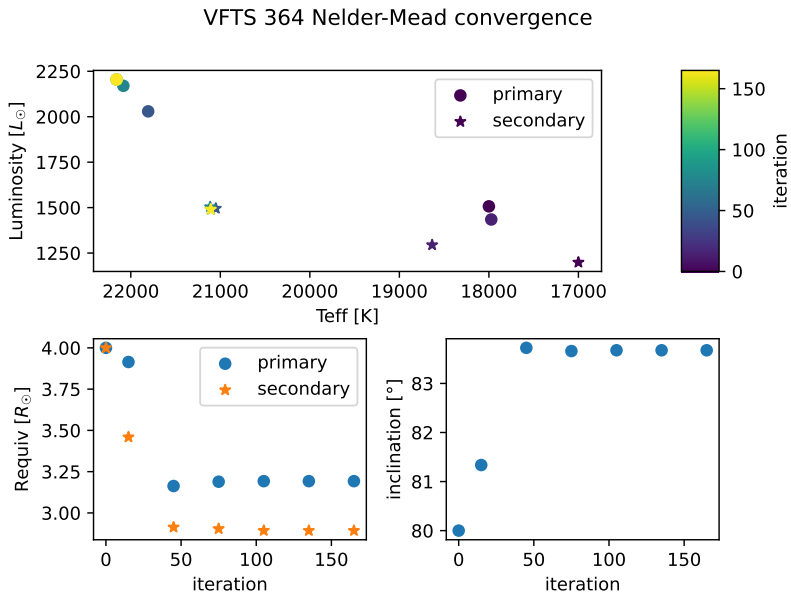

Figure 27: Convergence of Nelder-Mead

the HRD including both components of VFTS 364, colour-coded with the number of iterations. After 165 iterations, the results converged and the values for the effective temperature and the (calculated) luminosity did not change. The lower-left panel shows the radii of both objects and the bottom-right panel illustrates the convergence of the inclination of the system.
However, this optimization can also have its caveats due to degeneracies. This means that a specific set of parameters can result in a very similar model fit compared to some completely different parameters. When `Nelder-Mead` is run, it converges to one valley with the lowest χ^2 but it does not necessarily have to be the best physical parameters fitting to the system. Therefore, the parameters that result from `Nelder-Mead` have to be carefully interpreted.

2.4 Estimations of parameter uncertainties (EMCEE)

Once the `Nelder-Mead` optimization converges, the uncertainties of the parameters can be estimated via `EMCEE`. This tool allows the user to set distributions around the `Nelder-Mead` values to show the impact on the light curve. In this case, Gaussians around the centre values were set with appropriate variances. Depending on the number of optimized parameters, the required amount of iterations can change; the more parameters are optimized by `EMCEE`, the more iterations it needs to converge.

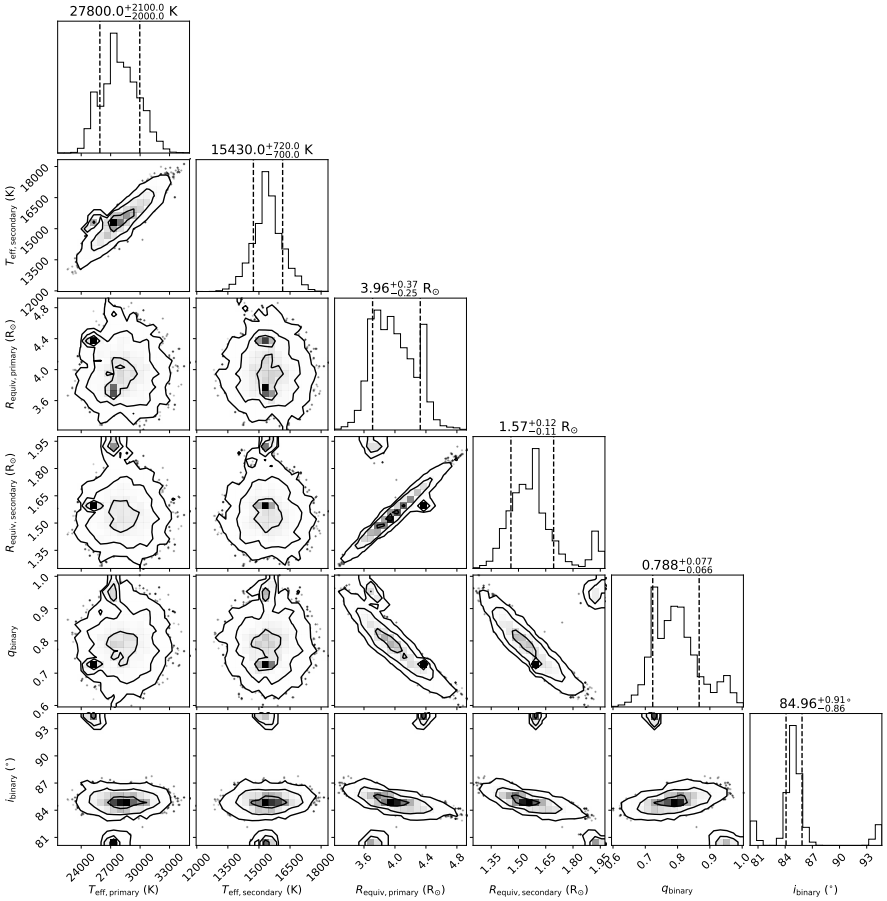

Figure 28: Example of an EMCEE corner plot of VFTS248, created with PHOEBE. This plot shows whether two quantities (shown at the bottom and on the left) are related to each other and a circular shape indicates no correlation. If the shape gets stretched towards a line, the correlation increases. An anti-correlation can be seen, for example, for the primary radius vs the mass ratio (3rd plot in the second to last row) while a correlation is depicted between the primary radius and the secondary radius (third plot in the third row from bottom).

That an EMCEE run has converged, is evident when there are clearly visible structures in the corner plot (Fig. 28). Correlated quantities have a squished shape from the bottom left to the upper right and anti-correlated quantities are visible when the plot has a shape from the top left to the bottom right. If there is a circular appearance, the quantities are not correlated with each other.
The topmost plots show the distributions of the parameters on their own, giving an idea of the uncertainties. The EMCEE sampling for VFTS 248 has converged because all the fitted quantities show Gaussian distributions around a maximum value and the correlation plots look smooth. If the number of iterations is insufficient, there

could be several maxima appearing in the probability plots.

3 Results

The analysis was primarily carried out to 14 systems, of which 9 showed clear eclipsing signs and the other 3 were potential ellipsoidal variables and one heartbeat variable. The values for the temperatures and the radii were taken from the `EMCEE` runs as shown for the example VFTS 248 in Fig. 28. The uncertainties of the luminosity (eq. 1) were calculated using the formula for Gaussian error propagation

$$\sigma_L = \sqrt{\left(\frac{\partial L}{\partial T} \cdot \sigma_T\right)^2 + \left(\frac{\partial L}{\partial R} \cdot \sigma_R\right)^2}, \tag{12}$$

where σ_L, σ_T and σ_R denote the uncertainty in Luminosity, effective temperature and radius respectively.

3.1 Stellar parameters of the system's components

This chapter summarizes the results from the Nelder-Mead analysis and the EMCEE sampling, giving uncertainties of the temperatures and radii of the components of the systems.

Table 2 summarizes the best values obtained from the posterior solution after the EMCEE runs in PHOEBE:

VFTS	t1	t2	r1	r2	m1	q	m2	i	e	logg1	logg2
112	26792	25033	5.524	4.690	18.794	0.658	12.373	83.181	0.000	4.228	4.188
157	30609	21082	2.916	2.758	8.089	0.333	2.690	86.140	0.029	4.416	3.987
189	28877	19538	4.998	2.313	14.246	0.227	3.234	79.837	0.002	4.194	4.220
206	16552	23499	9.333	3.116	3.839	1.083	4.158	59.394	0.034	3.082	4.070
215	20034	15937	5.131	2.304	8.846	0.336	2.971	79.047	0.284	3.964	4.186
240	24501	20564	3.731	3.573	8.056	0.970	7.814	76.163	0.001	4.201	4.225
248	27839	15428	3.962	1.569	9.806	0.788	7.730	84.962	0.138	4.234	4.935
255	23837	22432	5.534	5.369	10.600	0.970	10.282	72.074	0.024	3.977	3.990
27 cb	19430	18967	20.236	19.405	18.268	0.906	16.544	26.237	0.000	3.088	3.081
27	18311	17771	6.339	5.141	1.511	1.101	1.664	62.956	0.000	3.013	3.237
27 sd	18152	13765	6.297	17.059	24.129	0.627	15.137	31.571	0.000	4.222	3.154
364	22193	21404	3.132	2.801	5.787	0.970	5.613	83.868	0.157	4.209	4.293
388	19385	23636	10.503	7.138	12.725	0.456	5.802	21.718	0.656	3.500	3.494
430	17218	16817	8.103	5.541	14.445	1.141	16.485	56.572	0.000	3.781	4.168
687	21962	22161	18.711	6.755	8.676	0.315	2.736	52.194	0.000	2.832	3.216
883	19930	19450	3.409	3.437	15.038	0.970	14.587	77.687	0.000	4.550	4.530

Table 2: Stellar and orbital parameters (best values) from the EMCEE runs. For VFTS 27, the contact configuration (cb) and the semi-detached configurations (sd) were also tested. t1 and t2 are the primary and secondary temperatures respectively, r1 and r2 are their radii, m1 and m2 their masses, linked by the mass ratio q. And the surface gravities are in logg1 and logg2. The orbital inclination is shown in i and the eccentricity in column e. The uncertainties of the sampled parameters are given at the object's description.

The fitted models for all systems can be found in the appendix in section A. The

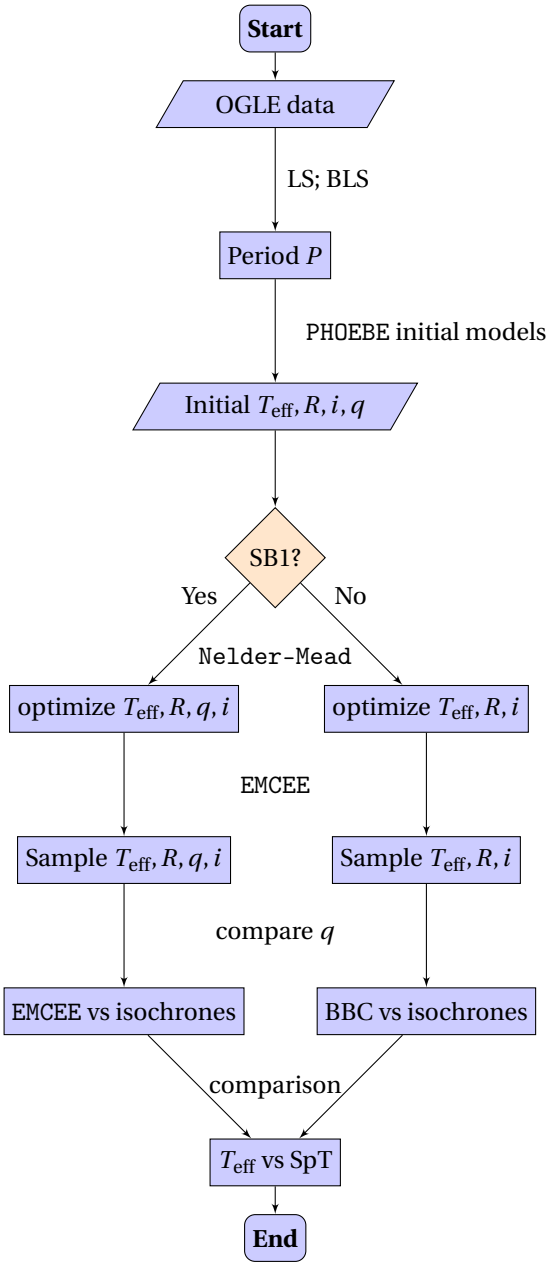

Figure 29: Flow chart to illustrate the processes of how the results were obtained. Note that for the SB2 systems VFTS 112, VFTS 206 and VFTS 248, the mass ratio was sampled and optimized too.

masses that PHOEBE calculated are origination from equations (13) and (14).

$$m_{\mathrm{p}} = \frac{39.478 \cdot a^3}{P^2 \cdot (q+1)} \cdot 2942.206 \tag{13}$$

$$m_{\mathrm{s}} = \frac{39.478 \cdot a^3}{P^2 \cdot \left(\frac{1}{q}+1\right)} \cdot 2942.206 \tag{14}$$

where q is the mass ratio, P the orbital period and a the semi-major axis. The semi-major axis itself depends on the inclination i

$$a = \frac{a \cdot \sin(i)}{\sin(i)} \cdot \left(\frac{1}{q}+1\right) \tag{15}$$

with keeping the value of $a\sin(i)$ fixed and vary the inclination. Setting $a\sin(i) = a_i$ to show that this value is kept constant yields the following equation:

$$a = \frac{a_i}{\sin(i)} \cdot \left(\frac{1}{q}+1\right) \tag{16}$$

Inserting eq. (16) in (13) and in (14) gives

$$\tag{17}$$

$$m_{\mathrm{p}} = \frac{39.478 \cdot \frac{a_i^3}{\sin^3(i)} \cdot \left(\frac{1}{q}+1\right)^3}{P^2 \cdot (q+1)} \cdot 2942.206 \tag{18}$$

$$m_{\mathrm{s}} = \frac{39.478 \cdot \frac{a_i^3}{\sin^3(i)} \cdot \left(\frac{1}{q}+1\right)^2}{P^2} \cdot 2942.206 \tag{19}$$

a_i is given in solar radii, the period in days and the resulting mass is in solar masses.

VFTS 27: This system was initially flagged as a potential contact system due to the ellipsoidal shape of its light curve. It is a close binary for a giant (B1 III-II) because of its short orbital period of around 6.58 days. When doing the analysis with `PHOEBE`, an overflow of the primary component frequently happened, resulting in the contact configuration and the semi-detached configurations to be tested. However, the best fit (see Fig. 30 for the comparison between the observational data and the computed models) was found using the detached configuration because this allowed the best to capture a slight eclipsing pattern. It also came out that both components have similar temperatures in the range of 18000-20000 K with the only exception being the secondary at the semi-detached configuration with about 14000 K. Furthermore, the mass ratio turned out to be close to 1, indicating that this system is likely a contact

config	$T_{\mathrm{eff,p}}$ [K]	$T_{\mathrm{eff,s}}$ [K]	R_{p} [$R_\odot$]	R_{s} [$R_\odot$]	i [°]	M_{p} [$M_\odot$]	M_{s} [$M_\odot$]
CB	19400^{+3000}_{-2800}	19000^{+2800}_{-2700}	$20.237^{+0.086}_{-0.105}$	19.426	26.237 ± 0.02	18.268	16.544
SD	18000^{+1800}_{-1900}	13800 ± 1700	$6.3^{+1.4}_{-1.2}$	13.436	31.7 ± 1.1	24.129	15.137
D	18400^{+2000}_{-1900}	17800 ± 1900	$6.33^{+0.24}_{-0.48}$	$5.13^{+0.39}_{-0.33}$	$62.97^{+0.9}_{-1.01}$	1.511	1.664

Table 3: VFTS 27 comparison among different configurations (CB=contact binary, SD=semi-detached, D=detached). The secondary was set to be the component in the semi-detached run. The masses are computed based on the inclination, mass ratio and orbital period and therefore fixed. See equations (13) and (14) for the calculation by PHOEBE.

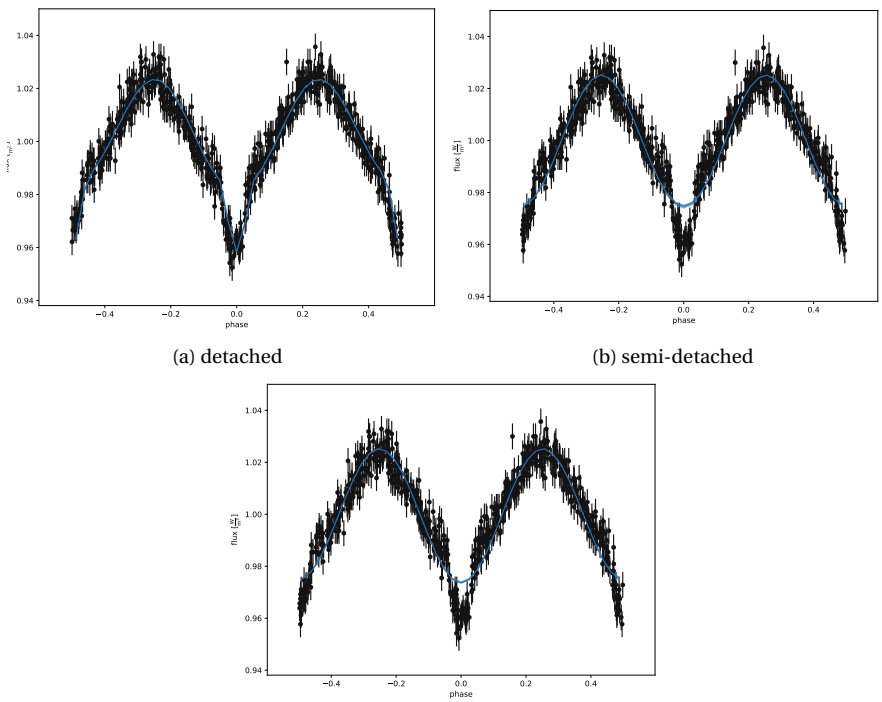

(a) detached

(b) semi-detached

(c) contact binary

Figure 30: comparison of the detached, semi-detached and contact binary model solutions with the model in blue and the observational data in black for VFTS 27.

system with the masses of both components equalizing each other. A more detailed overview of the parameters computed by PHOEBE with the different configurations can be seen in Table 3. When it comes to the comparison of the fitted model to the observational light curve (see panels in Fig. 30), the detached configuration best matches the light curve since it can best reproduce the minimum at phase 0. However, the parameters from PHOEBE in this case are inconsistent with the expectations, especially the masses with 1.555 and 1.628 solar masses are much too low for early B stars.
The masses for the semi-detached and contact configurations are more reasonable for early B stars even though the masses of the contact system are at the highest end of what is typical for B stars where they transition to O-type stars. This is the SB1 system where the mass ratio gets the closest to 1, which could mean that both components have similar masses but very different luminosities, resulting in only the primary being spectrally resolvable. The inclination has a strong impact on the masses of the components since it gets computed by PHOEBE with the equations (13) and (14)

VFTS 112: This is an SB2 eclipsing binary system with a comparable short period of about 1.67 days. The components of the system have similar effective temperatures, namely $T_{\mathrm{eff,p}} = 26800 \pm 1600$ K for the primary and $T_{\mathrm{eff,s}} = 25000^{+1500}_{-1400}$ K for the secondary. The radii of the components have a slightly bigger difference. The primary's one is $R\mathrm{p} = 5.52^{+0.32}_{-0.29} R_\odot$ and the secondary has a radius of $R_\mathrm{s} = 4.69^{+0.17}_{-0.2} R_\odot$. Its mass ratio with $q = 0.658$ is comparably small for an SB2 system.

VFTS 157: This is an SB1 eclipsing binary with an orbital period of 12.94 days, which is the longest of all eclipsing binaries in this sample. The components are located far from each other in the HRD; the primary has a temperature of $T_{\mathrm{eff,p}} = 30600^{+2600}_{-2300}$ K and a radius of $R_p = 2.92^{+0.9}_{-0.91} R_\odot$, whereas the secondary's effective temperature is only $T_{\mathrm{eff,s}} = 21100^{2000}_{-1600}$ K. This makes the secondary less luminous, also its radius of $R_\mathrm{s} = 2.76^{+0.9}_{-0.91} R_\odot$, contributes to it. The masses are quite different with $8.089 M_\odot$ and $2.69 M_\odot$ for the secondary respectively, resulting in a mass ratio of $q = 0.333$.

VFTS 189: This is another SB1 eclipsing binary with an orbital period of about 1.43 days. The analysis with `EMCEE` yielded an effective temperature for the primary of $T_{\mathrm{eff,p}} = 28900 \pm 2300$ K which is a reasonable temperature for a B0.7: V star. Its radius at $R_\mathrm{p} = 4.998^{+0.045}_{-0.047} R_\odot$ is fairly usual for B stars. The secondary was much cooler and smaller than the primary, showing that VFTS 189's components have a well-defined hierarchy. The temperature and the radius for the secondary are $T_{\mathrm{eff,s}} = 19500^{+1300}_{-1400}$ K and $2.3134^{+0.025}_{-0.024} R_\odot$ respectively. The masses computed by PHOBE are $14.202 M_\odot$ and $3.228 M\odot$ for the primary and secondary respectively, resulting in a mass ratio of $q = 0.227$, the smallest among all systems.

VFTS 206: This is a double-periodic SB2 binary system with a short period of about 7.55 days and a long period of the order of 215 days. For the modelling, the short

period from OGLE was used, yielding temperatures of 16550^{+870}_{-980} K and 23500± 1100 K for the primary and secondary respectively. This is one of the few systems where the secondary is hotter than the primary, But the primary still has the higher luminosity due to its three times bigger radius of $9.33^{+0.41}_{-0.57} R_\odot$ compared to the secondary with $3.12^{-0.43}_{+0.52} R_\odot$. It is also one of the few systems having a mass ratio bigger than unity with $q = 1.083$ (PHOEBE) and the primary's mass being 3.839⊙. With VFTS 430, it is the only system to have this property.

VFTS 215: Being an SB1 eclipsing binary at a period of around 4.4 days, it also showed a significant difference in the parameters of the components. The temperatures computed are $T_{\rm eff,p} = 20000 \pm 1600$ K for the primary and 15900^{+1200}_{-1100} K for the secondary, making both stars comparably cool in the studied sample. The radii of the components are $R_{\rm p} = 5.13^{\pm}0.43 R_\odot$ and $R_{\rm s} = 2.3^{+0.24}_{-0.23} R_\odot$ for the primary and secondary respectively. This difference also showed up in the masses with 8.85 and 2.97 solar masses for primary and secondary respectively, leading to a low mass ratio, which is expected for SB1 systems.

VFTS 240: With an orbital period of only 1.37 days, VFTS 240, an SB2 system, is the system with the shortest period of all eclipsing binaries analysed in this work. The temperatures of the components in this SB2 system are in good agreement for early B stars here, namely $T_{\rm eff,p} = 24500 \pm 2200$ K for the primary and $T_{\rm eff,s} = 20600^{+1700}_{-1800}$ K for the secondary. The same applies for the radii whose values are $R_{\rm p} = 3.73^{+0.11}_{-0.17} R_\odot$ for the primary and the secondary's radius is $R_{\rm s} = 3.57^{+0.19}_{-0.18} R_\odot$. The mass ratio was fixed to 0.97 and the masses at around 8 solar masses.

VFTS 248: This SB2 eclipsing binary system shows an orbital period of about 2.49 days and the depth of both eclipses is different which can also be seen in the obtained stellar parameters, especially in the temperatures. The temperatures of the components were computed to be $T_{\rm eff,p} = 27800^{+2100}_{-200}$ K for the primary stars being much hotter than the secondary star at only $T_{\rm eff,s} = 15430^{+720}_{-700}$ K. Also the radii of both objects are quite different with the primary being more than double the size of the secondary, the values being $R_{\rm p} = 3.96^{+0.37}_{-0.25} R_\odot$ and $R_{\rm s} = 1.57^{+0.12}_{-0.11} R_\odot$.

VFTS 255: This SB2 eclipsing binary system has an orbital period of about 2.84 days and both components are quite similar in their stellar properties. The temperatures are $T_{\rm eff,p} = 23800^{+2100}_{-2200}$ K for the primary and $T_{\rm eff,s} = 22400 \pm 2000$ K for the secondary. The radii of the components confirm their similarity since they are $R_{\rm p} = 5.53^{+0.19}_{-0.25} R_\odot$ and $R_{\rm s} = 5.37 \pm 0.024 R_\odot$ for the primary and secondary respectively.

VFTS 364: Another SB2 system of eclipsing binaries where both components take about 4.4 days to orbit each other once. Both eclipses show a different depth, meaning that differences in the parameters should be expected. However, they are not as big as compared to VFTS 248 and more similar to VFTS 255. The temperatures are $T_{\rm eff,p} = 22200 \pm 1500$ K and $T_{\rm eff,s} = 21400 \pm 1400$ K for the primary and secondary respectively, The radius of the primary was computed to

$R_p = 3.13^{+0.23}_{-0.18} R_\odot$ and the secondary is a bit smaller at $R_s = 2.8^{+0.21}_{-0.29} R_\odot$. The masses are 5.787 and 5.613 solar masses for the primary and secondary respectively.

VFTS 388: This SB1* heartbeat system has the following parameters of the stars: $19400^{\pm}1900$ K for the primary and 23600^{+2300}_{-2500} K for the secondary. Despite being hotter, the secondary is smaller with $7.138^{\pm}0.048 R_\odot$ compared to the primary whose radius is $10.503^{+0.048}_{-0.051} R_\odot$. It has by far the highest eccentricity of all systems studied here with $e = 0.656$.

VFTS 430: This is an SB1 system showing ellipsoidal variations but no eclipses. The period discussion yielded a 2.59-day period for the analysis in contrast to the 8.76-day period given by the BBC. The short period was adopted here because it still showed the periodic variability similar to the long period but not phase-folded multiple times (see more details in Figure 21), following the same argumentation as for VFTS 883 (see Fig. 24). Because there are no eclipses, the determination of the stellar parameters gets more difficult here. EMCEE finalized here with the following temperatures: $T_{\rm eff,p} = 17200^{+2200}_{-2300}$ K for the primary and $T_{\rm eff,s} = 16800 \pm 2200$ K for the secondary. To produce ellipsoidal variability, the stellar surfaces have to come sufficiently close, explaining their relatively big radii of $R_p = 8.1^{+0.35}_{-0.41} R_\odot$ for the primary and $R_s = 5.54^{+0.55}_{-0.41} R_\odot$ for the secondary. It is also a system whose mass ratio was computed to be bigger than unity, meaning that the primary is less massive than the secondary. This is also true for VFTS 206.

VFTS 687: The periods for Lomb-Scargle and the BBC period sufficiently agree at around 2.4 days but differ too much from the BLS period of 1.18 days, which is why the LS period was taken for the analysis. This system is, like VFTS 430, an SB1 system showing ellipsoidal variability, however with a lower amplitude. EMCEE concluded its run with the following stellar parameters: $T_{\rm eff,p} = 22200^{+2100}_{-2300}$ K for the primary and $T_{\rm eff,s} = 22200^{+2300}_{-2400}$ K, meaning that the primary is at the same temperature as the secondary. The primary's radius was computed to $18.711^{+0.089}_{-0.097} R_\odot$ and the secondary's to $R_s = 6.72^{+0.13}_{-0.11} R_\odot$. Since the primary is more than three times bigger than the primary, it shows a higher luminosity. However, due to a mass ratio of $q = 0.315^{+0.015}_{-0.012}$, the secondary likely has less mass than the primary.

VFTS 883: This SB2 eclipsing system has a controversial discussion of the correct orbital period. The shortest period still showing two distinct eclipses is 2.33 days, which was adopted in the analysis. The parameters of both stars are very similar. The temperatures are $T_{\rm eff,p} = 19900^{+2200}_{-2000}$ K and $T_{\rm eff,s} = 19400 \pm 2000$ K for the secondary respectively. The same worked out to be for both radii which are $R_p = 3.41^{+0.33}_{-0.49} R_\odot$ for the primary and $R_s = 3.44^{+0.31}_{-0.49} R_\odot$ for the secondary. This shows that both components are very similar to each other, which is also true for the masses of 15.038 and 14.587 solar masses respectively.

I also compared the orbital inclinations with respect to the orbital periods of the eclipsing systems. It is expected that the inclination should approach 90 degrees

as the orbital period increases. A longer period usually means that the separation between the components also increases. To make them still eclipsing, the orbital inclination has to approach an edge-on view, which is defined with an orbital inclination of 90 degrees. Fig. 31a shows the results of that analysis. In general, all

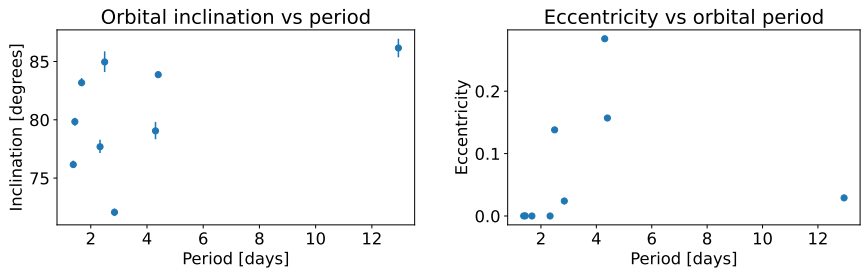

(a) Orbital inclinations in comparison with the orbital period of the eclipsing systems.

(b) Orbital eccentricities with respect to the orbital periods of the eclipsing systems.

Figure 31: Dependencies of the orbital inclination (left) and the orbital eccentricity (right) as a function of the orbital period.

the inclinations tend to be relatively high with none going below 70 degrees. Typical values for the inclinations are in the range of 75 to 85 degrees with orbital periods between 1.37 and 4.4 days.

It can be seen in Fig. 31a that the eclipsing system with the longest period (VFTS 157, ≈ 12.9 days) also has the highest inclination ($86.16^{+0.79}_{-0.8}$ degrees). This is a logical finding because eclipses can only be seen if the orbital plane is close to be in the line of sight to make the stars pass in front of each other to cause them to eclipse each other.

When looking at the eccentricity as a function of the orbital period for the eclipsing binaries (see Fig. 31b), it becomes clear that the systems with periods under two days have a circular orbit. The system with the shortest period to show a significant eccentricity ($e > 0.01$) is VFTS 248 with an orbital period of 2.494 days and an eccentricity of $e = 0.138$. This matches well with the results in Lennon et al. (2024).

3.2 Plotting on HRD with isochrones

With the stellar parameters that were obtained and listed in section 3.1, it is possible to put them on a Hertzsprung-Russell diagram (HRD) to compare the temperatures and luminosities of the stars with isochrones.

An isochrone is a line of effective temperatures and luminosities that are connected by stars of the same *age*. Stars are born with different initial masses and the mass heavily affects the future evolution pathways. For example, very young isochrones of a few Myr are connecting stars within the main sequence since they have not yet evolved from it. But older isochrones include that the more massive stars have evolved to giant stars and that they drifted away from the main sequence.

As already mentioned, this procedure is meant to find out whether the systems have

undergone a phase of mass transfer or not by plotting the components on an HRD with isochrones. When a binary system is formed, both stars are born at the same time but they may have different masses. This means that both components are located at different points in the HRD but on the same isochrone. Then two scenarios are possible. On the one hand, the components have not interacted with each other and no mass transfer has been occurring since their birth. The masses did not change significantly so both components should still be positioned on one common isochrone in the HRD. The following paragraph will discuss the findings from the isochrone fitting for each analysed star.
All points of the isochrones are associated with a stellar mass value. To compute the masses and mass ratios based on the isochrones, the point closest to an appropriate isochrone is searched by minimizing the expression in equation (20).

$$d = \sqrt{(T_{\text{eff,star}} - T_{\text{eff, isochr}})^2 + (L_{\text{star}} - L_{\text{isochr}})^2} \tag{20}$$

This is done for all values of the isochrones in both linear and logarithmic scaling. For the linear scaling, the values were kept as in eq. (20). For the logarithmic distances, the $\log_{10}$ of all temperature and luminosity values is taken first before inserting them into eq. (20). When the temperature-luminosity pair closest to the star is found, its corresponding mass value is assigned to the star.
Two different sets of isochrones were used in the analysis to allow comparison among them. Firstly, PARSEC isochrones were obtained by a query on the webpage http://stev.oapd.inaf.it/cgi-bin/cmd with the following settings:

```
[M/H]=-0.5
YBC +new Vega
PARSEC version 1.2S
60% Si, 40% AlOx
Periods from Trabucchi+2021
Kroupa2001,2002 IMF
Ages from 5e5 to 1e8 yr with step 5e5 yr
```

The models were done by Bohlin, Hubeny, and Rauch 2020, Tang et al. 2014, Chen et al. 2014, Chen et al. 2015, Pastorelli et al. 2020, Trabucchi et al. 2021, Pavel Kroupa 2001, P. Kroupa 2002 and the LMC-metallicity was taken from Li et al. (2024). The evolutionary tracks for the PARSEC version 1.2S were computed by Chen et al. (2015). They assumed enhanced mass losses for the most massive stars when the luminosity of the star approached the Eddington luminosity. This luminosity limit is set by the inward-directed gravitational pull and the outward-directed pull by the photons. Another set of isochrones and additional evolutionary tracks is provided by Brott et al. (2011). The isochrones consider the metallicity of the LMC and the initial rotational velocity was set to 111 kms^{-1}, a typical value for massive binaries. The analysis was carried out for these systems with isochrone of the ages 1 to 35 Myr with a spacing of 1 Myr. They contain masses from 5 to more than 20 solar masses, covering the range of early B-type stars.
The masses obtained by PHOEBE matched better with the mass values of the Brott et al. (2011) isochrones so that they are illustrated in Fig. 32, 33 and 34. Especially in

the range of 10 $M_\odot$ and above, the PARSEC isochrones mostly yielded values in the range of 4 to 6 $M_\odot$, making them less reliable and therefore excluded in this analysis. The masses and mass ratios are obtained by measuring the smallest Euclidean

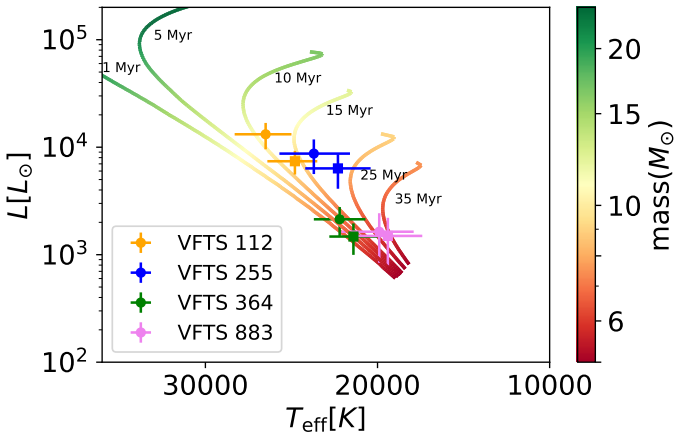

Figure 32: Brott et al. (2011) isochrones of 1,5,10,15,25 and 35 Myr. These systems in this plot can be associated with one common isochrone

distance (see eq. 20) between the centre values of the components and the mass associated with the position on the isochrone with either logarithmic or linear scaling of the temperatures and luminosities. The results can be seen in Table 4.

3.3 Systems having both components on the same isochrone

Four systems were found whose components lie on a common isochrone. This means that these systems are not mass-transfer candidates.
VFTS 364 is the best example to illustrate this, being located on the same isochrone (10 Myr from Brott et al. (2011)). This means that the masses of the objects remained unchanged since the stars had been formed and there was no phase of mass transfer in this system. The same isochrone is also the best fit for the components of VFTS 112, however, their components lie on points of higher masses. The components of VFTS 883 lie towards cooler temperatures, thus making the 30 Myr isochrone the best line fitting for both components that are the closest among the systems in terms of temperature and luminosity in Fig. 32.
VFTS 255's components fit the best with the 20 Myr isochrone. Individually, the 17 Myr and the 22 Myr isochrone align the best for the primary and secondary respectively but due to their proximity, the assumption of a common isochrone still holds for this system.

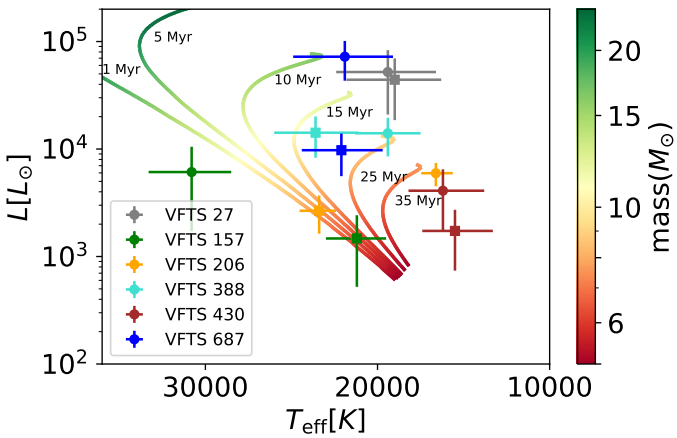

Figure 33: Brott et al. (2011) 1,5,10,15,25 and 35 Myr isochrones. The systems plotted here are possible (post-)mass transferring systems since they do not fit on one isochrone.

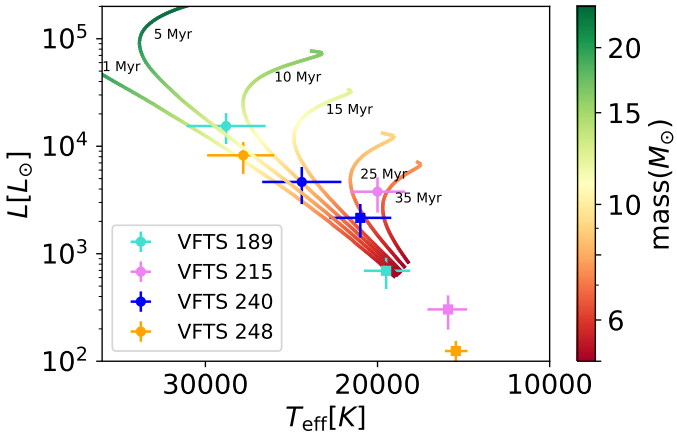

Figure 34: Brott et al. (2011) 1,5,10,15,25 and 35 Myr isochrones with systems where one isochrone could be found but it is uncertain.

VFTS	$m_{1,\mathrm{PHOEBE}}$	$M_{1,\mathrm{lin}}$	$M_{1,\mathrm{log}}$	$m_{2,\mathrm{PHOEBE}}$	$M_{2,\mathrm{lin}}$	$M_{2,\mathrm{log}}$	q_{PHOEBE}	q_{lin}	q_{log}
112	18.794	11.092	11.092	12.373	9.398	9.398	0.658	0.847	0.847
157	8.089	10.849	10.150	2.690	6.250	6.450	0.333	0.576	0.635
189	14.246	12.292	12.292	3.234	5.350	5.150	0.227	0.435	0.419
206	3.839	7.481	7.432	4.158	7.650	7.600	1.083	1.023	1.023
215	8.846	6.94	6.492	2.971	<5	<5	0.336	<0.72	<0.72
240	8.056	8.549	8.499	7.814	6.548	6.648	0.970	0.766	0.782
248	9.806	10.748	10.698	7.730	<5	<5	0.788	<0.465	<0.467
255	10.600	9.346	9.364	10.282	8.345	8.345	0.970	0.893	0.893
27 cb	18.268	11.901	11.901	16.544	11.901	11.901	0.906	1	1
364	5.787	6.943	7.049	5.613	6.449	6.349	0.970	0.928	0.901
388	12.725	9.423	9.423	5.802	10.291	10.291	0.456	1.092	1.092
430	14.445	7.334	6.990	16.485	4.998	5.897	1.141	0.682	0.844
687	8.676	15.388	15.388	2.736	9.093	9.093	0.315	0.591	0.591
883	15.038	5.997	5.897	14.587	5.747	5.797	0.970	0.967	0.975

Table 4: Masses and corresponding mass ratios obtained by PHOEBE vs isochrone fitting using either linear or logarithmic scales for the distances to the isochrone from Brott et al. (2011). All the masses are given in solar masses. For the systems VFTS 215 and VFTS 248, the secondary lies below the 5 solar masses lower limit for the modelling of the isochrones so that the secondary masses and the mass ratios can only be estimated with higher limits. For VFTS 430, older isochrones would have to be used since their components are located to colder temperatures than the 35 Myr isochrone from Brott et al. (2011). This can be seen in Fig. 32

3.4 Systems with no common isochrone (mass-transferring candidates)

In total, three systems were found that do not fit on a common isochrone, meaning that they are candidates for mass transferring systems. The best example of such a system is VFTS 157, even when considering the error bars. This means that VFTS 157 is the system of this sample that has undergone a phase of mass transfer with the highest probability.

Similar relations between the components can also be observed for the systems VFTS 206 and VFTS 687, though they do not show eclipses like VFTS 157. The components of VFTS 687 have the same temperatures but the primary is much bigger than the secondary, thus having a higher luminosity. In contrast, the components of VFTS 206 have a high ratio of about 3 concerning their radii. The primary therefore stays more luminous than the secondary despite its lower effective temperature.

Three more systems have relatively high uncertainties but their best values do not match a common isochrone, meaning that they are probably (post-) mass transferring systems as well. In the case of VFTS 27, the error bars are comparably high with temperature uncertainties of ≈ 2700 K, which is likely due to the contact configuration. In total, this system is a mass-transferring system due to the proximity of the components and the comparably high radius, making this system a contact binary.

For VFTS 430, the components lie to lower temperatures than the oldest isochrone of Brott et al. (2011) can map to. But because of the high uncertainties and the higher separation of the components as compared to VFTS 27, it is likely a mass-transferring system as well.

Finally, for VFTS 388, it can be seen that its components have comparable lumi-

nosities but vary in temperatures by about 4000 K. The 15 Myr isochrone fits for the primary while the 25 Myr isochrone is a better approximation for the secondary.

3.5 Systems where the relationship to the isochrones is uncertain

For four more systems, it is not entirely clear whether their components are located on the same isochrone or not. In these cases, the error bars of the stars intersect a few isochrones of the same age while the best values are inconsistent with them. An example to illustrate is the system VFTS 240, where the 10 Myr isochrone fits well with the primary and the 25 Myr isochrone with the secondary. However, due to the error bars of both components intersecting a range of isochrones from 10 to 25 Myr, no clear conclusion can be drawn. The high age uncertainty arises mainly from the temperature uncertainties (~ 2000 K) and the proximity of different isochrones at the main sequence (spectral type B1-2 V). Similarly is the situation with the components of VFTS 189. While the isochrone for 7 Myr intersects the primary the best, no conclusion can be made for the secondary because of its location in the main sequence, making isochrones of 1 to 20 Myr in the possible range.
The secondaries of VFTS 215 and VFTS 248 have too low temperatures and luminosities to assign an isochrone to them. They are likely located on the main sequence when interpolating the isochrones towards lower masses at the main sequence.

3.6 Comparison with evolutionary tracks

Brott et al. (2011) also provided evolutionary tracks for massive stars and I extracted a total of 7 tracks between 5 and 19 solar masses to compare them with the masses obtained by PHOEBE. An evolutionary track illustrates the temporal evolution of a star in the HRD at a given initial mass. These evolutionary tracks start at the main sequence and then they evolve away from it. The speed of this divergence heavily depends on the initial masses and goes faster the higher the initial mass is set. All extracted evolutionary tracks assume rotational velocities of the order 110 kms^{-1}. The evolutionary tracks among the system's components are shown in Fig. 35, 36 and 37. Table 5 compares the masses obtained by PHOEBE with the interpolated masses from the evolutionary tracks. It can be seen that from the values in Table 5 that there is sometimes an agreement from the masses obtained by PHOEBE compared with the evolutionary masses obtained by interpolation with the evolutionary tracks from Brott et al. (2011).

4 Discussion

The main goal of this work is to find out if a system underwent a phase of mass transfer or not. Since the assumption holds that both stars are coeval, both stars have been born at the same time and should sit on the same isochrone when plotted. But if this is not the case, this means that the masses of the stars have changed after the formation process and this can completely alter the evolution of a star, especially its main sequence lifetime.

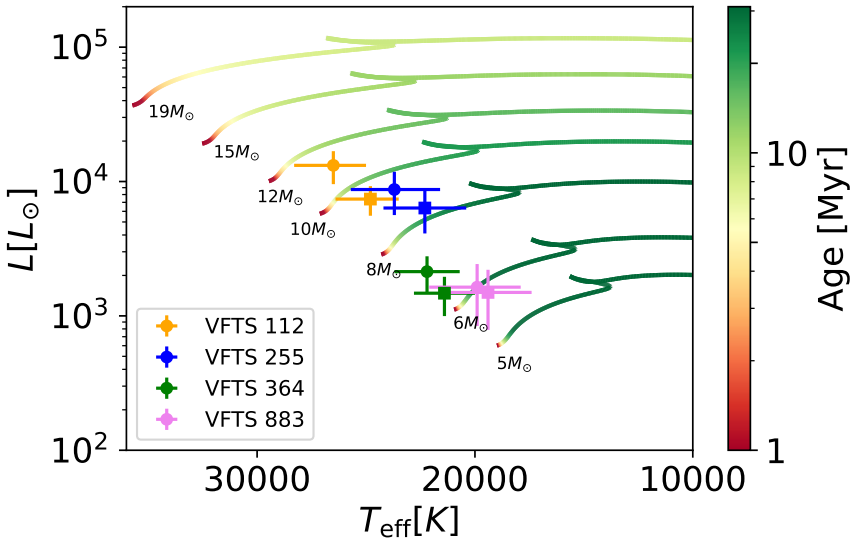

Figure 35: Plotting the systems with evolutionary tracks of different initial masses from Brott et al. (2011). The systems here were found to have a common isochrone.

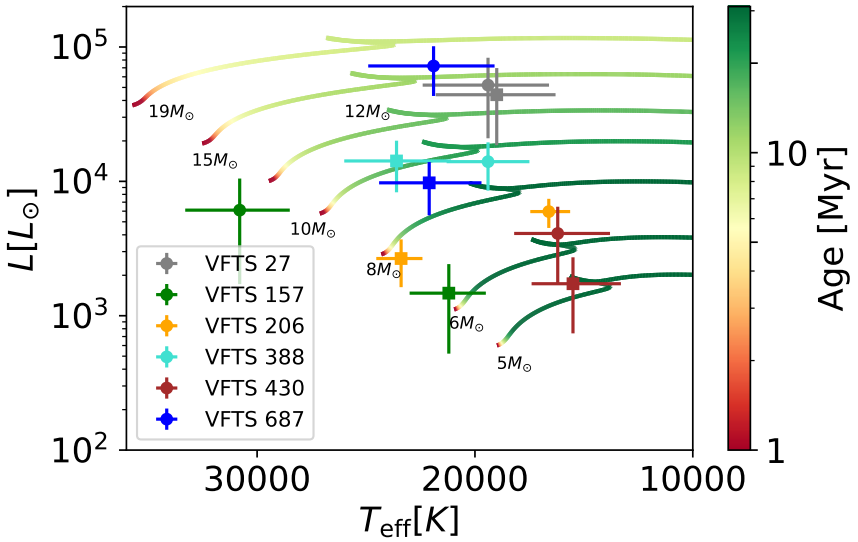

Figure 36: Same as Fig. 35, but for the mass-transferring candidates.

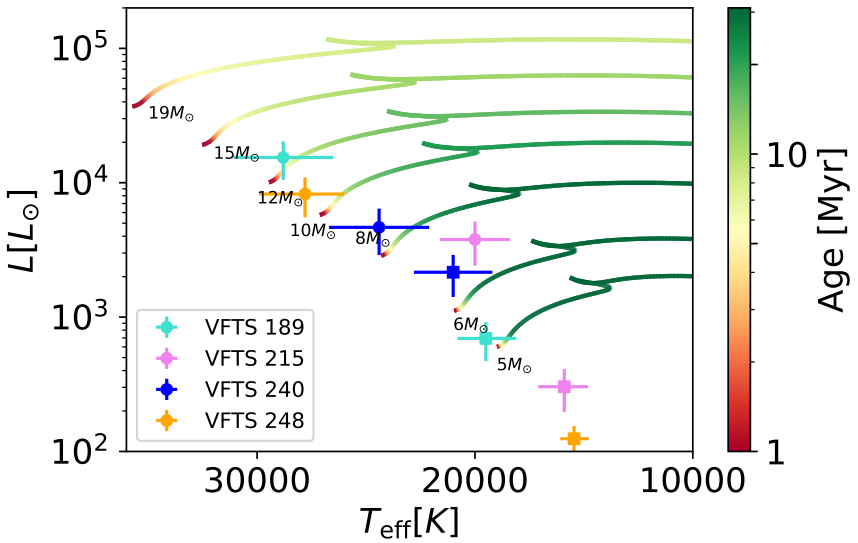

Figure 37: Same as Fig. 35, but for the systems where the relationship to an isochrone is uncertain.

VFTS	$m_{1,\rm PHOEBE}$	$M_{1,\rm evol}$	$m_{2,\rm PHOEBE}$	$M_{2,\rm evol}$
112	18.794	11	12.373	9.5
157	8.089	12	2.690	6
189	14.246	12	3.234	5.5
206	3.839	7	4.158	7.5
215	8.846	7	2.971	~ 4
240	8.056	9	7.814	6.5
248	9.806	11	7.730	~ 3
255	10.600	9.5	10.282	8.3
27 cb	18.268	14	16.544	13
364	5.787	7	5.613	6.5
388	12.725	9	5.802	10
430	14.445	6	16.485	5
687	8.676	16	2.736	9
883	15.038	6	14.587	5.7

Table 5: Comparison of the masses obtained by PHOEBE with the approximate masses obtained by interpolation from the evolutionary tracks by Brott et al. (2011). The index 1 is for the primary and the secondary is indexed with a 2. All the masses are given in solar masses.

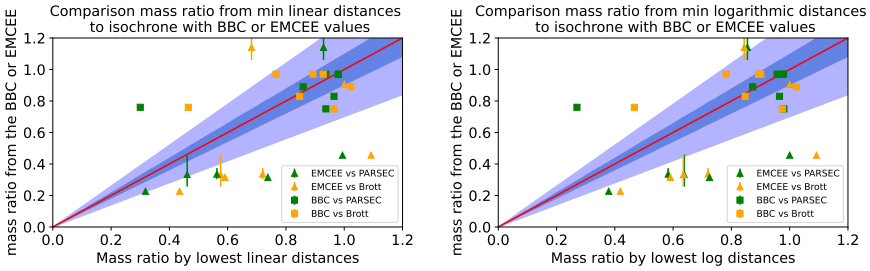

(a) Linear distances to isochrones

(b) Logarithmic distances to isochrones

Figure 38: Comparison of the mass ratios obtained by either linear (lin) or logarithmic (log) distance measurement to PARSEC and Brott et al. (2011) isochrones in comparison with either the BBC or the EMCEE values. The yellow markers represent comparisons with the Brott isochrones while the green markers represent findings based on the PARSEC isochrones. Triangles denote the SB1 systems where the isochrone mass ratios are compared with EMCEE results and the square markers compare the isochrone values with the BBC ones (SB2 systems, Villaseñor et al. 2021). The darker blue shaded region marks a deviation up to 10 % from the line of both values being equal to each other and the lighter blue region marks a tolerance of up to 30 %.

In section 3, the stellar parameters were determined and the relation to the best-fitting isochrones was stated. From this data, it can be seen that some systems are clearly on the same isochrone, while the state for others is not obvious and one system does not fit on one isochrone.

4.1 Comparison of parameters

4.1.1 Mass ratios

For both SB1 and SB2 systems, the point of minimum distance of the components in the HRD was computed. Because each point in an isochrone corresponds to a certain mass, a mass ratio can be obtained by comparing to the isochrones as well. For the SB1 systems, the mass ratio was provided by the `EMCEE` sampler from `PHOEBE`, providing a method to compare the values.
For the SB2 systems, however, the mass ratio was fixed to the value of the system in Villaseñor et al. (2021), except for VFTS 112, 206 and 248. The panels in Fig. 38 compare the mass ratios obtained by the isochrone fitting and the other aforementioned method, depending on whether the system is an SB1 or SB2. When comparing the values for the mass ratios for different systems, it can be seen that they are mostly in agreement within 10 per cent when the mass ratios are close to unity. These are the SB2 systems with mass mass ratios close to unity and the components are closely positioned in the HRD. There is one exception where the mass ratio of the SB2 system has a deviation of more than 30%. It is the system VFTS 248 whose BBC value is about twice to three times as big ($q = 0.76$) as the isochrone values (< 0.42) because of the comparably low temperature and luminosity of the secondary (see Fig. 34).

In contrast, a deviation of more than 30 % mainly arises when the mass ratios are smaller than 0.8. This comes for all SB1 systems with no BBC mass ratio available

Comparison with EMCEE sampling at the SB1 systems: Most of the SB1 systems show mass ratios that are significantly smaller than 1 which makes sense because then the primary is the dominating component in the system, making the secondary difficult to detect in the spectrum. VFTS 157, 189, and 215 all show low mass ratios, the lowest value for VFTS 189 likely has a mass ratio of around 0.3.
The `EMCEE` sampling even provided mass ratios greater than unity for VFTS 430. Its light curves show an ellipsoidal variation. This shows a high likelihood that both systems were undergoing a phase of mass transfer since the primary initially had more mass, meaning that the mass ratio was smaller than 1. However, when a phase of mass transfer happens, the donor star (primary) loses mass while the accretor (secondary) gains mass, thus flipping the mass ratio to a value greater than one, meaning that the secondary currently is more massive than the primary. However, the fitting with the isochrones does not verify the `EMCEE` results for both of these systems. That is likely because either VFTS 430 is older than 35 Myr, meaning it does not come close to the analysed isochrones or the parameters of this system have to be revised.

Comparing with the spectroscopic mass ratios at the SB2 systems For the SB2 systems where both components can be resolved, a more equal distribution of the mass in the components is expected. For the systems having a mass ratio close to unity, there is an agreement between the mass ratio from the isochrones and the mass ratio in Villaseñor et al. (2021), especially for VFTS 364 and closely agreeing with VFTS 112. At most of the other systems, the isochrone fitting overestimates the mass differences, becoming the most obvious at VFTS 248. During its primary eclipse the relative flux drops by about 0.2, while the flux reduction is only about 0.07 for the secondary eclipse. Due to the setting of the light curve model to be dataset-scaled in PHOEBE, this might have caused the parameter differences to be overestimated. One system, however, shows the opposite behaviour as the BBC mass ratio is further away from unity than the isochrone mass ratio for VFTS 883. This can be caused by the fact that both eclipses have the same depth in this system and different eccentricities were used (0.359 in the BBC vs 0 in my analysis), making both components to be the most similar in the studied sample.

4.1.2 Effective temperatures, radii and spectroscopic type

The temperatures were interpolated with a linear fit of the values given by Pecaut and Mamajek (2013) for early B-type stars up to a spectral type of O9. The temperatures of the primaries were also compared to the spectral types (see Fig. 39). Most of them are in agreement with the spectroscopic temperatures in Lennon et al. (2024) within the error bars. However, some outliers also appeared, especially those whose temperatures are too low as it would be expected for a B0.5 star. The most prominent example is the system VFTS 430 with a primary temperature of only 16200 ± 2400 K, making it about 10000 K or 4σ cooler than the expectation from the

VFTS	SpT	$T^{\mathrm{p}}_{\mathrm{eff,PHOEBE}}$ [K]	$T_{\mathrm{eff,L}}$ [K]	R_{p} [$R_\odot$]
27 (cb)	B1 III-II	19400^{+3000}_{-2800}	20500	$20.236^{+0.086}_{-0.104}$
112	EarlyBs	26800 ± 1600	29100	$5.52^{+0.33}_{-0.29}$
157	B2 V	30600^{+2600}_{-2300}	24500	$2.92^{+0.9}_{-0.91}$
189	B0.7: V	28900 ± 2300	27900	$4.998^{+0.045}_{-0.047}$
206	B3 III:	16550.0^{+870}_{-980}	19200	$9.33^{+0.41}_{-0.57}$
215	B1.5 V	20000 ± 1600	25700	5.13 ± 0.43
240	B1-2 V	24400 ± 2300	26800	$3.73^{+0.11}_{-0.17}$
248	B2: V	27800^{+2100}_{-2000}	25700	$3.96^{+0.37}_{-0.25}$
255	B2: V	23800^{+2100}_{-2200}	24500	$5.53^{+0.25}_{-0.19}$
364	B2.5: V	22200 ± 1500	23400	$3.13^{+0.23}_{-0.18}$
388	B0.5 V	19400 ± 1900	27500	$10.503^{0.048}_{-0.051}$
430	B0.5 Ia+((n))Nwk	17200^{+2200}_{-2300}	24500	$8.1^{+0.35}_{-0.41}$
687	B1.5 Ib((n))Nwk	22000^{+2100}_{-2300}	20000	$18.711^{+0.089}_{-0.097}$
883	B0.5 V	19900^{+2200}_{-2000}	29100	$3.41^{+0.33}_{-0.49}$

Table 6: Comparison of effective temperatures and radii from the primaries obtained by PHOEBE with the spectral classification in Villaseñor et al. (2021) and the spectroscopic effective temperatures in Lennon et al. (2024)

spectral type. But also VFTS 883 and VFTS 388 are unexpectedly cool stars for their spectral type B0.5 with primary temperatures of 19900^{+2200}_{-2000} K and 19400 ± 1900 K for their primaries respectively. A low estimation of the temperatures can arise from high reddening, reducing the fluxes of shorter wavelengths. The systems VFTS 430 and 388 are located close to the centre of NGC 2070, the nebula in 30 Doradus, so that they are invisible in the optical DSS image when doing a SIMBAD[2] query. In the 2MASS image (near-infrared), NGC 2070 becomes more transparent, meaning that the extinction is reduced. This deviation doe

Another possible reason for the deviation of the photometric temperatures compared to the spectroscopic ones is that Lennon et al. (2024) used the spectral type as a base to fit the spectral effective temperature. If the spectral type has an uncertainty of 0.2 subtypes, this can make a difference of 10000 K at this regime (e.g., B0 vs B2, see Fig. 39).

Contrary to the previously discussed systems, VFTS 157 has a deviation in the other direction. Its primary is hotter than it would be expected for its spectral type. Since it has been marked as a mass-transferring candidate, this can be explained by a contracting post-mass transfer star. When stars contract, the pressure in their cores increases, causing the temperature to rise as well according to thermodynamics. The spectral type might also be inaccurate, causing an underestimation of spectroscopic temperature for VFTS 157.

Therefore, these systems should be studied more carefully with both spectroscopy and photometry to identify the cause of the deviations and to match the data to find a mutual agreement in future studies. According to Fig. 39, one expects effective

[2] https://simbad.cds.unistra.fr/simbad/sim-fid

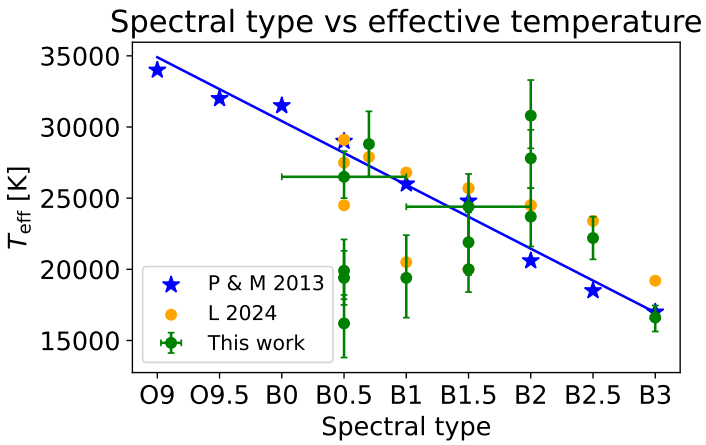

Figure 39: Effective temperature as a function of the spectral type. The values for the intrinsic temperatures with respect to the spectral type (blue stars and linear fit) are from Pecaut and Mamajek (2013). The effective temperatures were spectroscopically estimated with He II and Si III and IV lines by Lennon et al. (2024) (yellow points). And the spectral classes for this work were taken from Evans et al. (2015) and the uncertainties come from the `EMCEE` sampling (green points). The temperatures were all taken from the primaries.

temperatures of about 28000 K for B0.5 stars and about 17000 K for a B3 star with an approximately linear dependency. The majority of the systems are in the same range as in the work of Lennon et al. (2024) but some are deviating more significantly, especially systems that are too cool compared to the expectations of a B0.5 star.

4.2 Interesting finding

This section discusses in more detail about the interpretations of the results obtained by PHOEBE and the fittings with isochrones and the evolutionary tracks. The focus is on the potential (post-)mass-transferring systems as well as findings related to the parameters such as the masses.

4.2.1 Mass transfer candidates

It was found that the components of three systems did not fit on one isochrone (VFTS 157, VFTS 206 and VFTS 687), even when considering the error bars of the temperatures and luminosities.
The system VFTS 157 is the only eclipsing one of them, the others show other light curves that rather have an ellipsoidal shape. The primary of VFTS 157 has a relatively small radius compared to its effective temperature, which can be concluded by its location below the main sequence that is marked by the starting points of the evolutionary tracks in Fig. 36 based on an age of 1 Myr. A small radius compared

to its temperature can be explained by a stripped post-mass transfer star (Klement et al. 2025).
The systems VFTS 206 and VFTS 687 do not have eclipses in their light curve but show instead sinusoidal variations. What is notable is that the components' temperatures for VFTS 687 are quite similar with both being around 20000 K. The components of VFTS 206, however, have quite different temperatures, the primary being around 16500 K and the secondary being hotter at approximately 23500 K. A different relative location of the components can give insight into how fast and how long the mass transfer happened. To determine its nature, follow-up studies for these systems are needed to refine the parameters and evolutionary models that can model mass-transferring phases.
Three more systems are mass-transferring candidates, VFTS 27, VFTS 388 and VFTS 430. For VFTS 27, this is plausible since both components are so close together that they form a contact binary, meaning an RLOF of both components occurs and mass can therefore be easily transferred.
VFTS 388, the heartbeat system, is another candidate. It is the system that has the highest eccentricity by far in the sample with $e = 0.656$. When the stars are at periastron, they approach each other so that mass transfer can be possible during the periastron passages. This could explain the nature of both components not fitting on a common isochrone.
With the isochrones from Brott et al. (2011), it can not be clearly said if the components of VFTS 430 lie on one isochrone. This analysis used the short period which might be an inaccurate selection. Even though it showed ellipsoidal variation with two maxima in about 2.58 days, the BBC period of 8.76 days might have been a better choice since the data points show less scattering (see Fig. 21). That is why VFTS 430 should be investigated further to refine the results of the stellar parameters. Especially the primary radius is only half the one compared to VFTS 687 but it is expected to get similar radii for both systems since VFTS 430 and VFTS 687 are supergiants (luminosity class I). In total, 6 out of 14 systems were found to probably be a (post-) mass-transferring system, making approximately 43% of all the analysed ones and 6.8% of the entire BBC sample. According to Sana et al. (2012), about 71% of O-type stars will interact with their companion. A similar proportion is also expected for early B-type stars, especially in close binaries that the eclipsing binaries are. However, the merger systems ($\sim 24\%$) have to be deducted since the product of a merger is a single star and no longer a binary. The limited lifetime of a few Myr also causes the observed interaction fraction to be lower than the Sana et al. (2012) value, meaning that some systems may interact in the future when they continue to evolve.

4.2.2 Findings based on the parameters

The stellar and orbital parameters can reveal the nature of the system, especially if they agree among different determination methods. An example is the masses and mass ratios from PHOEBE compared with the spectroscopic values for SB2 systems as well as a comparison with evolutionary tracks. One system was really outstanding in this analysis, namely VFTS 248. The masses that PHOEBE calculated were 9.8 and 7.7 solar masses are in good agreement to about 10% with the minimum

masses in Villaseñor et al. (2021) are 10.42 and 7.93 based on a high inclination of 85 degrees. VFTS 248 is an exception in the PHOEBE analysis because the mass ratio was optimized as well to test if the photometric and spectroscopic mass ratios are in agreement. The photometric mass ratio of 0.788 obtained by PHOEBE turned out to agree with the spectroscopic value of 0.76. However, due to the small radius of only 1.57 solar radii and a low temperature of about 15400 K, it would imply a mass of ~ 3 solar masses only, the lowest for a component in the studied sample.

It also turned out that, except for VFTS 248 and 206, all SB2 binaries are located close to each other in the HRD because of similar temperatures and radii and therefore luminosities. If the objects are closely located in the HRD, this would imply a mass ratio close to unity which has been confirmed for systems such as VFTS 364 and VFTS 883.

In contrast, the SB1 systems' components turned out to be located further away from each other, which can mainly be explained by the higher differences in mass. For main sequence stars, it can be said that the more massive a star becomes, the hotter and more luminous it becomes.

One exception for this is VFTS 27. Despite being an SB1 system, PHOEBE and the isochrone fitting both concluded that the mass ratio is of the order 0.9, which is very close to 1 and even closer to 1 compared to some SB2 systems. This can be caused by the contact configuration of VFTS 27, making it possible to equalize the masses of both components.

The system VFTS 248 has a good agreement on the primary masses when the PHOEBE and the Brott et al. (2011) isochrone results are compared. However, due to the parameters that PHOEBE calculated for the secondary, there is a mismatch between the PHOEBE and the isochrone mass inferred for the secondary. The secondary of VFTS 248 turned out to be the least luminous star in the studied sample at only about 100 $L_\odot$ due to its small radius of about 1.57 $R_\odot$ and a comparably low temperature of 15430 K. While PHOEBE provided a secondary mass of 7.7 $M_\odot$, the Brott et al. (2011) isochrone fitting yielded an upper limit of $5M_\odot$.

For most of the SB1 systems, however, the EMCEE mass ratios were overestimated in comparison with an estimation made by isochrones, especially the region of $0.4 < q_{\mathrm{isochr}} < 0.7$ of isochrones where the EMCEE values are at a range of $0.2 < q_{\mathrm{EMCEE}} < 0.4$. Finally, the system VFTS 430 has a comparably low mass ratio of 0.4 obtained with EMCEE compared to the isochrone fitting that yielded mass ratios of near unity. This data point can be seen at the bottom right part of both panels in Fig. 38.

It has already been a challenging task to find the correct period for VFTS 883 because the LS analysis, the BBC, and OGLE all provided different periods of about 2.330, 3.495 and 6.991 days respectively (see Fig. 24 for the phased light curves). Because the shortest period of the LS analysis still showed two distinct eclipses, it was taken for the analysis with PHOEBE. This system shows that the phased light curve has to be carefully investigated to find the true period.

5 Conclusions

After going through the exercise of complementing the results from the spectroscopic data analysis with the OGLE photometry and modelling the observational light curve with PHOEBE, this work allowed me to get constraints of the effective temperatures and radii and thus also the luminosity. The temperatures and luminosities of the components from the PHOEBE modelling were compared with isochrones to identify the mass-transferring candidates.

It can be said that, for a full determination of stellar and orbital parameters of eclipsing binaries, we need both spectroscopic and photometric data. With spectroscopy, the radial velocity, the half-amplitude of the primary, the eccentricity and the mass ratio for SB2 binaries can be measured. For the temperatures and the radii of the stars and the orbital inclination, however, a high spectral resolution would be needed which can not be provided by many spectrographs. Photometric surveys allow us to determine these parameters very precisely, which is most effective at eclipsing binaries. With the shape of the eclipses, their depth and their location in the phase-folded light curve, the temperatures, radii and the inclination can be measured. The period and eccentricity of the system could be confirmed for all eclipsing systems except for VFTS 883 where the LS, the BBC and OGLE all have different periods.

There are also some downsides when computing stellar models to reproduce the light curve of an eclipsing binary because of possible degeneracies. When the Nelder-Mead optimizer is run, it converges to a possible solution minimizing the χ^2 of the model to the observational data. Similar light curve shapes can result from different inclination angles if the mass ratio and the radii are adjusted accordingly to cause the same relative flux decrease during the eclipses. Therefore, to verify that the parameters computed by PHOEBE's optimizers are physically possible and expectable for the type of stars that are investigated, a careful look at parameters such as the masses and the surface gravities (logg) is needed. For the system VFTS 248, for example, the primary mass was calculated to be more than 33 solar masses when the mass ratio was optimized as well, resulting in its value to be around 0.46. This mass is at least twice as much as the maximum expected mass for a star at the O-B transition. When rerunning from a similar light curve shape with a mass ratio of around 0.78 and a slightly higher inclination of 86 degrees instead of 82 degrees, the masses become much more realistic with 9.8 and 7.7 solar masses respectively, being in agreement with the evolutionary masses for the primary.

Nelder-Mead alone does only provide an optimum in the set of parameters that fit well with the observational data. To estimate their uncertainties, a sampler such as EMCEE is needed. This sampling verifies how well models with small deviations from the optimal parameter set still agree with the optimized values. It can be seen that the inclination, for example, can be tightly constrained because of its heavy impact on the light curve. Other parameters can sometimes be not so tightly constrained because they do not have a significant impact on the light curve, especially the mass ratio turned out to be such a parameter.

When the masses and mass ratios from PHOEBE modelling do not match the masses they have when compared to evolutionary tracks on the HRD, the question arises as to why it occurs. In some cases, like VFTS 248, the mass ratio is comparably

low for the SB2 systems, however, the evolutionary mass difference is much more pronounced. This means that an appropriate scaling of the photometric dataset is needed to get a match between the model masses and the evolutionary masses. A possible solution for this problem can be setting up a grid of parameters to be modelled in PHOEBE that result in a similar light curve and studying their impact on the evolutionary and model masses. This can also overcome degeneracies by minimizing the difference between the evolutionary and PHOEBE masses.
The same solution can be applied to systems where the status of an ongoing or past mass transfer is uncertain, especially due to high error bars in temperatures and luminosity.
In short, the determination of the stellar and orbital parameters needs to be done carefully to avoid getting unrealistic parameters for the stars. Knowing them accurately is important to determine whether the components of a system lie on a common isochrone or not. If the uncertainties in the temperatures and the radii and thus luminosities are too high, no clear conclusion can be drawn as to whether a system can be associated with a common isochrone or not.
The logic of classifying a system as a mass-transferring or a post-mass-transfer one is based on the fact that both systems formed at the same time and should therefore be sitting on one isochrone at the beginning. If there has not been any interaction ongoing in a system, its components have evolved but it is still expected that both components lie on one common isochrone.
Due to the high impact of stellar mass on stellar evolution, especially for the main sequence lifetime, a mass transferring phase between the components is revealed if no common isochrone can be found that matches both stars. Since mass transferring systems are a subject of current research, more systems, also in other clusters, should be investigated to find out more correlations of mass transferring rates with metallicity, spectral type, orbital period or other important parameters. Eclipsing binaries are the perfect stars to study these dependencies because of the opportunity to precisely measure the parameters to put them on an HRD with isochrones.
Out of the 14 investigated objects, 6 43%) showed up to be likely a mass transfer or a post-mast transferring system. This corresponds to 6.8% of the BBC sample. Follow-up studies in both photometry and spectroscopy should allow a deeper study dedicated to these systems. It shows that finding a mass-transferring system is a challenging task, especially since more than half of the systems (50 of 88) did not show photometric variability.
Some challenges in this process should be addressed in future studies. Especially when there are degeneracies in the models, resulting in a similar light curve model with different input parameters (inclination, mass ratio, radii and effective temperatures). To solve this, a grid of models that produce a similar light curve can be inserted into PHOEBE to determine the impact of different parameters to resolve the degeneracy.
This method can also be a solution to another issue that arose when discrepancies between the spectroscopic and photometric results occurred and the dynamical masses of the systems did not agree with the evolutionary masses. With the help of the model grid, evolutionary masses and masses computed by PHOEBE can be compared and the model solution with the lowest discrepancy can be adopted.

A different issue appeared when the effective temperatures of the PHOEBE modelling were compared to the spectroscopic values. Spectroscopic temperatures can be inaccurate when the spectral type is not precisely determined and the temperature is based on that. It can also be the case that the temperatures of the PHOEBE modelling did not match the temperature expected by the spectral type. To solve this issue, more detailed studies in both spectroscopy to refine the spectral type as well as in photometry for confirmations are needed.

6 Summary

A combination of spectral and photometric observations is of high importance to get a full set of orbital and stellar parameters. Photometry becomes particularly important when it comes to measuring temperatures, radii and orbital inclinations of eclipsing binaries. Temperatures, combined with radii yield luminosities, which are then used to put the components on an HRD with isochrones. For a scientifically robust result, initial model parameters should be firstly optimized and a sampler is needed for the estimation of the parameters' uncertainties. This is made to find out whether a system has undergone a phase of mass transfer, which is confirmed with high probability for six of 14 systems. Future studies should be focused on studying the potentially mass-transferring systems in more detail, achieving a better understanding of mass transfer phases, especially how fast mass is transferred between the components and how long these phases last.

7 Kurzzusammenfassung (Deutsch)

Eine Kombination aus spektroskopischen und photometrischen Daten ist von großer Bedeutung, um einen vollständigen Satz von orbitalen und stellaren Parametern zu erhalten. Die Photometrie ist besonders wichtig, wenn es darum geht, Temperaturen, Radien und Bahnneigungen von bedeckungsveränderlichen Systemen zu messen. Die Temperaturen in Verbindung mit den Radien ergeben die Leuchtkraft, die dann verwendet wird, um die Komponenten in ein HRD mit Isochronen abzugleichen. Für ein wissenschaftlich robustes Ergebnis sollten zunächst die anfänglichen Modellparameter optimiert werden, und für die Abschätzung der Unsicherheiten der Parameter wird ein Sampler benötigt. Damit soll festgestellt werden, ob ein System eine Phase des Massentransfers durchlaufen hat, was für sechs von 14 Systemen mit hoher Wahrscheinlichkeit bestätigt wird. Zukünftige Studien sollten sich darauf konzentrieren, die potenziell massentransferierenden Systeme genauer zu untersuchen, um ein besseres Verständnis der Massentransferphasen zu erlangen, insbesondere wie schnell Masse zwischen den Komponenten übertragen wird und wie lange diese Phasen dauern.

References

Abt, Helmut A., Ana E. Gomez, and Saul G. Levy (Oct. 1990). "The Frequency and Formation Mechanism of B2–B5 Main-Sequence Binaries". In: The Astrophysical Journal Supplement 74, p. 551. DOI: 10.1086/191508.

Alard, C. (Jan. 2000). "New Powerful Methods for Photometry of CCD Images in Crowded Fields". In: IAU Colloq. 176: The Impact of Large-Scale Surveys on Pulsating Star Research. Ed. by L. Szabados and D. Kurtz. Vol. 203. Astronomical Society of the Pacific Conference Series, pp. 50–55.

Almeida, L. A. et al. (Feb. 2017). "The Tarantula Massive Binary Monitoring. I. Observational campaign and OB-type spectroscopic binaries". In: Astronomy & Astrophysics 598, A84, A84. DOI: 10.1051/0004-6361/201629844. arXiv: 1610.03500 [astro-ph.SR].

El-Badry, Kareem, Hans-Walter Rix, and Tyler M. Heintz (Sept. 2021). "A million binaries from Gaia eDR3: sample selection and validation of Gaia parallax uncertainties". In: Monthly Notices of the Royal Astronomical Society 506.2, pp. 2269–2295. DOI: 10.1093/mnras/stab323. arXiv: 2101.05282 [astro-ph.SR].

Banyard, G. et al. (Feb. 2022). "The observed multiplicity properties of B-type stars in the Galactic young open cluster NGC 6231". In: Astronomy & Astrophysics 658, A69, A69. DOI: 10.1051/0004-6361/202141037. arXiv: 2108.07814 [astro-ph.SR].

Bernstein, Rebecca et al. (Mar. 2003). "MIKE: A Double Echelle Spectrograph for the Magellan Telescopes at Las Campanas Observatory". In: Instrument Design and Performance for Optical/Infrared Ground-based Telescopes. Ed. by Masanori Iye and Alan F. M. Moorwood. Vol. 4841. Society of Photo-Optical Instrumentation Engineers (SPIE) Conference Series, pp. 1694–1704. DOI: 10.1117/12.461502.

Bohlin, Ralph C., Ivan Hubeny, and Thomas Rauch (July 2020). "New Grids of Pure-hydrogen White Dwarf NLTE Model Atmospheres and the HST/STIS Flux Calibration". In: AJ 160.1, 21, p. 21. DOI: 10.3847/1538-3881/ab94b4. arXiv: 2005.10945 [astro-ph.SR].

Brott, I. et al. (June 2011). "Rotating massive main-sequence stars. I. Grids of evolutionary models and isochrones". In: A&A 530, A115, A115. DOI: 10.1051/0004-6361/201016113. arXiv: 1102.0530 [astro-ph.SR].

Chen, Yang et al. (Nov. 2014). "Improving PARSEC models for very low mass stars". In: MNRAS 444.3, pp. 2525–2543. DOI: 10.1093/mnras/stu1605. arXiv: 1409.0322 [astro-ph.SR].

Chen, Yang et al. (Sept. 2015). "PARSEC evolutionary tracks of massive stars up to 350 $M_\odot$ at metallicities $0.0001 \leq Z \leq 0.04$". In: MNRAS 452.1, pp. 1068–1080. DOI: 10.1093/mnras/stv1281. arXiv: 1506.01681 [astro-ph.SR].

Collier Cameron, A. et al. (Dec. 2006). "A fast hybrid algorithm for exoplanetary transit searches". In: Monthly Notices of the Royal Astronomical Society 373.2, pp. 799–810. DOI: 10.1111/j.1365-2966.2006.11074.x. arXiv: astro-ph/0609418 [astro-ph].

Daszyńska-Daszkiewicz, Jadwiga and Amadeusz Miszuda (Nov. 2019). "Age Determination of Galactic B-type Stars in Double-lined Eclipsing Binaries". In: The Astrophysical Journal 886.1, 35, p. 35. DOI: 10.3847/1538-4357/ab4133. arXiv: 1909.04392 [astro-ph.SR].

Djurašević, G. et al. (Jan. 2011). "Physical parameters of close binaries QX Andromedae, RW Comae Berenices, MR Delphini, and BD +079° 3142". In: Astronomy & Astrophysics 525, A66, A66. DOI: 10.1051/0004-6361/201014895. arXiv: 1011.3677 [astro-ph.SR].

Duchêne, Gaspard and Adam Kraus (2013). "Stellar Multiplicity". In: Annual Review of Astronomy and Astrophysics 51.Volume 51, 2013, pp. 269–310. ISSN: 1545-4282. DOI: https://doi.org/10.1146/annurev-astro-081710-102602. URL: https://www.annualreviews.org/content/journals/10.1146/annurev-astro-081710-102602.

Dunstall, P. R. et al. (2012). "The VLT-FLAMES Tarantula Survey V: The peculiar B[e]-like supergiant, VFTS698, in 30 Doradus". In: Astronomy & Astrophysics 542.A50, pp. 1–17. ISSN: 1432-0746. DOI: 10.1051/0004-6361/201218872. URL: https://doi.org/10.1051/0004-6361/201218872.

Dunstall, P. R. et al. (Aug. 2015). "The VLT-FLAMES Tarantula Survey. XXII. Multiplicity properties of the B-type stars". In: Astronomy & Astrophysics 580, A93, A93. DOI: 10.1051/0004-6361/201526192. arXiv: 1505.07121 [astro-ph.SR].

Eggleton, P. P. (May 1983). "Aproximations to the radii of Roche lobes." In: The Astrophysical Journal 268, pp. 368–369. DOI: 10.1086/160960.

Erkal, D et al. (May 2019). "The total mass of the Large Magellanic Cloud from its perturbation on the Orphan stream". In: Monthly Notices of the Royal Astronomical Society 487.2, pp. 2685–2700. ISSN: 1365-2966. DOI: 10.1093/mnras/stz1371. URL: http://dx.doi.org/10.1093/mnras/stz1371.

Essam, A. et al. (Jan. 2016). "THE FIRST PHOTOMETRIC ANALYSES OF THE ALGOL BINARY SYSTEMS GSC 04328-02164 AND GSC 03164-01558". In: The Astronomical Journal 151.1, p. 19. DOI: 10.3847/0004-6256/151/1/19. URL: https://dx.doi.org/10.3847/0004-6256/151/1/19.

Evans, C. J. et al. (June 2011). "The VLT-FLAMES Tarantula Survey. I. Introduction and observational overview". In: Astronomy & Astrophysics 530, A108, A108. DOI: 10.1051/0004-6361/201116782. arXiv: 1103.5386 [astro-ph.SR].

Evans, C. J. et al. (Feb. 2015). "The VLT-FLAMES Tarantula Survey. XVIII. Classifications and radial velocities of the B-type stars". In: Astronomy & Astrophysics 574, A13, A13. DOI: 10.1051/0004-6361/201424414. arXiv: 1501.04108 [astro-ph.SR].

Faccioli, Lorenzo et al. (Nov. 2007). "Eclipsing Binary Stars in the Large and Small Magellanic Clouds from the MACHO Project: The Sample". In: The Astronomical Journal 134.5, pp. 1963–1993. DOI: 10.1086/521579. arXiv: 0711.1617 [astro-ph].

Fahrion, Katja and Guido De Marchi (Jan. 2024). "The hierarchical formation of 30 Doradus as seen by JWST". In: Astronomy & Astrophysics 681, A20, A20. DOI: 10.1051/0004-6361/202348097. arXiv: 2311.06336 [astro-ph.GA].

Frankel, Neige et al. (Mar. 2024). "What Does the Large Magellanic Cloud Look Like? It Depends on [M/H] and Age". In: arXiv e-prints, arXiv:2403.08516, arXiv:2403.08516. DOI: 10.48550/arXiv.2403.08516. arXiv: 2403.08516 [astro-ph.GA].

Garland, R. et al. (July 2017). "The VLT-FLAMES Tarantula Survey. XXVII. Physical parameters of B-type main-sequence binary systems in the Tarantula nebula". In: Astronomy & Astrophysics 603, A91, A91. DOI: 10.1051/0004-6361/201629982. arXiv: 1704.07131 [astro-ph.SR].

Gosnell, Natalie M. et al. (Nov. 2019). "Constraining Mass-transfer Histories of Blue Straggler Stars with COS Spectroscopy of White Dwarf Companions". In: The Astrophysical Journal 885.1, 45, p. 45. DOI: 10.3847/1538-4357/ab4273. arXiv: 1904.02280 [astro-ph.SR].

Heber, Ulrich (Oct. 2024). "Hot Subdwarf Stars". In: arXiv e-prints, arXiv:2410.11663, arXiv:2410.11663. DOI: 10.48550/arXiv.2410.11663. arXiv: 2410.11663 [astro-ph.SR].

Iglesias-Marzoa, Ramón, Mercedes López-Morales, and María Jesús Arévalo Morales (June 2015). "The rvfit Code: A Detailed Adaptive Simulated Annealing Code for Fitting Binaries and Exoplanets Radial Velocities". In: Publications of the Astronomical Society of the Pacific 127.952, p. 567. DOI: 10.1086/682056. URL: https://dx.doi.org/10.1086/682056.

IJspeert, L. W. et al. (Sept. 2024). "Statistical view of orbital circularisation with 14 000 characterised TESS eclipsing binaries". In: arXiv e-prints, arXiv:2409.20540, arXiv:2409.20540. DOI: 10.48550/arXiv.2409.20540. arXiv: 2409.20540 [astro-ph.SR].

Klement, R. et al. (Jan. 2025). "VLTI/GRAVITY enables the determination of the first dynamical masses of a classical Be + stripped and bloated pre-subdwarf binary". In: arXiv e-prints, arXiv:2501.04103, arXiv:2501.04103. DOI: 10.48550/arXiv.2501.04103. arXiv: 2501.04103 [astro-ph.SR].

Kobulnicky, Henry A. et al. (Aug. 2014). "Toward Complete Statistics of Massive Binary Stars: Penultimate Results from the Cygnus OB2 Radial Velocity Survey". In: The Astrophysical Journal Supplement 213.2, 34, p. 34. DOI: 10.1088/0067-0049/213/2/34. arXiv: 1406.6655 [astro-ph.SR].

Koumpia, E. and A. Z. Bonanos (Nov. 2012). "Fundamental parameters of four massive eclipsing binaries in Westerlund 1". In: Astronomy & Astrophysics 547, A30, A30. DOI: 10.1051/0004-6361/201219465. arXiv: 1108.4453 [astro-ph.SR].

Kroupa, P. (Jan. 2002). "The Initial Mass Function and Its Variation (Review)". In: Modes of Star Formation and the Origin of Field Populations. Ed. by Eva K. Grebel and Walfgang Brandner. Vol. 285. Astronomical Society of the Pacific Conference Series, p. 86. DOI: 10.48550/arXiv.astro-ph/0102155. arXiv: astro-ph/0102155 [astro-ph].

Kroupa, Pavel (Apr. 2001). "On the variation of the initial mass function". In: Monthly Notices of the Royal Astronomical Society 322.2, pp. 231–246. ISSN: 0035-8711. DOI: 10.1046/j.1365-8711.2001.04022.x. eprint: https://academic.oup.com/mnras/article-pdf/322/2/231/2852412/322-2-231.pdf. URL: https://doi.org/10.1046/j.1365-8711.2001.04022.x.

Lennon, D. J. et al. (Aug. 2024). "Rotational synchronisation of B-type binaries in 30 Doradus". In: Astronomy & Astrophysics 688, A141, A141. DOI: 10.1051/0004-6361/202450583. arXiv: 2405.17608 [astro-ph.SR].

Li, Fu-Xing et al. (Dec. 2024). "Evolutionary States and Triplicity of Four Massive Semidetached Binaries with Long-term Decreasing Orbital Periods in the LMC". In: The Astrophysical Journal 976.2, 158, p. 158. DOI: 10.3847/1538-4357/ad855e. arXiv: 2411.03592 [astro-ph.SR].

Liu, Jian-Fei et al. (Nov. 2024). "Spectroscopic and photometric investigations of the totally eclipsing contact binary V1320 Cas". In: New Astronomy 112, 102254, p. 102254. DOI: 10.1016/j.newast.2024.102254.

Lomb, N. R. (Feb. 1976). "Least-Squares Frequency Analysis of Unequally Spaced Data". In: Astrophysics and Space Science 39.2, pp. 447–462. DOI: 10.1007/BF00648343.

Lucy, L. B. and R. E. Wilson (July 1979). "Observational tests of theories of contact binaries." In: The Astrophysical Journal 231, pp. 502–513. DOI: 10.1086/157212.

Mahy, L. et al. (Feb. 2020). "The Tarantula Massive Binary Monitoring. IV. Double-lined photometric binaries". In: Astronomy & Astrophysics 634, A119, A119. DOI: 10.1051/0004-6361/201936152. arXiv: 1912.06853 [astro-ph.SR].

Marchant, Pablo and Julia Bodensteiner (2023). The Evolution of Massive Binary Stars. arXiv: 2311.01865 [astro-ph.SR]. URL: https://arxiv.org/abs/2311.01865.

McEvoy, C. M. et al. (Mar. 2015). "The VLT-FLAMES Tarantula Survey. XIX. B-type supergiants: Atmospheric parameters and nitrogen abundances to investigate the role of binarity and the width of the main sequence". In: Astronomy & Astrophysics 575, A70, A70. DOI: 10.1051/0004-6361/201425202. arXiv: 1412.2705 [astro-ph.SR].

Moe, Maxwell and Rosanne Di Stefano (Sept. 2015). "Early-type Eclipsing Binaries with Intermediate Orbital Periods". In: ApJ 810.1, 61, p. 61. DOI: 10.1088/0004-637X/810/1/61. arXiv: 1501.03152 [astro-ph.SR].

— (June 2017). "Mind Your Ps and Qs: The Interrelation between Period (P) and Mass-ratio (Q) Distributions of Binary Stars". In: The Astrophysical Journal Supplement 230.2, 15, p. 15. DOI: 10.3847/1538-4365/aa6fb6. arXiv: 1606.05347 [astro-ph.SR].

Offner, S. S. R. et al. (July 2023). "The Origin and Evolution of Multiple Star Systems". In: Protostars and Planets VII. Ed. by S. Inutsuka et al. Vol. 534. Astronomical Society of the Pacific Conference Series, p. 275. DOI: DOI:10.26624/LSUL6799. arXiv: 2203.10066 [astro-ph.SR].

Öztürk, Oğuz and Ahmet Erdem (Aug. 2023). "First photometric study of three eclipsing binary star systems: V495 Aur, V589 Aur and V478 Cam". In: New Astronomy 102, 102036, p. 102036. DOI: 10.1016/j.newast.2023.102036.

Paczynski, B. et al. (May 1997). "Massive Automated Variability Search With OGLE-2". In: American Astronomical Society Meeting Abstracts #190. Vol. 190. American Astronomical Society Meeting Abstracts, 26.06, p. 26.06.

Pastorelli, Giada et al. (Nov. 2020). "Constraining the thermally pulsing asymptotic giant branch phase with resolved stellar populations in the Large Magellanic

Cloud". In: MNRAS 498.3, pp. 3283–3301. DOI: 10.1093/mnras/staa2565. arXiv: 2008.08595 [astro-ph.SR].

Pawlak, M. et al. (Dec. 2016). "The OGLE Collection of Variable Stars. Eclipsing Binaries in the Magellanic System". In: Acta Astronomica 66.4, pp. 421–432. DOI: 10.48550/arXiv.1612.06394. arXiv: 1612.06394 [astro-ph.SR].

Pecaut, Mark J. and Eric E. Mamajek (Sept. 2013). "INTRINSIC COLORS, TEMPERATURES, AND BOLOMETRIC CORRECTIONS OF PRE-MAIN-SEQUENCE STARS". In: The Astrophysical Journal Supplement Series 208.1, p. 9. ISSN: 1538-4365. DOI: 10.1088/0067-0049/208/1/9. URL: http://dx.doi.org/10.1088/0067-0049/208/1/9.

Pellouin, Clément, Irina Dvorkin, and Léonard Lehoucq (Nov. 2024). "Evolutionary tracks of binary neutron star progenitors across cosmic times". In: arXiv e-prints, arXiv:2411.04563, arXiv:2411.04563. DOI: 10.48550/arXiv.2411.04563. arXiv: 2411.04563 [astro-ph.HE].

Pietrzyński, G. et al. (Mar. 2013). "An eclipsing-binary distance to the Large Magellanic Cloud accurate to two per cent". In: Nature 495.7439, pp. 76–79. ISSN: 1476-4687. DOI: 10.1038/nature11878. URL: http://dx.doi.org/10.1038/nature11878.

Prša, A. and T. Zwitter (July 2005). "A Computational Guide to Physics of Eclipsing Binaries. I. Demonstrations and Perspectives". In: The Astrophysical Journal 628.1, pp. 426–438. DOI: 10.1086/430591. arXiv: astro-ph/0503361 [astro-ph].

Prša, Andrej et al. (Jan. 2022). "TESS Eclipsing Binary Stars. I. Short-cadence Observations of 4584 Eclipsing Binaries in Sectors 1-26". In: The Astrophysical Journal Supplement 258.1, 16, p. 16. DOI: 10.3847/1538-4365/ac324a. arXiv: 2110.13382 [astro-ph.SR].

Ramachandran, Varsha et al. (Apr. 2019). "Testing massive star evolution, star formation history, and feedback at low metallicity Spectroscopic analysis of OB stars in the SMC Wing". In: Astronomy and Astrophysics 625. DOI: 10.1051/0004-6361/201935365.

Rodríguez, C. N. et al. (Dec. 2021). "Fundamental parameters of the massive eclipsing binary HM1 8". In: MNRAS 508.2, pp. 2179–2193. DOI: 10.1093/mnras/stab2699. arXiv: 2109.13054 [astro-ph.SR].

Salpeter, Edwin E. (Jan. 1955). "The Luminosity Function and Stellar Evolution." In: Astrophysical Journal 121, p. 161. DOI: 10.1086/145971.

Sana, H. et al. (July 2012). "Binary Interaction Dominates the Evolution of Massive Stars". In: Science 337.6093, p. 444. DOI: 10.1126/science.1223344. arXiv: 1207.6397 [astro-ph.SR].

Sana, H. et al. (Feb. 2013). "The VLT-FLAMES Tarantula Survey. VIII. Multiplicity properties of the O-type star population". In: Astronomy & Astrophysics 550, A107, A107. DOI: 10.1051/0004-6361/201219621. arXiv: 1209.4638 [astro-ph.SR].

Scargle, J. D. (Dec. 1982). "Studies in astronomical time series analysis. II. Statistical aspects of spectral analysis of unevenly spaced data." In: The Astrophysical Journal 263, pp. 835–853. DOI: 10.1086/160554.

Schneider, F. R. N. et al. (Oct. 2018). "The VLT-FLAMES Tarantula Survey. XXIX. Massive star formation in the local 30 Doradus starburst". In:

Astronomy & Astrophysics 618, A73, A73. DOI: 10.1051/0004-6361/201833433. arXiv: 1807.03821 [astro-ph.SR].

Scowen, Paul et al. (Sept. 2019). "PolStar - An Explorer-Class FUV Spectropolarimetry Mission to Map the Environments of Massive Stars". In: Bulletin of the American Astronomical Society. Vol. 51, 167, p. 167. DOI: 10.48550/arXiv.1911.06724. arXiv: 1911.06724 [astro-ph.SR].

Tang, Jing et al. (Dec. 2014). "New PARSEC evolutionary tracks of massive stars at low metallicity: testing canonical stellar evolution in nearby star-forming dwarf galaxies". In: MNRAS 445.4, pp. 4287–4305. DOI: 10.1093/mnras/stu2029. arXiv: 1410.1745 [astro-ph.SR].

Temmink, K. D. et al. (Jan. 2023). "Coping with loss. Stability of mass transfer from post-main-sequence donor stars". In: Astronomy & Astrophysics 669, A45, A45. DOI: 10.1051/0004-6361/202244137. arXiv: 2209.12707 [astro-ph.SR].

Townsley, Leisa K., Patrick S. Broos, and Matthew S. Povich (July 2024). "T-ReX: The Tarantula—Revealed by X-Rays". In: The Astrophysical Journal Supplement 273.1, 5, p. 5. DOI: 10.3847/1538-4365/ad435c. arXiv: 2403.16944 [astro-ph.HE].

Trabucchi, Michele et al. (Nov. 2021). "Modelling long-period variables - II. Fundamental mode pulsation in the non-linear regime". In: MNRAS 500.2, pp. 1575–1591. DOI: 10.1093/mnras/staa3356. arXiv: 2010.13654 [astro-ph.SR].

Udalski, A. (Dec. 2003). "The Optical Gravitational Lensing Experiment. Real Time Data Analysis Systems in the OGLE-III Survey". In: Acta Astronomica 53, pp. 291–305. DOI: 10.48550/arXiv.astro-ph/0401123. arXiv: astro-ph/0401123 [astro-ph].

Udalski, A., M. K. Szymański, and G. Szymański (Mar. 2015). "OGLE-IV: Fourth Phase of the Optical Gravitational Lensing Experiment". In: Acta Astronomica 65.1, pp. 1–38. DOI: 10.48550/arXiv.1504.05966. arXiv: 1504.05966 [astro-ph.SR].

Udalski, A. et al. (Oct. 1992). "The Optical Gravitational Lensing Experiment". In: Acta Astronomica 42, pp. 253–284.

Villaseñor, J. I. et al. (Nov. 2021). "The B-type binaries characterization programme I. Orbital solutions for the 30 Doradus population". In: Monthly Notices of the Royal Astronomical Society 507.4, pp. 5348–5375. DOI: 10.1093/mnras/stab2197. arXiv: 2107.10170 [astro-ph.SR].

Vink, Jorick S. (Aug. 2022). "Theory and Diagnostics of Hot Star Mass Loss". In: Annual Review of Astronomy and Astrophysics 60, pp. 203–246. DOI: 10.1146/annurev-astro-052920-094949. arXiv: 2109.08164 [astro-ph.SR].

Walborn, N. R. et al. (Apr. 2014). "The VLT-FLAMES Tarantula Survey. XIV. The O-type stellar content of 30 Doradus". In: Astronomy & Astrophysics 564, A40, A40. DOI: 10.1051/0004-6361/201323082. arXiv: 1402.6969 [astro-ph.SR].

Zasche, P. and M. Wolf (Feb. 2019). "Apsidal Motion and Absolute Parameters of 21 Early-type Small Magellanic Cloud Eccentric Eclipsing Binaries". In: The Astronomical Journal 157.2, p. 87. DOI: 10.3847/1538-3881/aafc31. URL: https://dx.doi.org/10.3847/1538-3881/aafc31.

A Model solutions

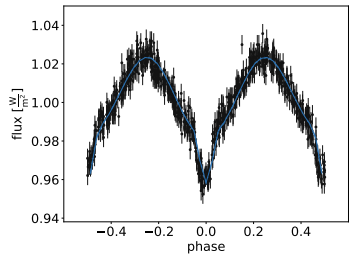

(a) VFTS 27 model solution

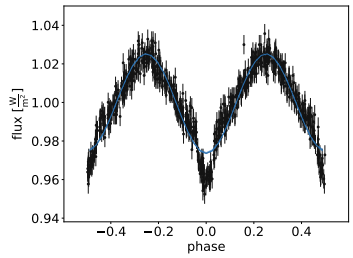

(b) VFTS 27 contact binary model solution

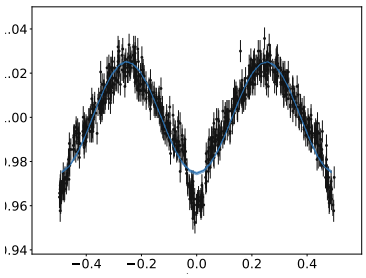

(c) VFTS 27 semi-detached binary model solution

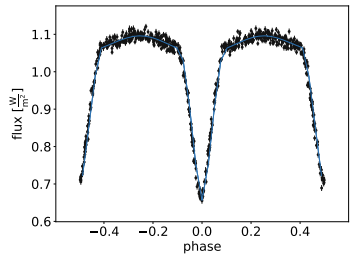

(d) VFTS 112 binary model solution

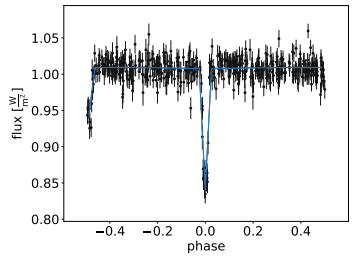

(e) VFTS 157 binary model solution

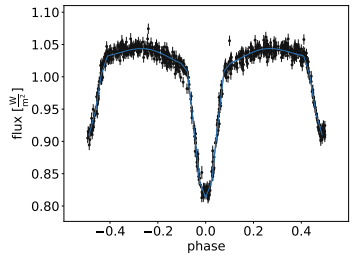

(f) VFTS 189 binary model solution

Figure 40: EMCEE model solutions

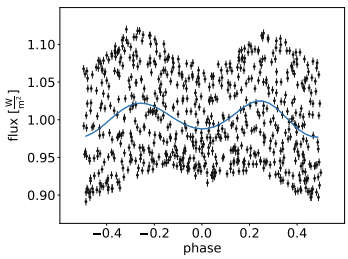

(g) VFTS 206 binary model solution

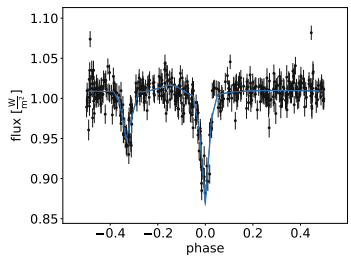

(h) VFTS 215 binary model solution

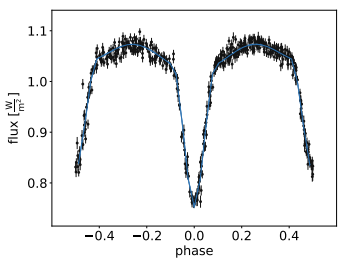

(i) VFTS 240 binary model solution

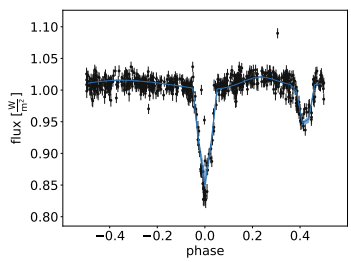

(j) VFTS 248 binary model solution

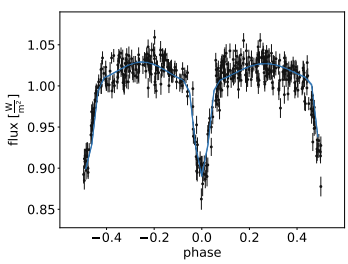

(k) VFTS 255 binary model solution

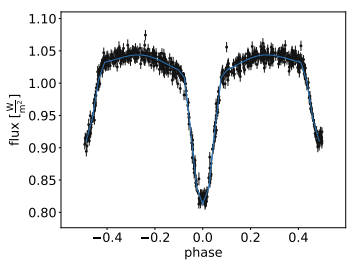

(l) VFTS 364 binary model solution

Figure 40: Continued.

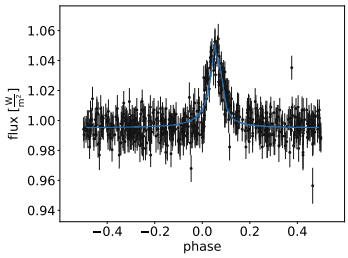

(m) VFTS 388 binary model solution

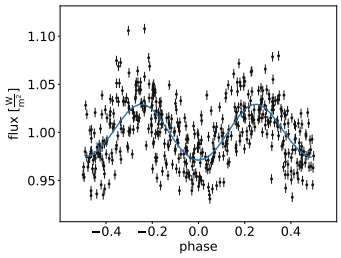

(n) VFTS 430 binary model solution

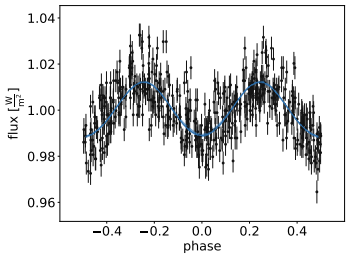

(o) VFTS 687 binary model solution

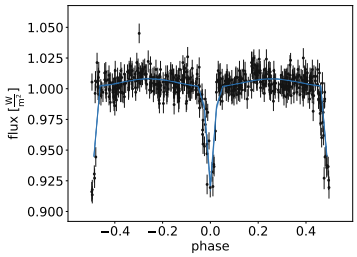

(p) VFTS 883 binary model solution

Figure 40: Continued.

B EMCEE corner plots

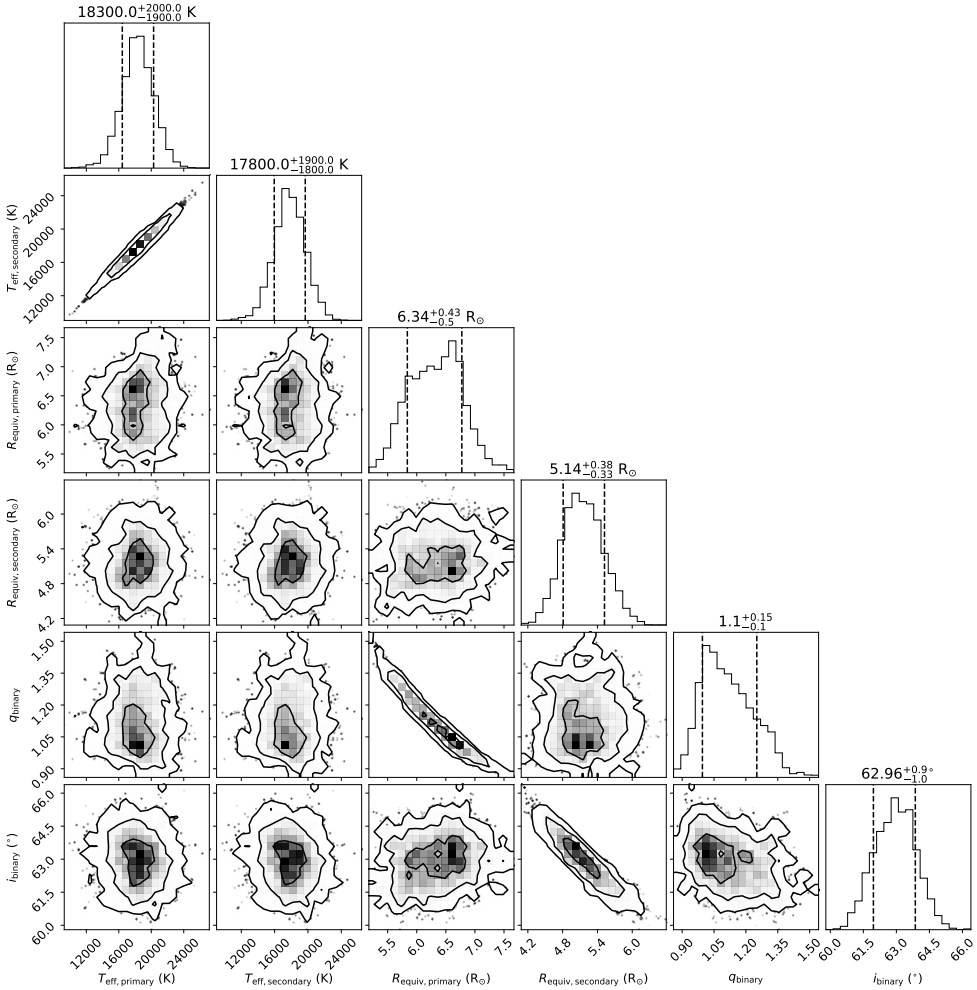

Figure 41: EMCEE corner plot for VFTS 27 (detached configuration)

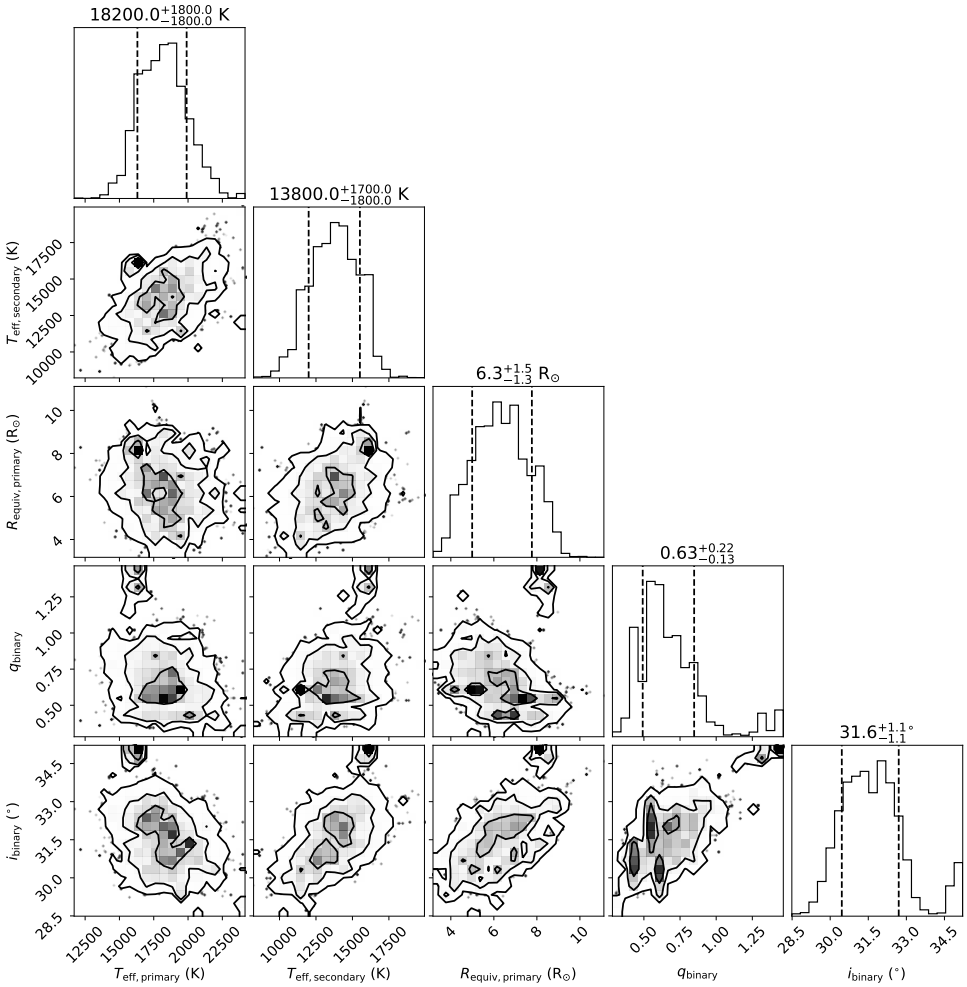

Figure 42: EMCEE corner plot for VFTS 27 (semi-detached configuration)

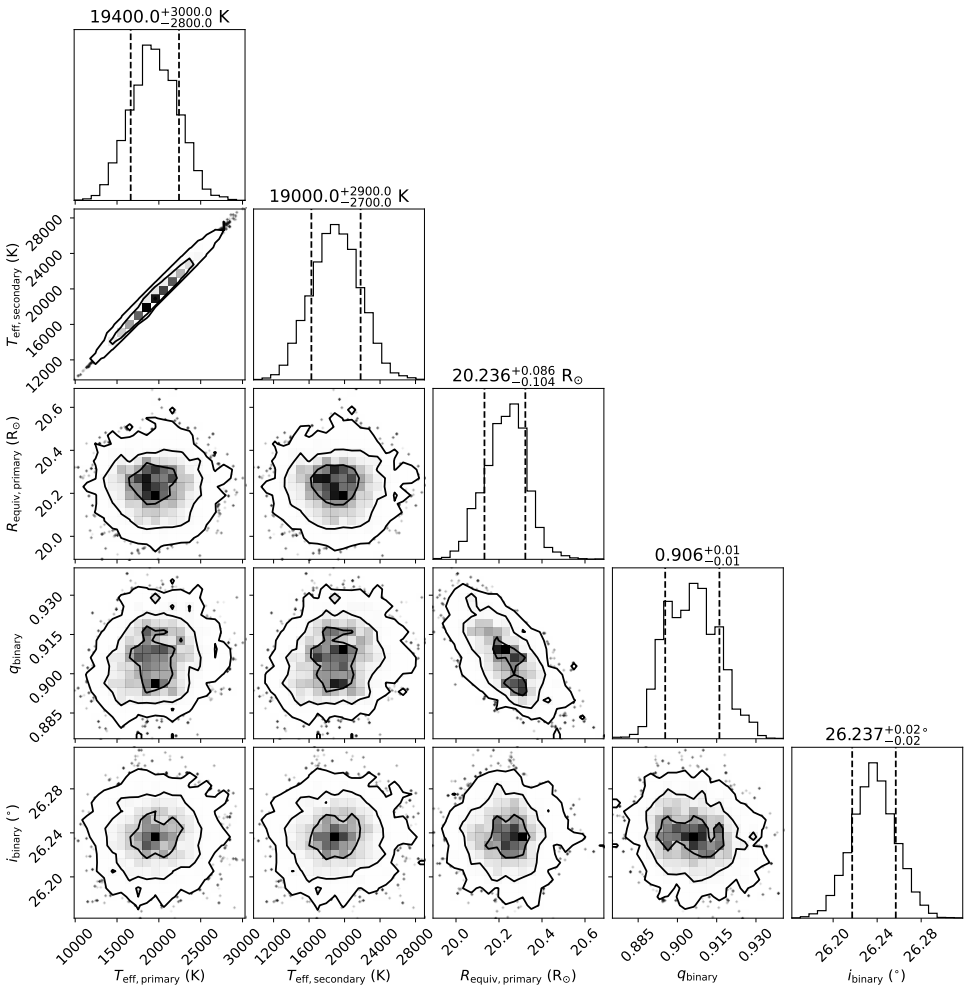

Figure 43: EMCEE corner plot for VFTS 27 with contact binary configuration

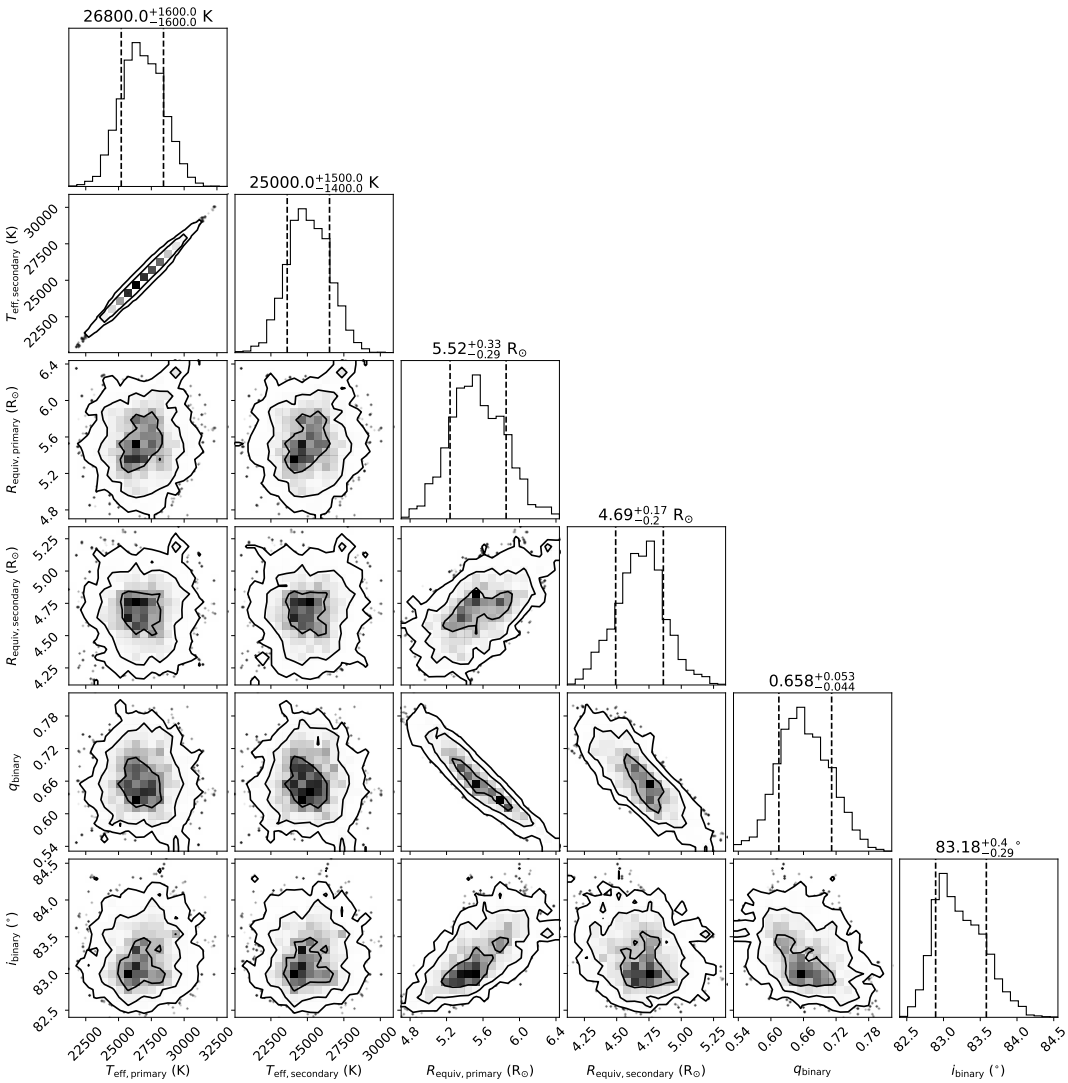

Figure 44: EMCEE corner plot for VFTS 112

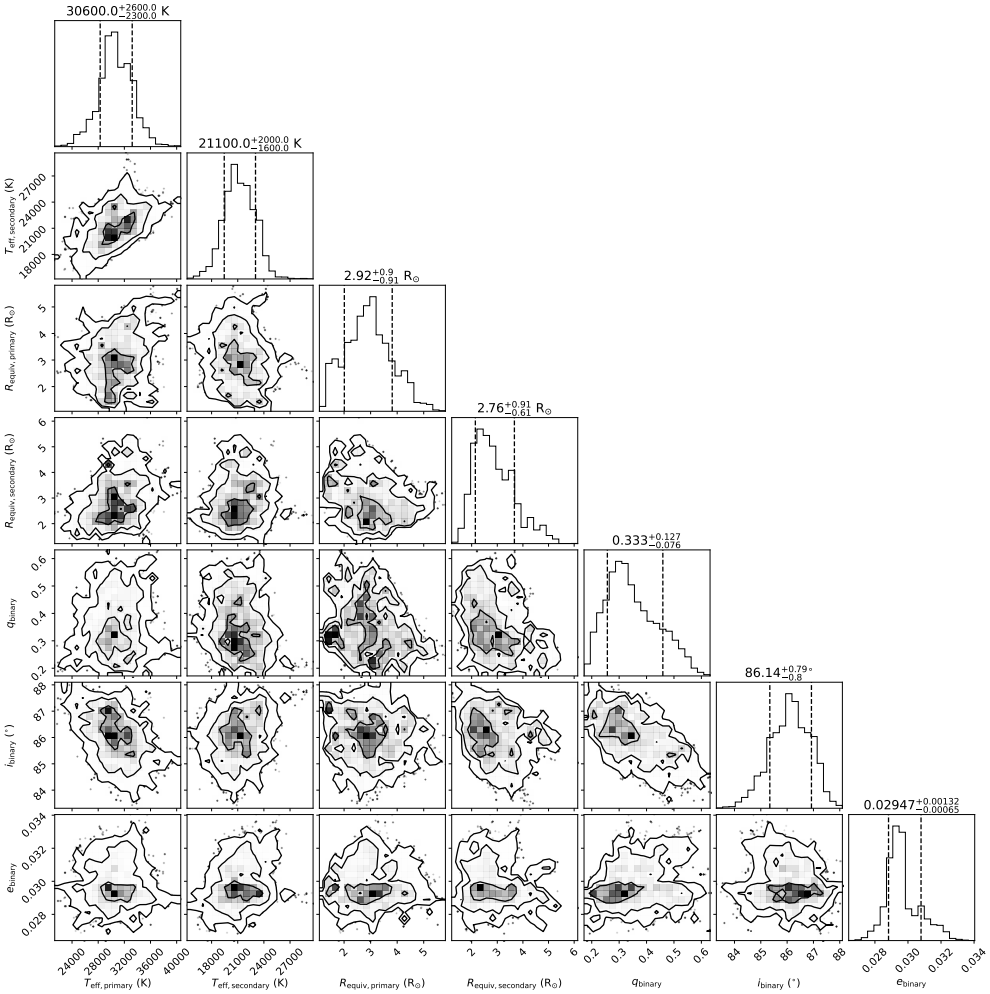

Figure 45: EMCEE corner plot for VFTS 157

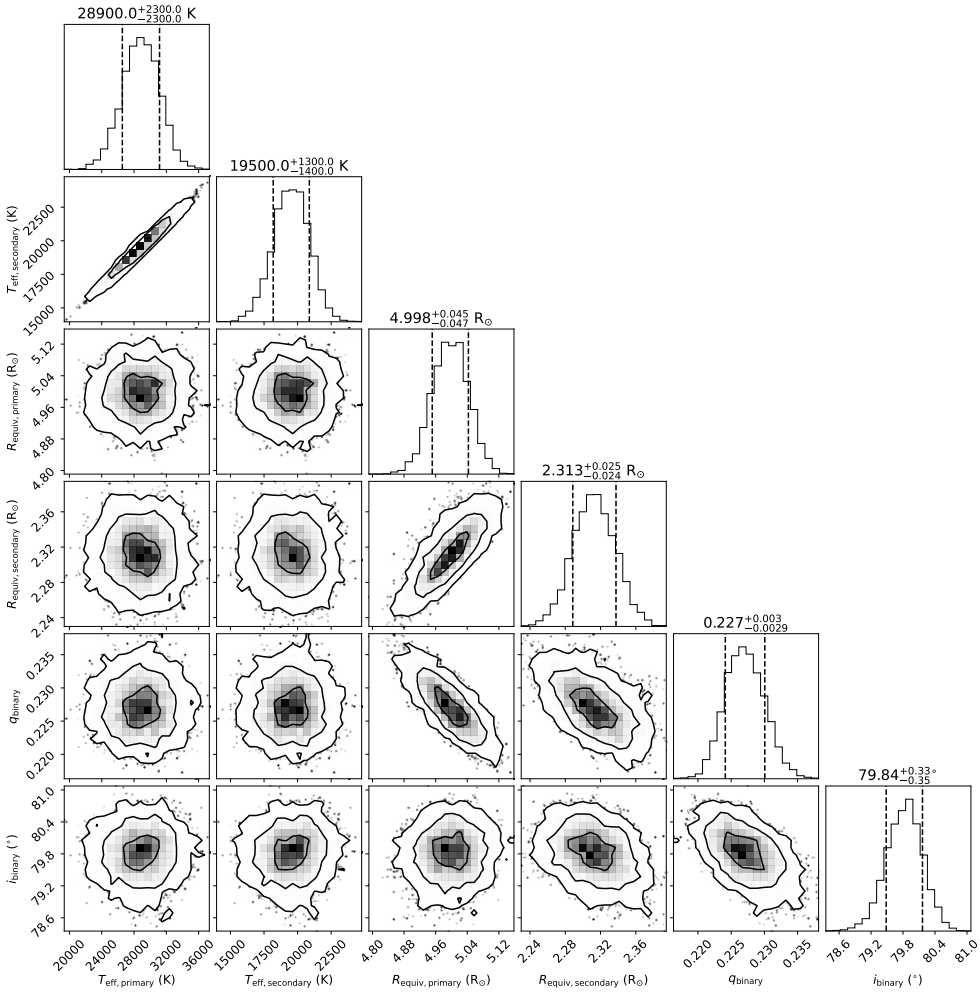

Figure 46: EMCEE corner plot for VFTS 189

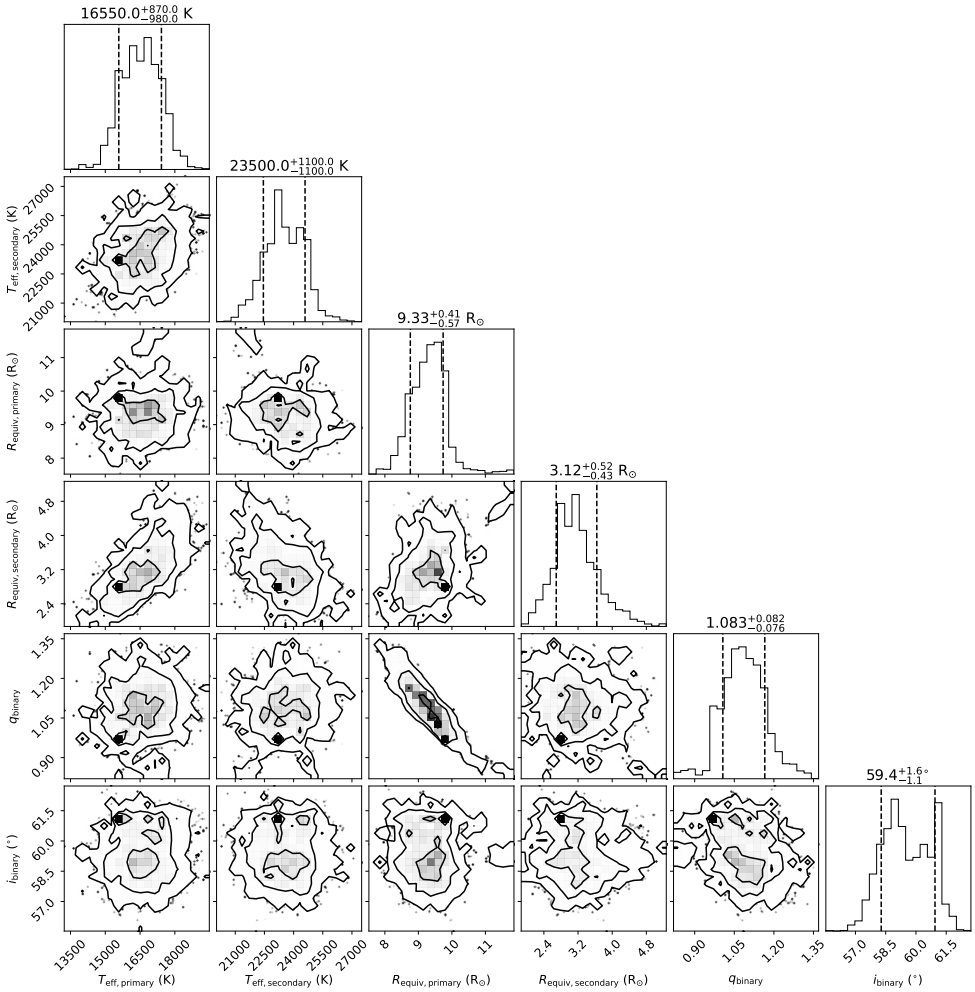

Figure 47: EMCEE corner plot for VFTS 206

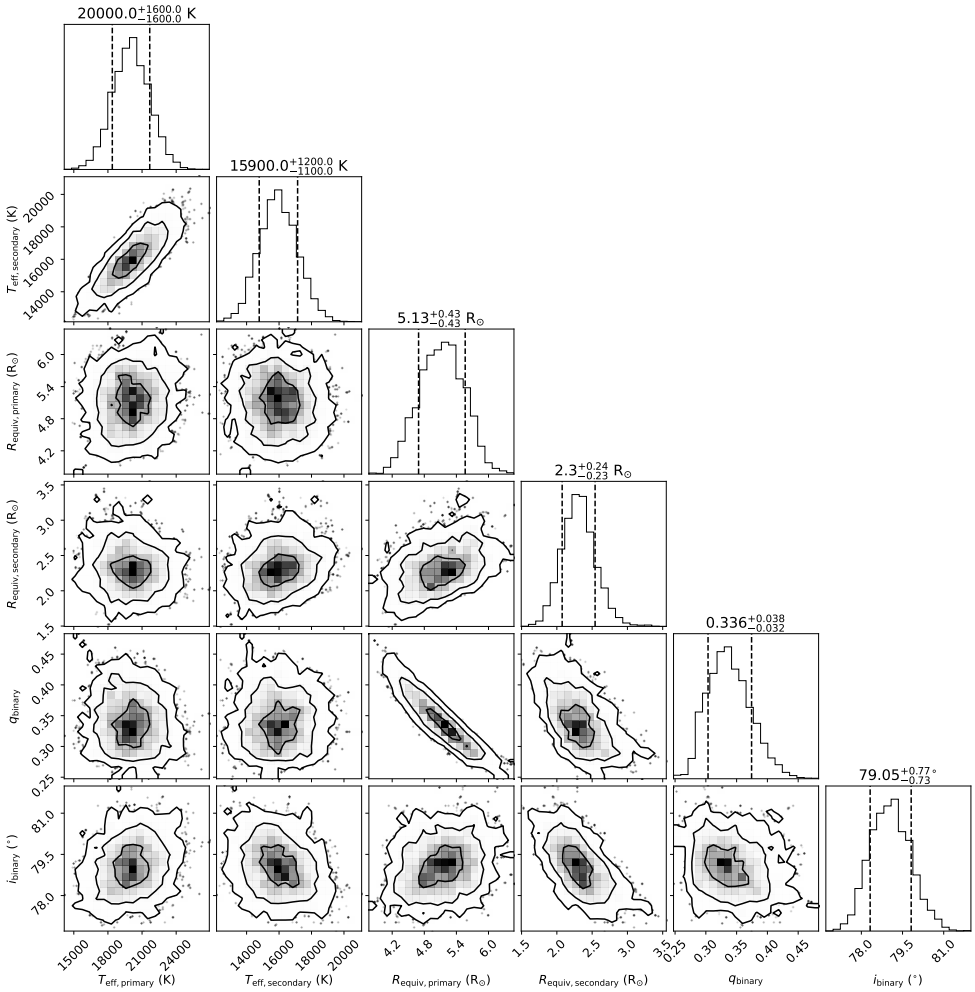

Figure 48: EMCEE corner plot for VFTS 215

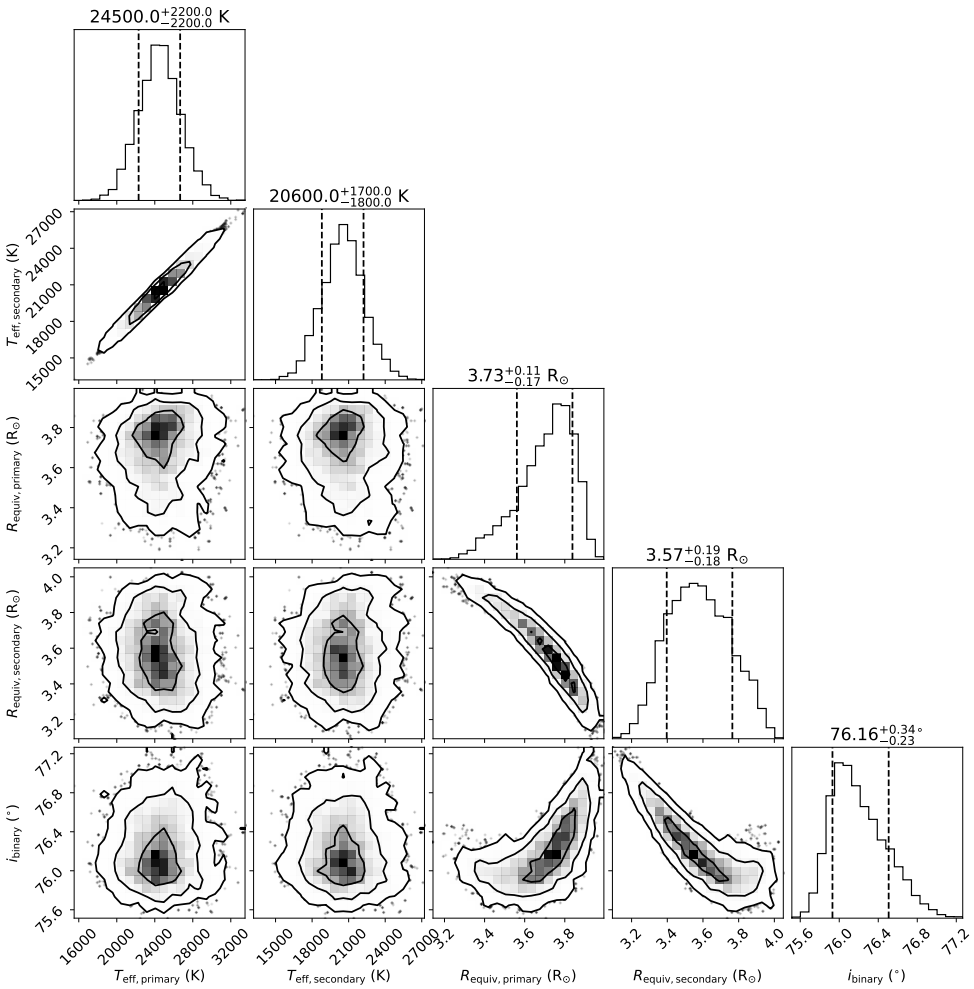

Figure 49: EMCEE corner plot for VFTS 240

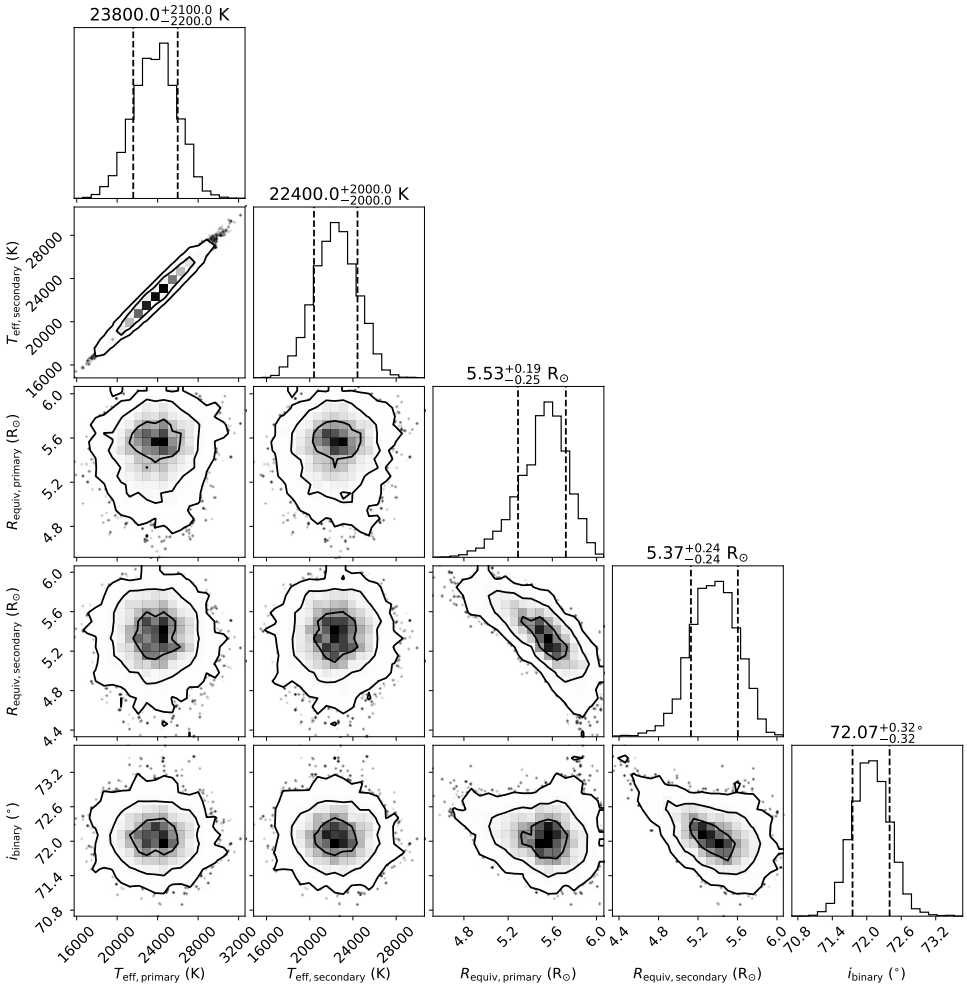

Figure 50: EMCEE corner plot for VFTS 255

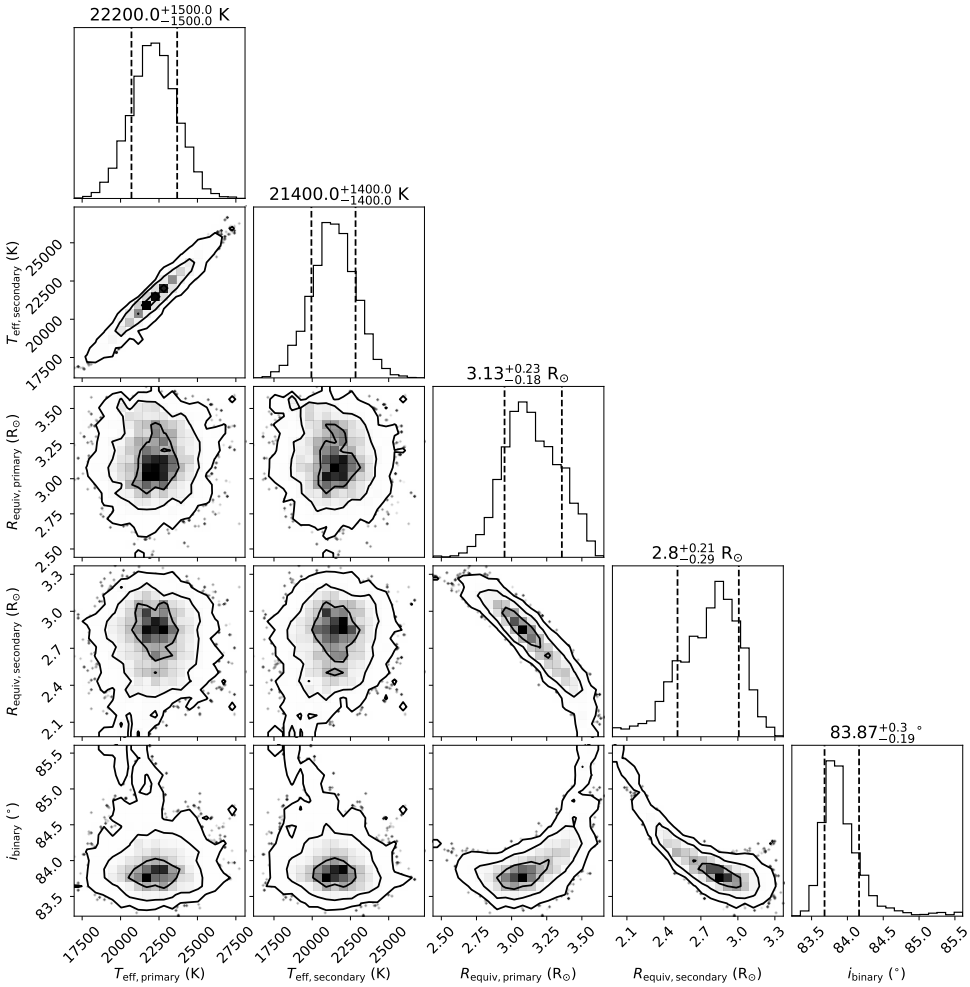

Figure 51: EMCEE corner plot for VFTS 364

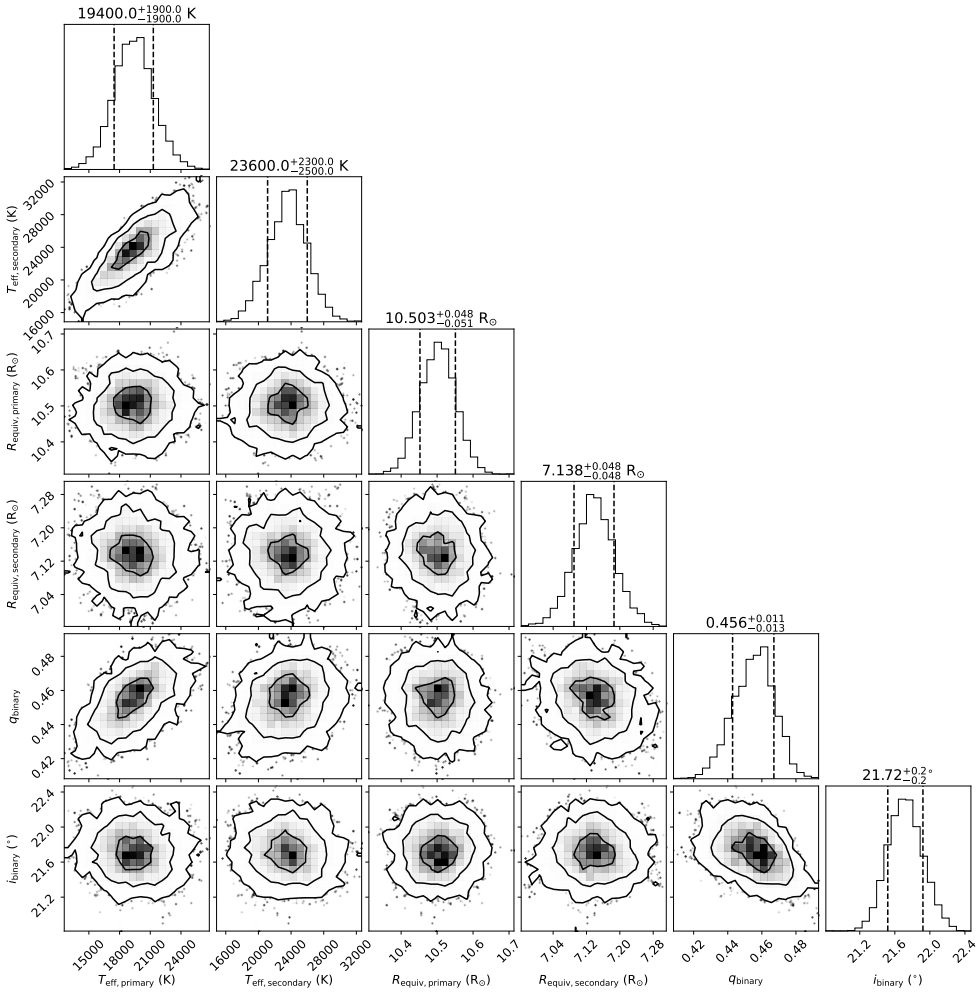

Figure 52: EMCEE corner plot for VFTS 388

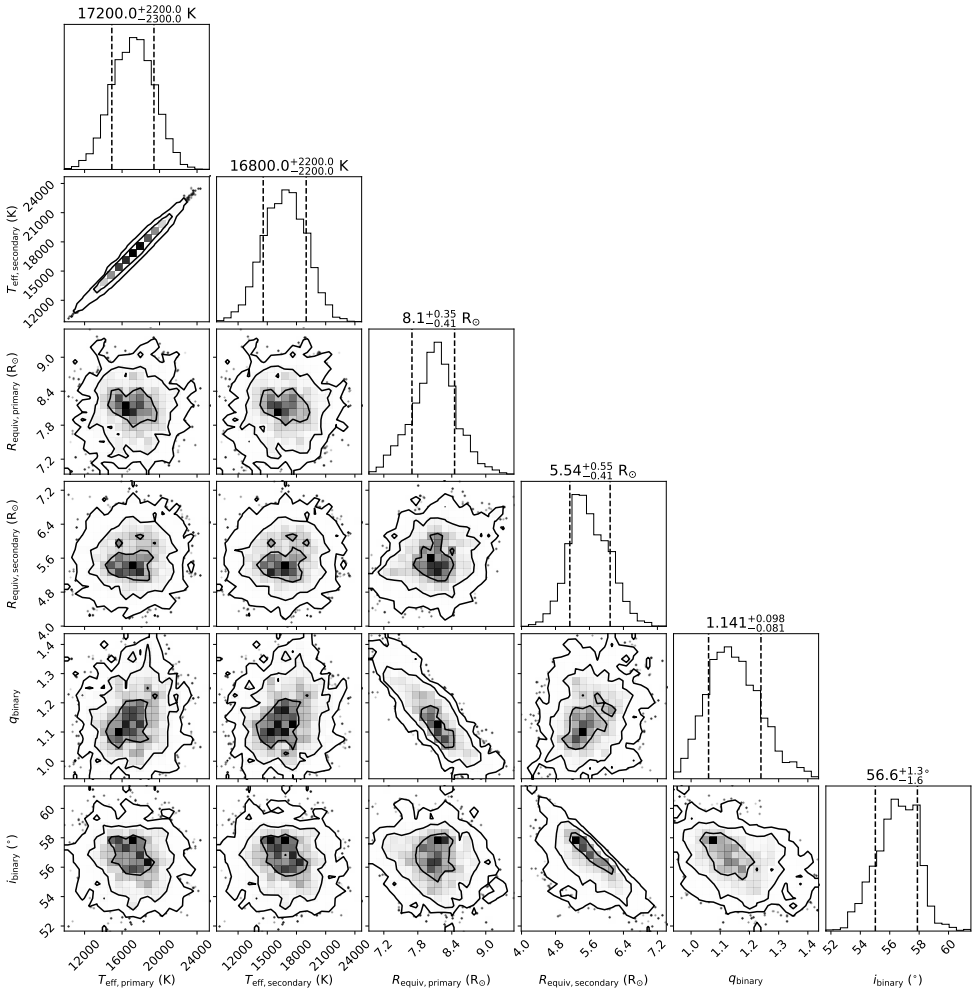

Figure 53: EMCEE corner plot for VFTS 430

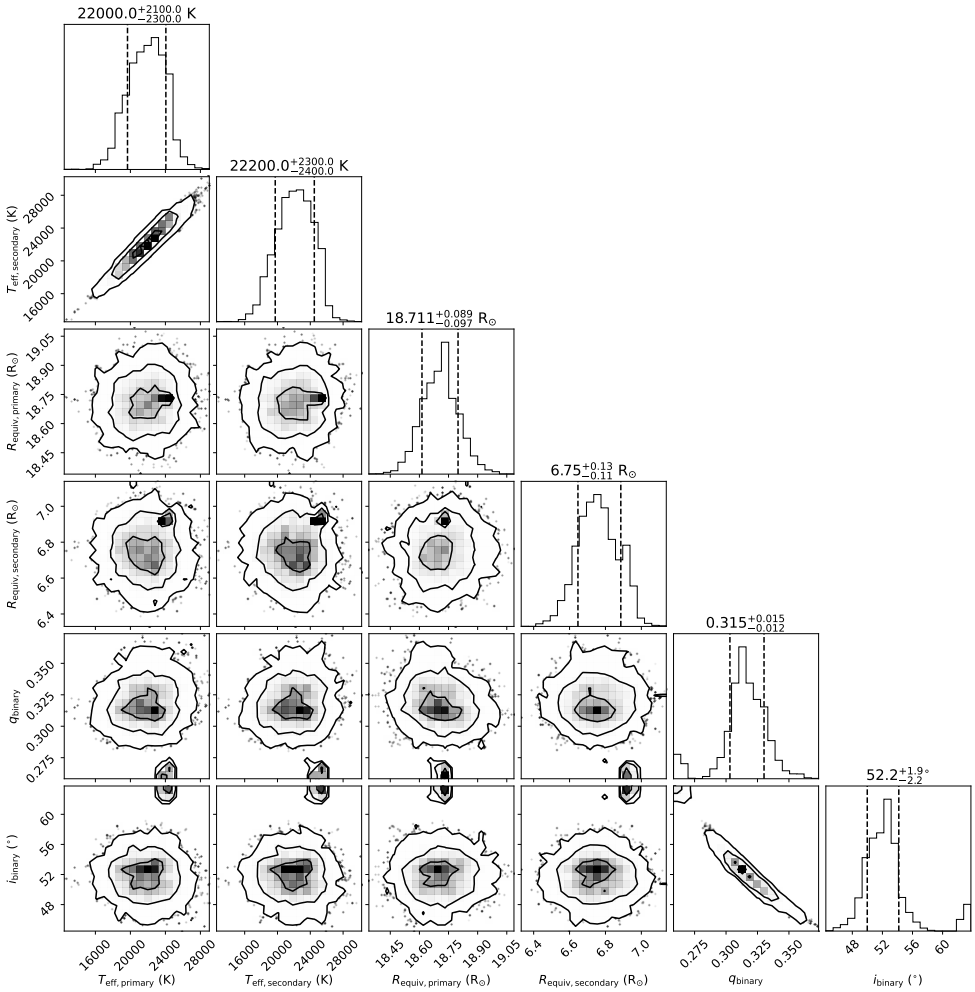

Figure 54: EMCEE corner plot for VFTS 687

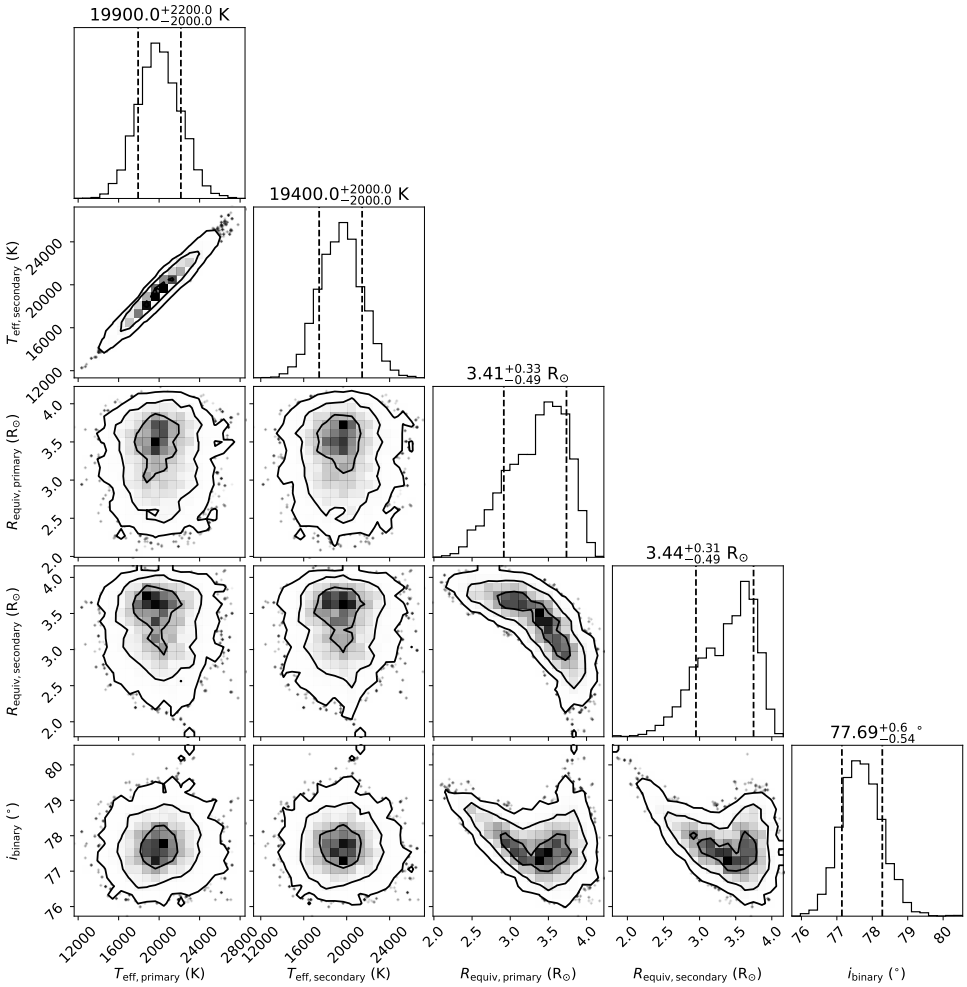

Figure 55: EMCEE corner plot for VFTS 883

Declaration of self-commitment

Hereby I declare that I wrote this work on my own and without using foreign support. Sources are indicated when I used information from others.
This work has neither been submitted to any examination authority nor has it been published yet.

Heidelberg, February 21, 2025 Henry Willems